CRANFIELD UNIVERSITY

KWASI FRIMPONG AYARKWA

PRODUCTION OF NOVEL ALUMINIUM BY ADDITIVE MANUFACTURING

SCHOOL OF AEROSPACE, TRANSPORT AND MANUFACTURING (SATM)

PhD Thesis
Academic Year: 2014 - 2018

Supervisors:
Prof. Stewart Williams
Dr. Jialuo Ding

April 2018

CRANFIELD UNIVERSITY

SCHOOL OF AEROSPACE, TRANSPORT AND MANUFACTURING

PhD Thesis

Academic Year: 2014 - 2018

KWASI FRIMPONG AYARKWA

PRODUCTION OF NOVEL ALUMINIUM BY ADDITIVE MANUFACTURING

Supervisor: Professor Stewart Williams
April 2018

This thesis is submitted in partial fulfilment of the requirements for the degree of Doctor of Philosophy

"I count not myself to have apprehended: but this one thing I do, forgetting those things which are behind, and reaching forth unto those things which are ahead, I press on towards the mark for the prize of the high calling of God in Christ Jesus"

Philippians 3:14

ABSTRACT

Aluminium matrix composites are required by manufacturers to produce light weight components or parts with improved mechanical properties over conventional aluminium alloys. These materials are useful for complex structures with locally strengthened properties which are difficult to produce by conventional techniques such as subtractive and formative processes. In this research wire and powder feed additive manufacture processes were investigated for their suitability for producing aluminium matrix particle reinforced composites as an alternative to conventional processes.

The research focusses on the use of wire + powder additive manufacture to produce aluminium silicon carbide composites. Different process variants were investigated including the use of either gas metal arc, gas tungsten arc or a laser as the heat source. In depth investigations of the main process parameters such as travel speed, arc or laser power were carried out. Of these both the gas tungsten arc and the laser proved to be viable options. It was found that a melt pool with as high a temperature as possible is required to successfully inject particles into the melt. Therefore it was found necessary to insulate the substrate in which the melt bead was being generated.

Detailed studies into the other controlling factors for embedding the SiC particles into aluminium melt pool were explored. It was found that the most important are the nozzle feeding direction, particle size, particle velocity and type of shielding gas. For example, it was necessary to use 150 µm SiC particles in order to successfully break the surface oxides and penetrate the melt pool correspondingly. For the arc based processes using helium as the shielding gas was highly beneficial as it resulted in a much larger melt pool size in comparison to using argon. It was found that particles were distributed at the top and bottom surface of helium produced melt beads. On the other hand, particles were mainly distributed at the top surface of argon and laser melt injected melt beads. For the laser process, the particles penetrated more than 1.5 mm into the melt bead. Finally the investigation showed that increasing the particle feed rate and heat input increases the % volume fraction of SiC reinforcement particles captured.

Keywords:

Wire + arc additive manufacture; Metal matrix composites; Silicon carbide; Tungsten inert gas; Cold metal transfer

ACKNOWLEDGEMENTS

I would like to thank the almighty God for good health and favour throughout the entire research. He always makes a way where there seem to be no way.

I want to thank the WAAMmat program members for funding the research. My sincere gratitude goes to my supervisors Prof. Stewart Williams, Dr. Jialuo Ding and Dr. Wojciech Suder for their entire support all through the PhD study and related research, for their immense knowledge, patience and motivation. Their guidance aided me throughout the research and writing of the thesis. I could not have imagined having better advisors and mentors for the research.

I want to also show my appreciation to the Welding Engineering and Laser Processing Centre (WELPC) team for all the stimulating discussions, the love from the different cultures and all the fun we have had throughout the years. I would like to say thank you to Zsolt, Uzoma, Eloise, Sonia, Goncalo, Pawel, Philip, Bridegeman, Sergio, Yash, Junny, Leo, Florent, Clement, Filo, Jan, Gu, Alex, Xiangfang, Yipeng, Chong, Armando, Julio, Kuladeep, Osas, Daniel and Usani. Not forgetting the lab technicians, Flemming and Nissar for their help and assistance in setting up of equipment for conducting experiements.

My deepest appreciation goes to my parents Prof. and Mrs Ayarkwa, my brother Junior Ayarkwa and my uncle Kwame Boakye for granting me all the support; financially, spiritually and my life in general. Without them I would not have made it this far. I also want to thank my church, Harvest Chapel International, Bedford, under the leadership of Rev. Benjamin Titi-Lartey for all the support and love they have shown me throughout my entire stay in England. I will never forget the great joy and love experienced from them.

Last but not least, I want to say a big thank you to my fiancée Barbara Asamoah for her patience, kindness and encouragement even through the difficult times of my studies. You are a star my dear.

TABLE OF CONTENTS

LIST OF FIGURES

LIST OF TABLES

LIST OF NOMENCLATURE

Al	aluminium
SiC	Silicon carbide
Al_2O_3	Aluminium oxide
Cu	Copper
WC	Tungsten carbide
B_4C	Boron carbide
V_{min}	Minimum particle velocity
η	Process efficiency
d	distance
A_{Al}	melt area
P_{SiC}	Particles captured per melt area
V_{SiC}	SiC particle velocity
ρ_{SiC}	Density of SiC
E_{kin}	Kinetic energy
M	Momentum

LIST OF ABBREVIATIONS

WAAM	Wire + arc additive manufacture
TOS	Topology optimised structures
MMC	Metal matrix composite
AM	Additive manufacturing
Al-WAAM	Aluminium wire + arc additive manufacture
PM	Powder metallurgy
SLM	Selective laser melting
AMC	Aluminium matrix composites
PRC	Particle reinforced composite
LSP	Liquid state processing
DLD	Direct laser deposition
EBFF	Electron beam freeform fabrication
WLAM	Wire and laser additive manufacture
EWW	Effective wall width
TWW	Total wall width
SW	Surface waviness
TIG	Tungsten inert gas
MIG	Metal inert gas
% EP	Direct current electrode positive
% EN	Direct current electrode negative
AC	Alternating current
ACTIG	Alternating current tungsten inert gas
CMT	Cold metal transfer
CMT-PA	Cold metal transfer pulse advance process
CMT-P	Cold metal transfer pulse process
LMI	Laser melt injection

WFS	Wire feed speed
TS	Travel speed
UTS	Ultimate tensile strength
YS	Yield strength
HI	Heat input
KE	Kinetic energy
CTWD	Contact tip to work distance
WFS/TS	Wire feed speed to travel speed ratio
LH	Layer height
SEM	Scanning electron microscope
PFR	Powder feed rate
GFR	Gas flow rate
% SiC	Percentage volume fraction of SiC

1 Introduction

1.1 Background

Metal matrix composites (MMCs) are useful as they have improved strength, stiffness and tribology in comparison to conventional metal alloys. An important class of MMC is aluminium particulate reinforced MMCs which are used especially in the automotive industry [1–3]. The global research market [4] has shown an increasing trend in the use of MMCs between the years 2007 and 2013 (Figure 1-1). The research showed that in the year 2007 about 4.1 million kilograms of MMC were used which further increased to about 4.4 million in the year 2008. A further projection of about 5.9 million kilograms of MMC was anticipated for the year 2013 with a significant application in ground transportation and electrical industries. Figure 1-2 also shows the latest global market needs and profit analysis projected from the year 2012 to 2019 with an estimated increase of about 38 % tonnes in volume of MMCs.

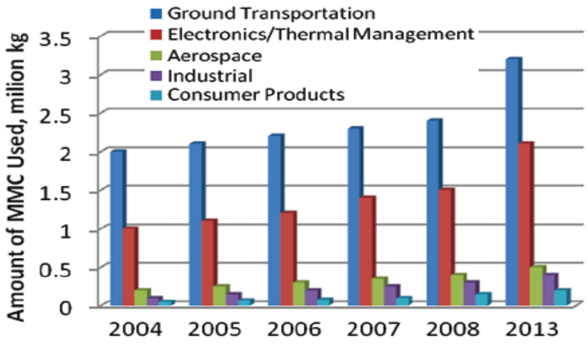

Figure 1-1: Typical application of MMCs showing increasing trend in its use [4]

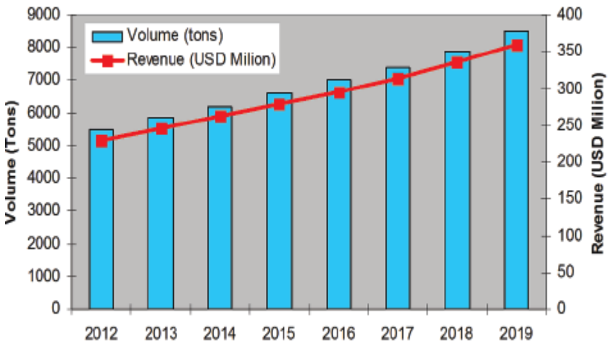

Figure 1-2: Projected market needs and associated revenues of MMCs [4]

The current manufacturing routes of MMCs are based around solid and liquid processing methods [5,6]. A number of commercial applications require liquid fabrication techniques because of their low cost of manufacturing and also their ability to employ already existing methods developed for conventional unreinforced metals such as casting [7]. However, inhomogeneous distribution of particles and structure reproducibility is the main limitation of liquid state processes (LSP). The limitations in LSPs result from the difficulty in controlling process parameters, wettability and/or adverse chemical reactions which could occur between the molten metal and the reinforcement due to the long solidification time [8,9]. These limitations tend to affect the physical, chemical and mechanical properties desired, hence, the difficulty of manufacturing large semi-finished products in MMCs.

Furthermore, solid and liquid fabrication processes also have limitations in general and they are particularly limited in making complex parts. An example of a complex part is a topology optimised structure (TOS). Topology optimisation is attractive to manufacturers due to its excellent weight and cost savings [10,11]. Topology optimised structures factors into account both the size and shape of the structure (Figure 1-3). Typical TOSs are made of trusses and if one member fails, structures such as this have no residual strength because there is no alternate load path. Therefore consideration is given to all the constraints of the component to be produced [10,12,13].

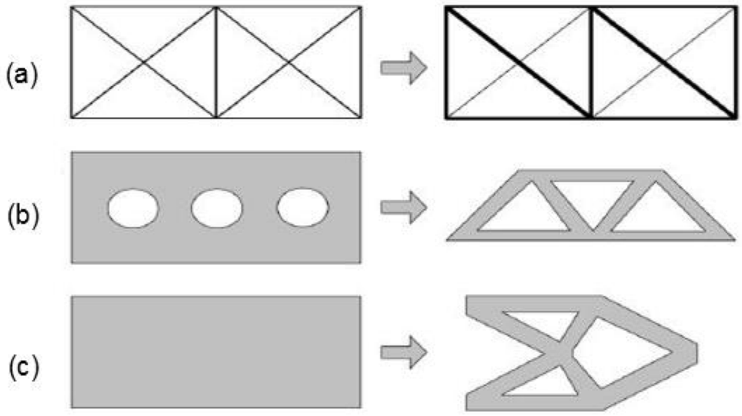

Figure 1-3: Structural optimisation, (a) sizing; (b) shape; (c) topology [10]

In production, it would be desirable in a TOS to be able to vary the properties of the materials from high performance relatively heavy to low performance relatively light. A common way of manufacturing TOSs is by additive manufacture (AM) [11]. The different types of AM processes can be seen in Figure 1-4. AM processes have been classified into powder bed fusion (PBF) and directed energy deposition (DED). PBF uses thermal energy to fuse regions of powder selectively whilst in DED a focussed thermal energy is used to melt powder or wire which is fed in the direction of the heat source [14].

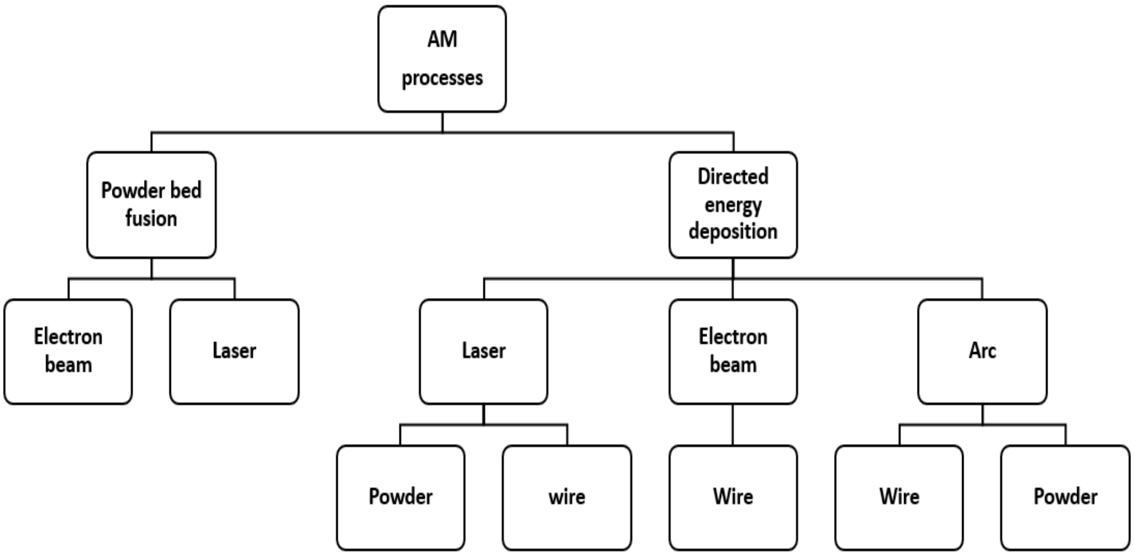

Figure 1-4: Classification of additive manufacture systems

Presently, all additively manufactured TOSs have been produced using powder bed systems. The limitations of powder bed systems are the cost and the size. For most powder bed systems the size is limited to a maximum of 500 mm. Larger systems up to 1000 mm have been developed but are extremely expensive to purchase and use. A way to overcome these manufacturing challenges have been the development of the wire + arc additive manufacture process (WAAM) which employs already developed arc welding techniques to produce parts in an additive fashion [15,16]. WAAM has been shown to be able to build large engineering parts at low cost in a range of different materials. However, WAAM has not been used for production of metal matrix composites. The flexibility of controlling WAAM process parameters to control melt pool behaviour could be an advantage during MMC manufacture in terms of producing complex shaped parts on a large scale and improving the properties compared to other LSPs.

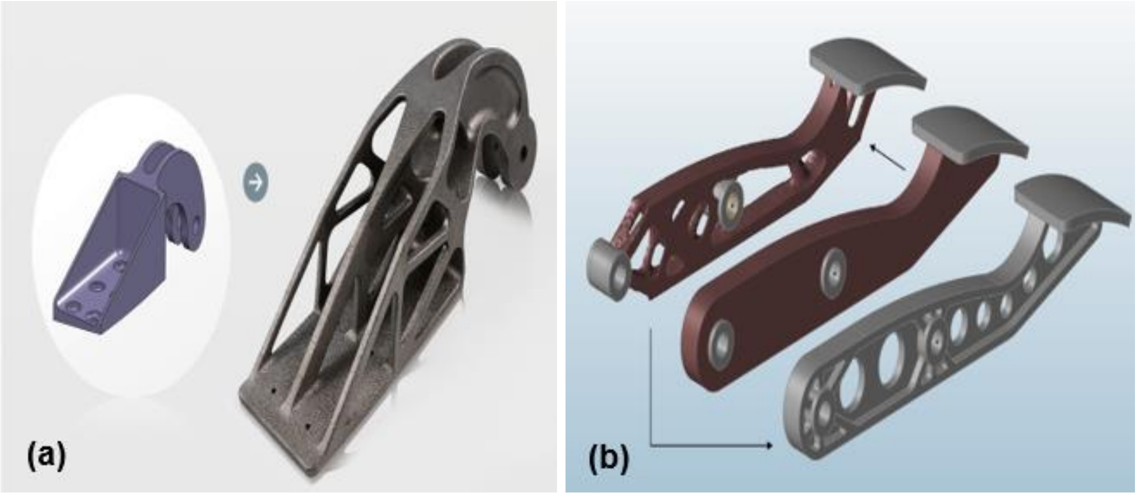

Figure 1-5: Topologically optimised parts: (a) Topology optimised bracket; (b) Topology optimised race car brake pedal [17,18]

1.2 Hypothesis

Aluminium matrix composites can be produced by injecting reinforcement particles into an aluminium melt pool during wire + arc additive manufacture.

1.3 Research Aim and Objectives

The aim of the research is to produce aluminium matrix composites (AMCs) by wire + arc additive manufacture (WAAM) and determine their physical and mechanical properties with the view to producing a topology optimised structure of different materials such that the process can be switched on and off at short processing lengths.

The following objectives are considered:

- To identify a suitable process for aluminium metal matrix components manufacture using wire + arc additive manufacture
- To develop the selected wire + arc additive manufacture process for aluminium matrix composites

- If high quality materials can be produced to determine their mechanical properties

The methodological approach to the research is shown in the schematic diagram in Figure 1-6. The research approach is a literature review and aluminium WAAM baseline studies to identify the suitability of cold metal transfer (CMT) and alternating current tungsten inert gas (ACTIG) processes in the manufacture of MMCs as can be seen in stage 1. Stage 2 is the production of MMCs by WAAM. If successful (Y), it can be followed by material property studies in stage 3. If unsuccessful (N), then a more sophisticated technique such as the laser melt injection process can be used. Furthermore, if unsuccessful (N), a hybrid laser + WAAM technique would be used and then followed by material property studies (stage 3).

The study identified both the ACTIG and laser melt injection processes as viable options for producing AMCs.

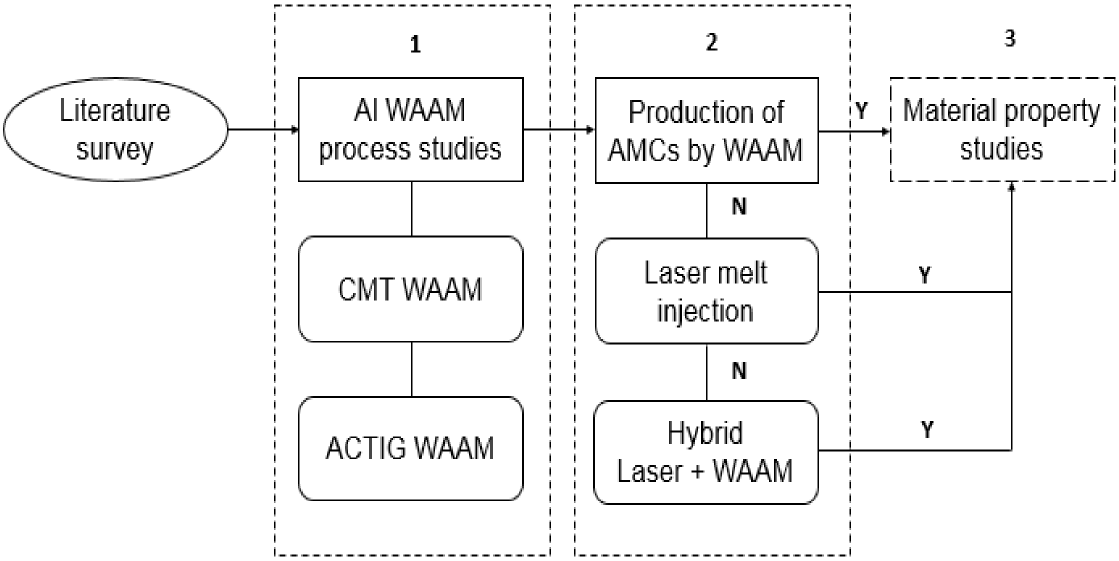

Figure 1-6: Outline of research methodology

1.4 Thesis Structure

The Thesis comprises 7 chapters.

Chapter 1 presents a general overview of metal matrix composites and topology optimisation as well as the research aim, objectives and Thesis structure.

Chapter 2 presents literature review on related research work. This includes: current production techniques of aluminium matrix composites, physical and mechanical properties, current aluminium wire + arc additive manufacture techniques and weldability of aluminium and its alloys.

Chapter 3 presents and describes all the materials and equipment used in the study. Chapters 4, 5, 6 and 7 present all the methods used, results, discussion and conclusions for the different investigations from each research.

Chapter 4 details process studies of the cold metal transfer process on aluminium WAAM. The effects of the process parameters on WAAM wall dimension, microstructure and porosity are presented.

Chapter 5 presents process studies conducted on aluminium using the alternating current TIG process. The effect of alternating current time cycle on single bead and linear WAAM walls have been presented. In addition, a working environment is also presented.

Chapter 6 presents the production of aluminium silicon carbide composite using ACTIG WAAM process. The effect of particle velocity, particle size and particle feed rate on the reinforcement particle capture efficiency is presented. In addition, the effect of the WAAM process parameters such as shielding gas type, heat input and WFS is also presented. Furthermore, the chapter also presents studies conducted using the laser melt injection process.

Chapter 7 summarises the conclusions of the research and suggests areas for further studies.

2 Literature Review

Context

This section presents a review of existing body of knowledge on the topic under investigation and presents "the state of the art" of the findings. The literature review includes an overview of existing research on aluminium matrix composites (AMCs), taking into consideration the present manufacturing techniques of these materials and the physical and mechanical properties associated with such manufacturing routes. In addition, current studies on aluminium wire + arc additive manufacture (Al-WAAM) have also been reviewed as a novel manufacturing technique for the production of AMCs. Prior to the above, a brief discussion on aluminium and its alloys was also conducted.

2.1 Aluminium and its alloys

Aluminium is the third most common chemical element found in the crust of the earth and comprises about 8 % its weight [19,20]. The existence of aluminium was established by the British electrochemist, Sir Humphrey Davy in 1808, and seventeen years later the first pellet of the metal was produced by Oersted, a Danish scientist [20,21]. The metals outstanding light weight characteristics and ease of shaping was also discovered by Wöhler, a German scientist. However, the metal was limited by its high cost of production which led to further research work to reduce the cost of production and processing of the metal. In 1886, this was made possible through the work of a French scientist Paul Louis Toussaint Héroult and a United States scientist Charles Martin Hall [22]. Through their independent work, molten cryolite (Na_3AlF_6) used for dissolving the aluminium oxide (Al_2O_3) was discovered. This was achieved by passing an electric current through the solution to dissolve the aluminium oxide into aluminium and oxygen.

2.1.1 Classification

Aluminium alloys can be classed into either cast or wrought [23]. Moreover, the main alloying elements have been categorised into different series: pure aluminium (1xxx); copper (2xxx); manganese (3xxx); silicon (4xxx); magnesium (5xxx); magnesium and silicon (6xxx) and zinc (7xxx) [23–26]. Figure 2-1 depicts some of the commonly used alloying elements. These have also been grouped into two, as heat-treatable and non-heat-treatable alloys. These alloys obtain their strength as-casted or by work hardening, solid solution and age (precipitation) hardening.

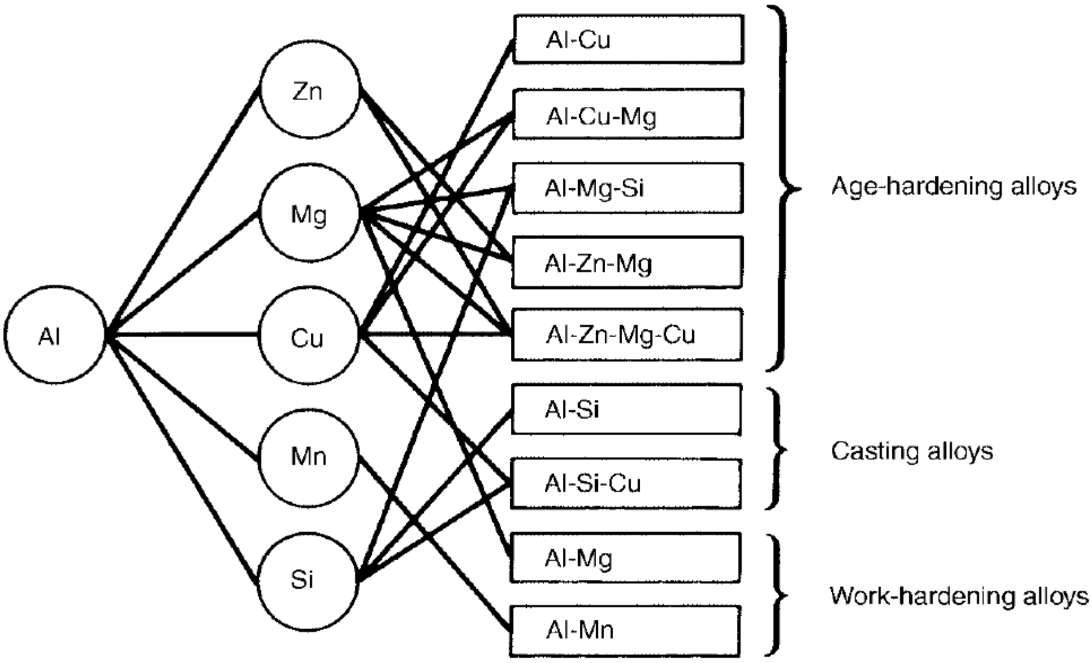

Figure 2-1: Commonly used alloys of aluminium [25]

2.1.2 Strengthening Mechanisms for Aluminium alloys

2.1.2.1 Work hardening

Work hardening is used mainly to increase the strength of non-heat-treatable aluminium alloys (1xxx, 3xxx and 5xxx). The process deforms the metal by the input of mechanical energy during cold rolling [23,27]. The deformation process results in increasing the hardness with a reduction in ductility. This proceeds until a stage is reached where the material becomes brittle such that any further deformation results in fracture. Figure 2-2 depicts the effect of work hardening on strength, hardness and ductility. During cold working, grains are elongated in the working direction leading to a high level of internal stress and an ideal grain orientation. Work hardened materials can be restored back to their original state by annealing to eliminate strain hardening and restore the grain orientation.

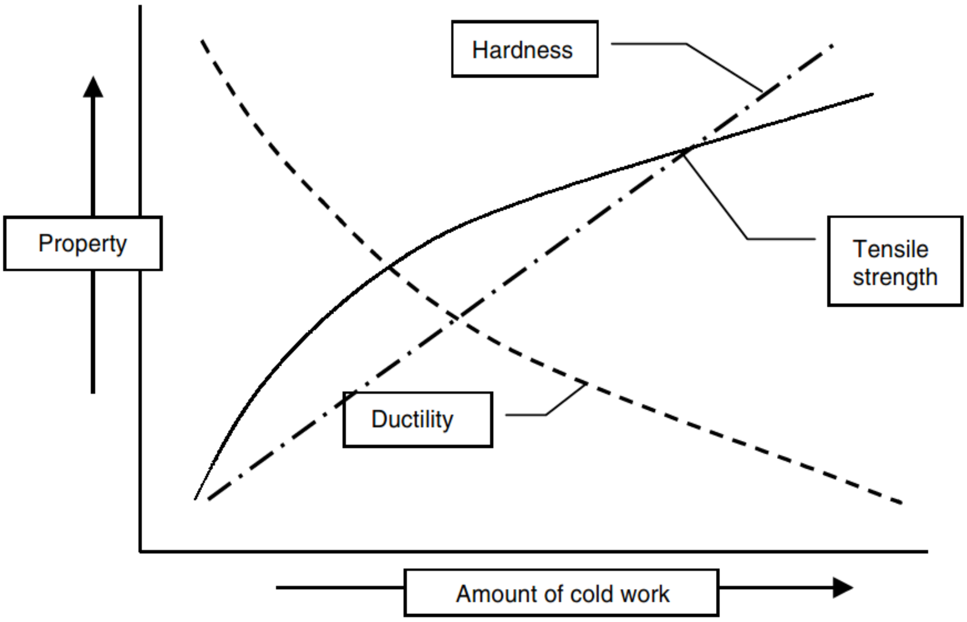

Figure 2-2: Cold work effect on strength, hardness and ductility [23]

2.1.2.2 Solid solution strengthening

Generally, pure aluminium is soft, ductile and does not have the required strength for engineering purposes. Therefore, it is alloyed with specific elements (solutes) which dissolve in aluminium (solvent) to increase the strength [23,27]. These solute atoms differ in stiffness, size and charge which makes their distribution random. The random distribution increases the hardness by serving as an obstruction to dislocation movement [23,27,28]. However, there is a limit to the amount of solute being dissolved in the solvent [28]. According to Mathers [23], microscopically, the limit of solubility results in the formation of second phases (inter-metallic compound; secondary solid solution) [23]. Second phases such as copper aluminide ($CuAl_2$) and aluminium silicide results in increasing the strength and hardness in aluminium alloys and are formed by alloying with copper and silicon respectively. Other alloy elements such as magnesium and manganese also result in increasing the strength and weldability of aluminium [29]. Solid solution alloys have been grouped into two as interstitial and substitutional as depicted by Figure 2-3 [23,28]. According to the authors, in interstitial solid solution, alloying elements fit into the interstices or spaces of solvent atoms while substitutional solid solution replaces solvent atoms. These alloying elements distort the lattice thereby introducing a strain in the lattice preventing dislocation movement. The strain introduced increases the tensile strength with corresponding decrease in ductility by impeding the slips between adjacent atomic planes.

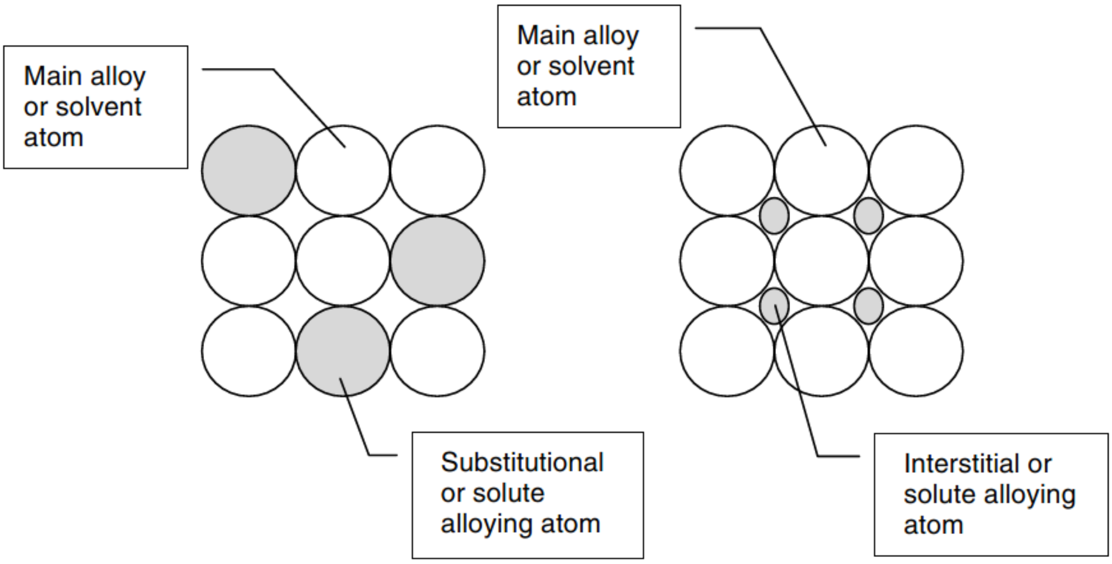

Figure 2-3: Forms of solid solution strengthening [23]

2.1.2.3 Precipitation hardening

Precipitation hardening is time and temperature dependent and generally affects metallic microstructures with two or more phases. The final geometry of the material is affected by the dispersion of the minor phase either within the grains or on the grain boundaries [23]. This is commonly found in the 2000 series (Al-Cu) grade aluminium as depicted by the phase diagram in Figure 2-4. During precipitation hardening, the alloy is heated to a point (between 500 ^oC and 580 ^oC) where the second phase (Cu) dissolves in Al solution [27]. This is followed by rapid cooling in water or in still air. The reason for the rapid cooling is to prevent the second phase from precipitating but retained at room temperature as a metastable supersaturated solid solution [23]. Below 500 ^oC, a two phase alloy is derived comprising of α and $CuAl_2$. When the alloy is slowly cooled, a low driving force becomes apparent for precipitation of $CuAl_2$; thus, reducing the nucleation rate. The few nuclei form and grow to become large precipitates which are spaced out and therefore moving dislocations find it easy to avoid the precipitates thus making the material soft [27]. Conversely, by cooling the alloy faster results in a finer structure owing to the high driving force which increases the nucleation rate as compared to the slowly cooled. The fine structured precipitates, which are closely spaced, act as an obstruction to dislocation movement and hence make the alloy harder.

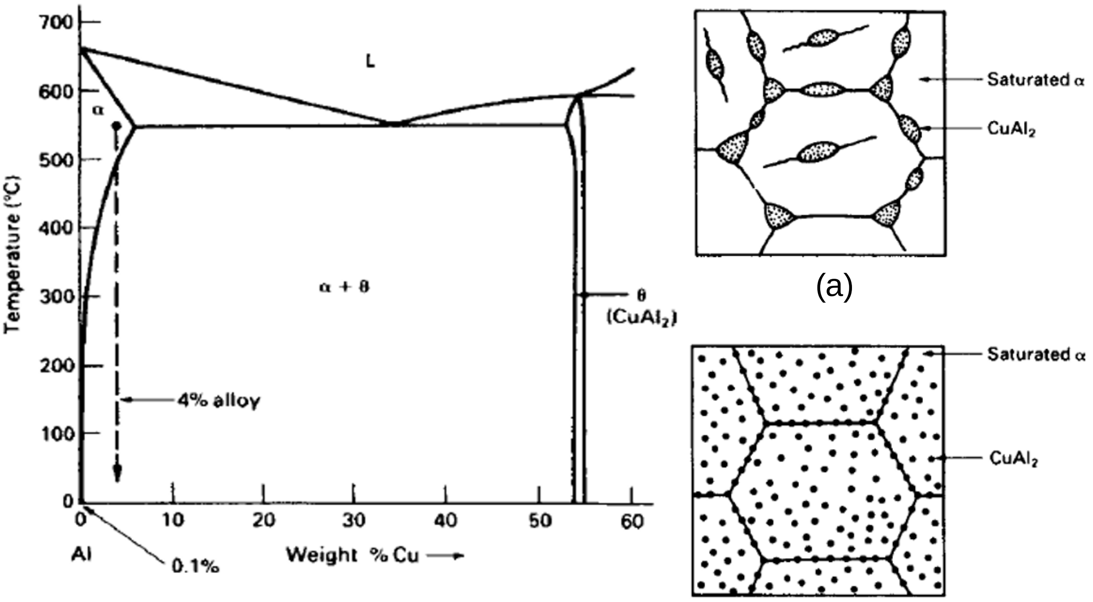

(a)

(b)

Figure 2-4: Al-Cu phase diagram and microstructure of (a) slowly cooled and (b) moderately cooled from 500 ^{o}C [27]

Aluminium alloys have been used in lightly loaded structures because of their limited hardness and strength, in addition to their low melting point [30]. Furthermore, the materials low stiffness and poor tribology properties have also been identified by MahendraBoopathi et al. [31]. Presently, a number of research works have also been geared towards production of aluminium metal matrix composites because of their great improvement in the material properties in terms of stiffness and tribology.

2.2 Aluminium matrix composites (AMCs)

2.2.1 Fibre reinforced composites (FRC)

Composite materials have been classified based on the chemical and physical nature of the matrix as metal matrix, polymer matrix and ceramic matrix [32]. The reinforcement type can also be used to classify them into particle, whisker/short fibre, continuous fibre and monofilament reinforcements [33]. FRCs are generally multiphase structures comprising of a distinct fibre constituent (reinforcement) integrated in a continuous phase (matrix) [32,33]. Properties of FRCs are derived from the respective constituent phases; thus, the major part of the load is carried by the fibre while the matrix holds them together during load transfer as shown in Figure 2-5.

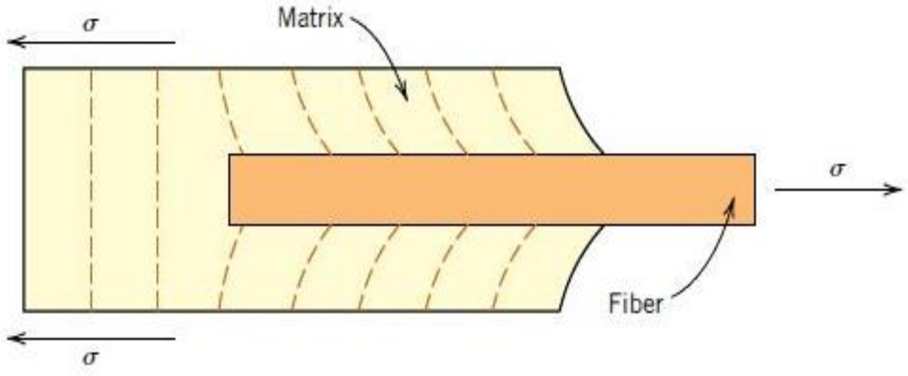

Figure 2-5: Load transfer in a fibre reinforced composites [32]

2.2.2 Particle reinforced composites

Particle reinforced composites (PRCs) compared to whisker and fibre reinforced composites have been of considerable interest to researchers because of their cost advantage and their excellent plastic forming capability, heat and wear resistance [19,34]. Aluminium PRCs have the ability to serve a variety of applications which may require light weight in combination with good mechanical properties such as improved fatigue damage tolerance and improved stiffness [9,35,36]. Ceramic particles such as aluminium oxide (Al_2O_3), silicon carbide (SiC), tungsten carbide (WC) and boron carbide (B_4C) have been used as reinforcements in molten aluminium matrix [37–39].

Table 2-1 outlines some physical properties of these ceramic reinforcements. The choice of reinforcement is dependent on several factors which include the application, production technique and cost.

Table 2-1: Physical properties of Al (6xxx) and ceramic particle reinforcements [40,41]

Properties	**Al**	**WC**	**SiC**	**Al_2O_3**	**B4C**
Density (g/cm3)	2.7	13 – 15.3	3.21	3.7 – 3.97	2.51
Compressive strength (MPa)	280	3100 - 5860	1725 - 2500	2070 - 2620	2900
Modulus of Rigidity (GPa)	34	483 - 641	476	393	445

2.2.3 Application of aluminium matrix composites

Aluminium matrix composites (AMCs) have been applied in components and parts of modern manufactured automobiles [1,2]. The properties exploited mostly are the increased thermal expansion coefficient, wear resistance, improved fracture properties and fatigue damage tolerance. One area of usage is in the manufacture of pistons (see Figure 2-6a) due to their operation in very harsh thermal, dynamical and mechanical environments [4,42]. Pistons are subject to high fatigue cycles (100 Hz) under mechanical load which makes the component prone to fatigue damages [4]. Also, during expansion, pistons have an intimate interaction with cylinders at extreme pressures [42]. Therefore, material properties such as high thermal expansion coefficient, wear resistance and dynamic endurance becomes vital during manufacture [4,43].

Another area of AMC usage is in the production of cylinders for engine blocks. Currently, hybrid aluminium matrix composites reinforced with Al_2O_3 and carbon have been used in this application [43,44]. These engine blocks have been produced by squeeze casting as depicted by Figure 2-6b.

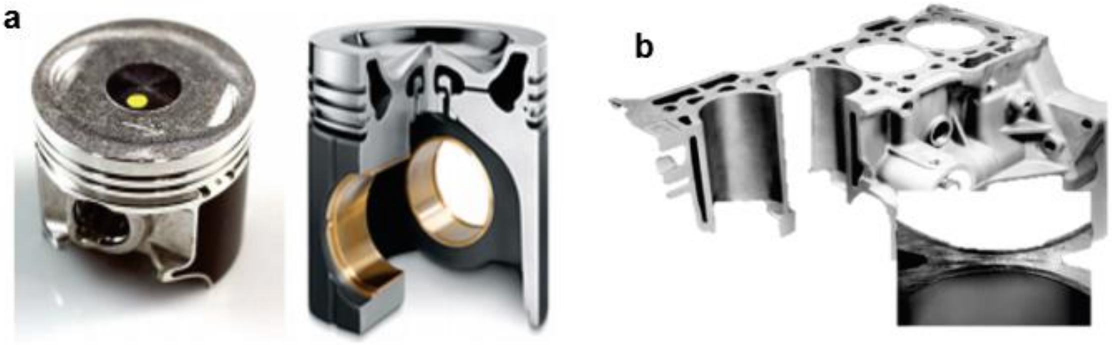

Figure 2-6: Applications of AMCs: (a) Pistons; (b) Engine cylinder block [4]

2.3 Production of aluminium matrix composites

The production technique selected for aluminium matrix composites (AMCs) is dependent on factors such as the integrity of the microstructure desired and the level and type of reinforcement loading [33,36,45–47]. Processing routes for AMCs are classified into two main groups i.e., solid state and liquid state processes [6,33,35]. Figure 2-7 illustrates commonly used processes for aluminium matrix composite manufacturing.

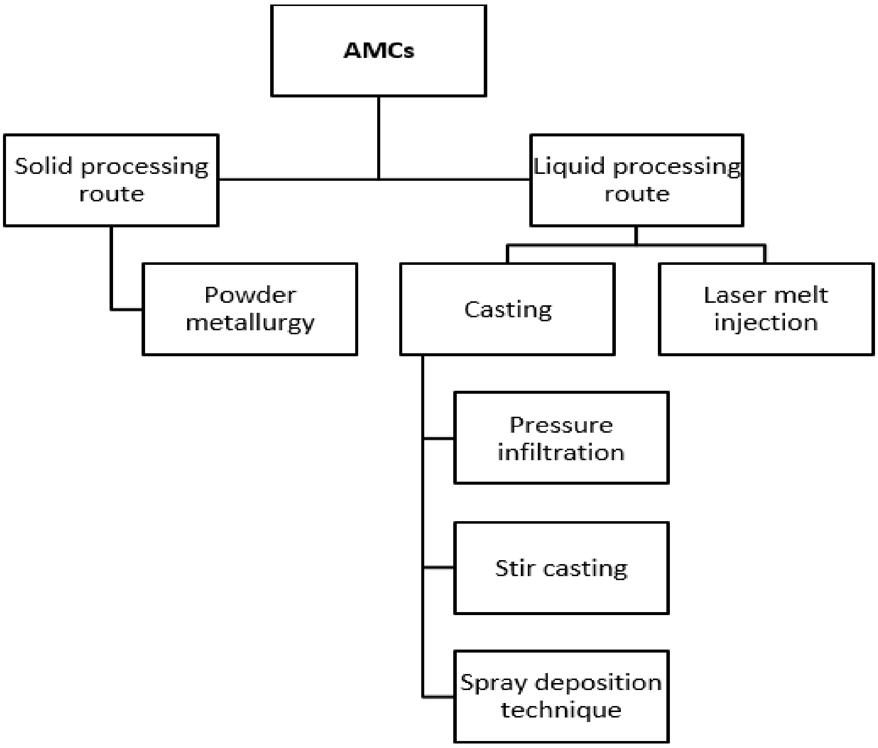

Figure 2-7: Common manufacturing routes for AMCs

The main differences in the processes for aluminium matrix composite manufacture lie in the matrix alloy. For solid processing routes, the matrix is in powder form whilst in liquid processing routes a molten state matrix is utilised [33–35,48,49]. For solid processing route, both the matrix and reinforcement are blended in powder form to obtain a homogeneous mixture. In view of this, careful selection of the matrix and reinforcement particle sizes is required to prevent agglomerates from forming after blending prior to usage in the final product [34]. In some liquid processing routes such as casting, reinforcement particles tend to spend a considerable amount of time with the molten matrix and result in formation of reactive phases which could damage the material properties [50]. Therefore, the reinforcement particle needs to be selected after considering the matrix alloy processing time and temperature. A number of research works have used SiC reinforcement and found it to yield good results [8,50–52]. Li et al. [51] conducted studies on fatigue crack growth behaviour of SiC reinforced Al matrix. The authors found increased fatigue resistance of the 4.5 µm Al-SiC composite alloy over the unreinforced alloy (see Figure 2-8).

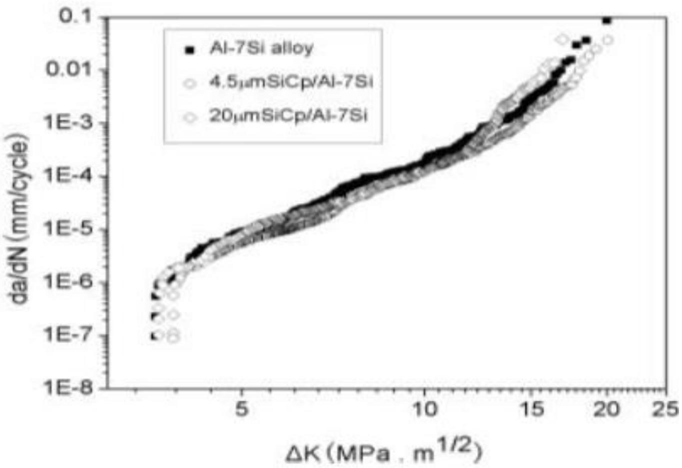

Figure 2-8: Fatigue crack growth rate (da/dN) as a function of stress intensity factor (ΔK)

Meena et al. [8] also conducted studies on the mechanical properties of Al-SiC produced by stir casting technique and identified superior strength and hardness over the conventional alloy. Occhionero et al. [52] identified Al-SiC as an ideal material for packaging components for thermal and light weight applications. It is for the good fatigue properties that this study focuses more on SiC reinforcement.

2.3.1 Solid processing route

Powder Metallurgy (PM) is a common and versatile solid fabrication technique used in mixing powdered aluminium alloy with particulate or short fibre or whisker ceramic particles [33,35]. This method was earlier developed due to the wetting difficulties encountered between ceramic particles and the molten metal. Figure 2-9 illustrates the process flow chart involved in powder metallurgy. In PM process, particles are fed into a mould of preferred shape and mixed. Pressure is then applied to enable further compaction of powder by cold pressing. Subsequent heating at a low temperature below the melting point of the powder can also be applied to facilitate the bond between the particles [35]. After mixing, direct pressing can also be achieved by hot pressing and the consolidated material produced can be used as an MMC [33]. Nevertheless, this method may be detrimental in terms of handling of highly reactive/explosive powders and the production route is rather complex and challenging to achieve even distribution of particles in the matrix [34,35]. Furthermore, it is difficult to produce intricate shapes by solid processing routes because of the low flowability of metal powder.

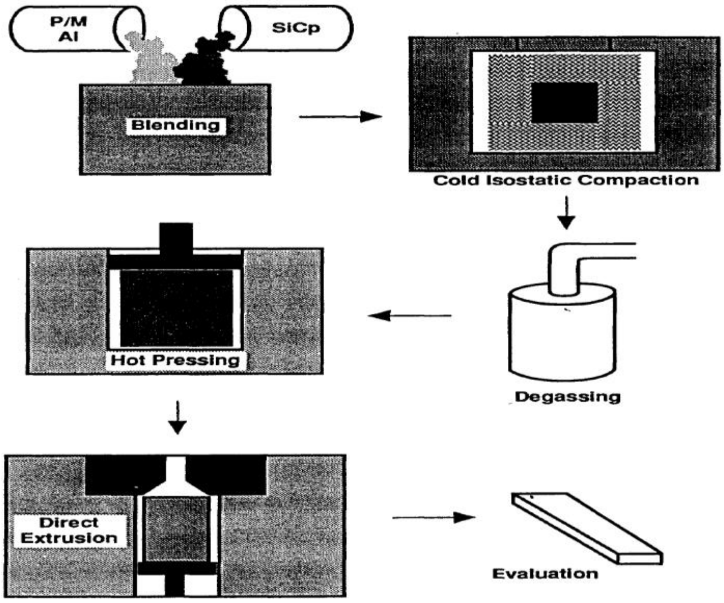

Figure 2-9: Powder metallurgy process [34]

2.3.2 Liquid State Process (LSP)

LSPs are commercially used by many industries due to their inherent benefits over solid-state processes. According to Michaud [7] and Huda [35], this can be attributed to the ease of handling liquid metal and the overall efficiency of the process as compared to the long processing times of solid state processes. Furthermore, composites can be produced using casting methods already developed for unreinforced aluminium metals. Nevertheless, LSPs have also been identified to be difficult in terms of part reproducibility due to the limited control of process parameters (such as melt temperature and viscosity of the liquid metal), wetting of ceramic reinforcement by molten metal and the detrimental chemical reaction which could occur at the interface between the reinforcement and the aluminium matrix [6,35,48,53]. The mentioned limitations would make it difficult to produce topology optimised structures by LSPs and may require complex designs patterns. However, complex LSP design strategies will result in increasing the manufacturing cost.

2.3.2.1 Casting or liquid Infiltration Processes

Casting or liquid infiltration processes have been identified as economical in fabrication of metal matrix composites [44,54]. In these processes reinforcing material is placed in a mould and infiltrated by molten metal (matrix) which flows through the interstices to fill pores thereby producing the composite [7]. However, microstructural inhomogeneity could result in particle agglomeration as well as sedimentation in the melt during solidification [49]. In view of this, a pressure infiltration technique has been developed which forces liquid metal into a preform (fibrous or particulate) and this helps to avoid problems with wettability and interfacial reaction. On the other hand, vortex or stir casting, a process development employing a mechanical stirrer has also been developed as depicted in Figure 2-10 [54,55]. In this process, pre-treated ceramic particles are introduced into the molten alloy prepared by a rotating impeller and then subsequently stirred [33]. Pradeep et al. [56] stated that particle distribution in the final product is dependent on the property of the material and the process parameters incorporated which includes wetting of particles and melt, relative densities, mixing and solidification. Likewise, particle distribution in the molten matrix is dependent on the mechanical stirrer geometry, stirring parameters, melting temperature and particle characteristics [54]. According to Bhandare & Sonawane [54], stir casting can be used to manufacture composites of up to 30% volume fraction of reinforcement with size range between 5 µm to 100 µm. Furthermore, extrusion of cast components is sometimes implemented to reduce porosity, homogenise reinforcement distribution and refine the microstructure [24,57].

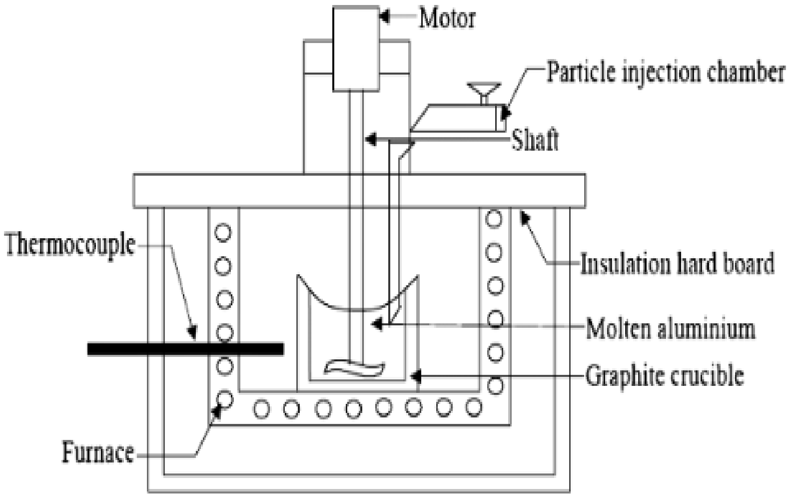

Figure 2-10: Stir casting process [58]

2.3.2.2 Spray deposition

Spray deposition technique is efficient in the production of particulate composites to form near-net shaped components with less processing steps [51]. Spray deposition technique minimises the tendency for chemical reaction to occur due to the short contact time between the matrix and reinforcement. Figure 2-11 shows the Alcan spray deposition process [14]. In this process, prior to spraying, the alloy is first melted by induction heating in a crucible. This is followed by applying pressure to eject the metal into an atomiser via a nozzle. Injection of particles into the atomised metal may also be done alongside and then deposited on a substrate preheated and positioned in the line of flight. The process builds the solid on a collector which is later moved from the substrate after cooling and then followed by rolling. This technique often displays inhomogeneous distribution of particles (ceramics) with about 5 - 10% porosity [33].

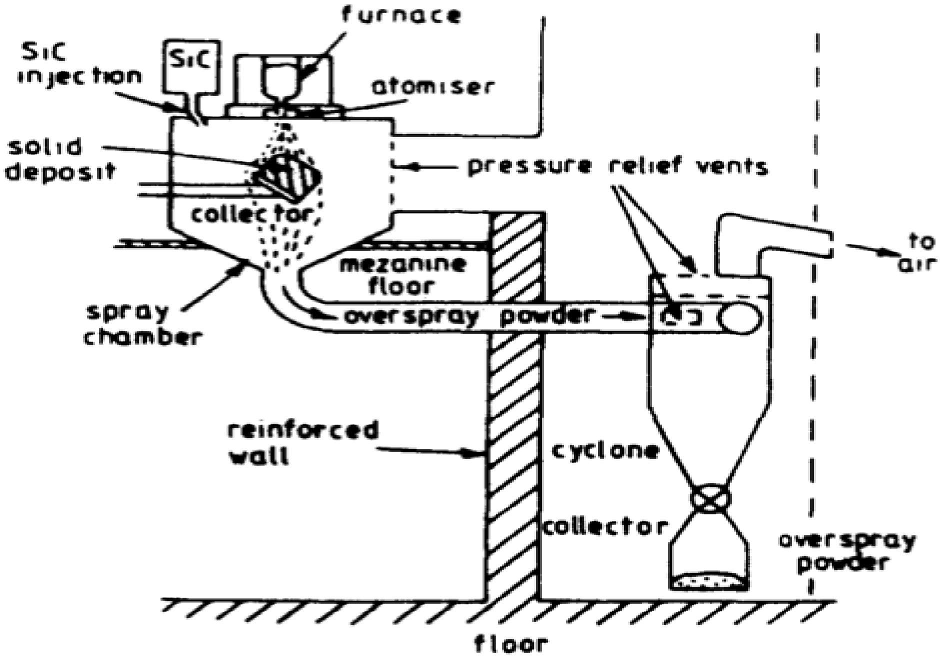

Figure 2-11: Alcan spray deposition process [35]

2.3.2.3 Laser melt injection (LMI)

In this process, a laser beam is used to melt the surface of the substrate (matrix) with simultaneous injection of particles as shown in Figure 2-12. These particles are trapped after rapid solidification of the melt pool, producing metal matrix composites. Studies have been conducted on laser melt injection of particles into aluminium matrix [59–61]. Vreeling et al. [59] conducted studies on the role of oxide layer during injection of SiC particles into an aluminium substrate. The authors identified a narrow operating envelope for successful injection of SiC into aluminium melt. The key factor for producing AlSiC composite was the temperature. For most studies, particle injection was only possible after the substrate was preheated above a temperature of 300 °C [59–61]. Jendrzejewshi et al. [60] also conducted similar studies by injecting WC and SiC into aluminium melt to produce Al-WC and AlSiC composites. The authors found that WC localised at the bottom of Al melt whiles SiC particles penetrated to a depth of 1 mm. The increased depth of penetration of WC resulted from its high density in comparison to SiC as shown previously in table 2-1.

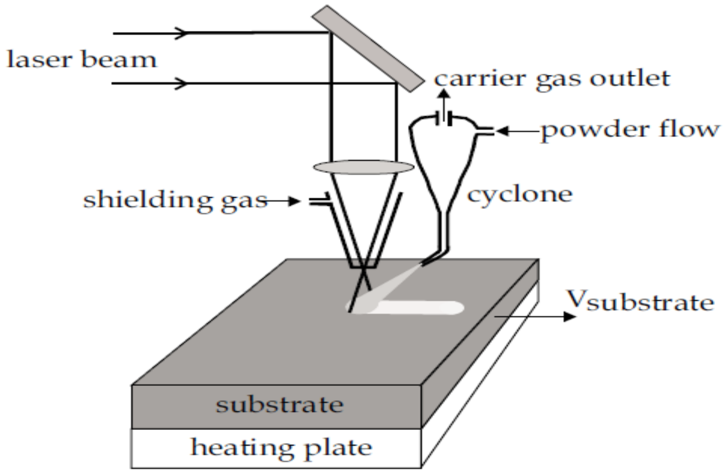

Figure 2-12: Schematic of a laser melt injection process [59]

The main challenge of the LMI process is the high reflectivity of aluminium [61]. As a result, a high energy density was required to produce a melt pool feasible for particle injection. A way to overcome the manufacturing limitations of laser is by using wire + arc additive manufacture (WAAM). WAAM has been successfully used in depositing aluminium melt tracks. The low reflectivity and cost of WAAM for aluminium deposition is an advantage.

2.3.3 Powder feed systems

Powder feeders are very essential in industrial applications which involve powder transport such as laser cladding, thermal spraying and other advanced material processing [62]. Due to the differences in the size, shape, physical and mechanical properties, the steady-state flow used in conveying a particular powder may not work for another powder [63]. For example, decreasing the grain size of powder below 15 µm decreases the flowability which results in problems with powder conveyance. Again, powder flow can also decrease drastically for cohesive and sticky powders [64]. In view of this, different feeding systems may be employed for different types of powders. It is therefore important to understand the 'flowability' of powder since it is the main limiting factor during powder deposition. Powders are able to flow because it consists of a group of small particles with each individual particle having the ability to flow relative to each other [62,65]. According to Koebler et al. [62] the angle of repose (α) that is the angle at which inter-particle friction forces are influenced by gravitational force is unique in each powder and is a function of the particular powder's flowability Figure 2-13.

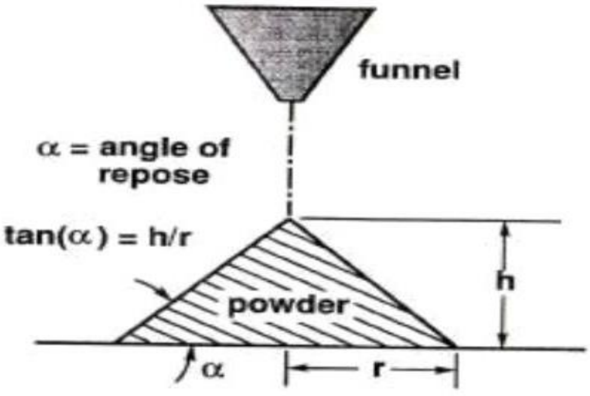

Figure 2-13: Angle of repose for a mass of powder leaving a funnel [62]

Generally, powder feeders have been grouped into different classes based on the operating principles. These include gravity – based, mechanised wheel, fluidised – bed and vibrating. For some powder feeders, in order to achieve steady powder stability, a combination of the above methods may be used [62,65].

2.3.3.1 Gravity – based powder feeder

The gravity – based powder feeder (Figure 2-14a) mainly depends on the weight of the powder to flow from the hopper to the orifice which is influenced by the flowability of the powder [62,66]. A number of feed systems incorporate a metering wheel below the hopper to enhance regulation of powder deposition.

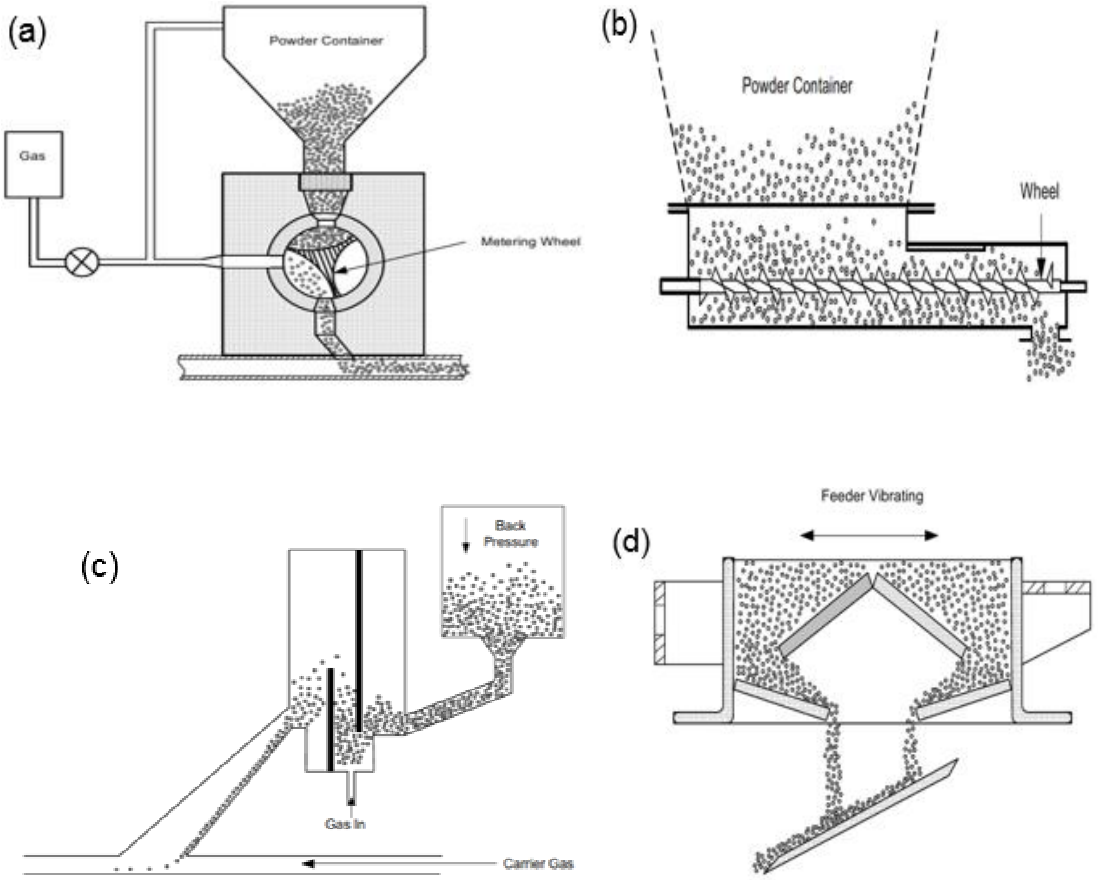

Figure 2-14: Groups of powder feeders: (a) gravity – based; (b) mechanised wheel; (c) fluidised – bed; (d) vibrating [62]

Mechanical wheel powder feeders can handle numerous powders of different grain sizes. This system can operate with zero or low pressure differential between the outlet and inlet [62]. Figure 2-14b depicts a typical mechanical wheel powder feeder and consists of a pitch with diverse diameter ratio or a propeller which can pull powder from the hopper to feed into the outlet. To promote the uniform flow of powder, different configurations can be used at different flow rate. However, one noticeable disadvantage has been the wear of the wheel disc which greatly affects interaction between the abrasive powder and the moving part [62,65].

Fluidised – bed powder works based on fluid mechanics principles to avoid the need for a mechanical part to deliver powder [65]. The principle works by delivering a non – pulsating but continuous powder feed, thereby giving the user optimum control over the process. The system is also beneficial in terms of the reduction in cost of maintenance and replacement of parts [65]. The system has been designed such that a pre-set quantity of gas is transported to a closed hopper with powder [62,66] (Figure 2-14c). Beneath the angled hopper, the powder is lifted by a high pressure stream of gas into the air which separates and fluidises the particles to be transported. This is picked up by a tube which is positioned above the fluidising gas inlet to propel to the feed hose. According to Liberto [66], issues that can arise with this feed system is with irregular fluidization and uneven powder containment in hopper.

The vibratory based feeder also known as the oscillating feeder (Figure 2-14d) is made up of a flat - bottomed tray conveying powder from a hopper to an angled tray using an external force to vibrate the tray. This transports the powder down to control the powder feed to the outlet. The system is within 1 % precision of the preferred flow rate [62].

2.4 Metallurgy of aluminium matrix composites (AMCs)

The physical and mechanical properties of AMCs are affected by several factors which include: wettability of the matrix and reinforcement [9,48,67]; reaction between the matrix and reinforcement [39,50,53]; type and size of reinforcement [6,31]; reinforcement volume fraction and distribution of the reinforcement in the matrix [8,31,68]. Figure 2-15 depicts the microstructure of a typical AMC; where the dark and light portions are SiC reinforcement and aluminium (Al) matrix respectively.

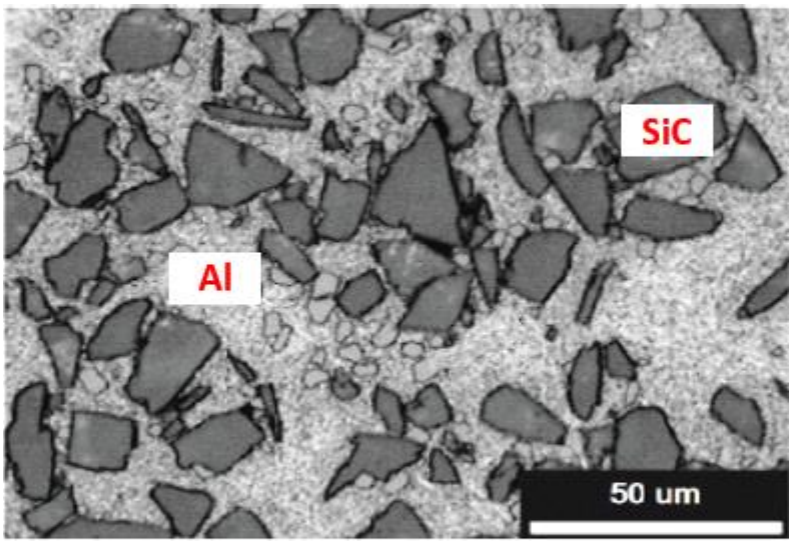

Figure 2-15: Microstructure of Al-SiC [69]

2.4.1 Wettability between the matrix and reinforcement material

In the production of MMCs, satisfactory bonds can be obtained when there is good wetting between the matrix and the reinforcement [6]. Wettability can be explained as the ability of a liquid to spread on the surface of a solid [9]. This becomes complicated when dealing with MMCs (particularly liquid state processes) therefore a number of procedures have been suggested to overcome the issues with wettability e.g. addition of surface reactive/active elements (Mg, Ca, Li, Ti or Zr) into the aluminium matrix, increasing the temperature of the metal matrix, coating the ceramic particles and pre-heat treatment of particles [47,48,59]. These result in increasing the solid surface energies, decreasing the interfacial solid – liquid energy and decreasing the surface tension of the liquid matrix alloy. The force binding the liquid and solid phases can be defined by the Young – Dupre equation which can be expressed in terms of the contact angle (see Figure 2-16) [48,70]. This defines the extent of wetting as perfect wetting ($\theta = 0^o$), no wetting ($\theta = 180^o$) and partial wetting ($0^o<\theta<180^o$).

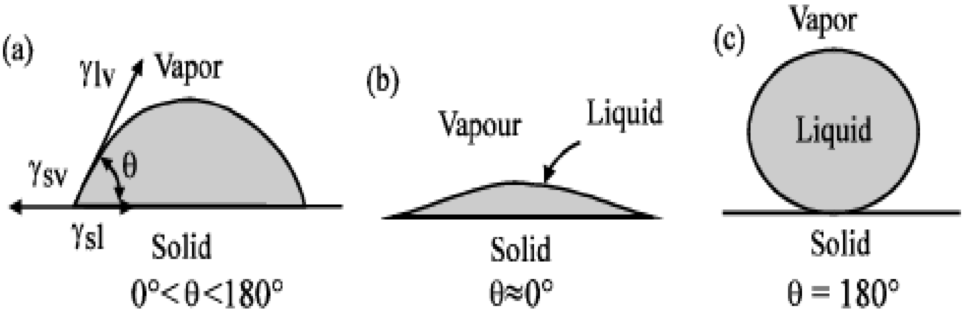

Figure 2-16: Schematic diagram depicting the relation between the contact angle and wettability: (a) Partial wetting (b) Perfect wetting and (c) No wetting [70]

Vreeling et al. [59] developed a model to provide an understanding of the mechanism of particle penetration in aluminium melt by laser melt injection. This considered particle penetration through the surface of the melt as well as particle movement in the melt. The study assumed the particles to be in the form of a sphere with radius R and a vertical velocity component v_0. The kinetic energy (E_{kin}) required to penetrate the surface barrier of the melt was calculated using Equation 2-1.

$$E_{kin} = \frac{2}{3}\pi R^3 \rho_{SiC} v_0^2; \quad \textbf{(Equation 2-1)}$$

$(\rho_{SiC}, density\ of\ SiC = 3217\ kg/m^3)$

For a particle partly immersed in a melt at a depth of x, 0 ≤ x ≤ 2R, the total interface energy ($G_{interface}$) was calculated from Equation 2 and Table 2-2.

$$G_{interface} = (R - x)^2 \pi \sigma_{1v} + 2R\pi x \sigma_{1p} + 2R\pi(2R - x)\sigma_{pv}; \quad \textbf{(Equation 2-2)}$$

Equilibrium depth (x_{eq}) and reinforcement contact angle (θ) can be calculated as follows;

$$x_{eq} = R\frac{\sigma_{1v}+\sigma_{pv}-\sigma_{1p}}{\sigma_{1v}}; \quad \textbf{(Equation 2-3)}$$

Where σ is the interface tension specified by the indices: 1 = liquid Al, p = solid SiC particles and v = vapour

$$\theta = 90^o + \arcsin(\frac{R-x_{eq}}{R}); \quad \textbf{(Equation 2-4)}$$

$$\Delta G_{barrier} = \sigma_{(x=x_{eq})} - \sigma_{(x=2R)}$$ **(Equation 2-5)**

$$= \frac{\sigma_{1V}+\sigma_{1P}-\sigma_{PV}}{\sigma_{1V}}\pi R^2 \;;$$ **(Equation 2-6)**

$$v_{min} = \sqrt{\frac{3}{2\sigma_{1v}R\rho_{SiC}}}\left(\sigma_{1v}+\sigma_{1p}-\sigma_{pv}\right);$$ **(Equation 2-7)**

For particle to overcome the surface barrier and move further into the melt, the initial velocity of the particle must be higher than the V_{min} depicted by Equation 2-8.

$$v = \sqrt{v_0^2 - v_{min}^2}$$ **Equation 2-8**

Table 2-2: Energy at the interfaces of oxidised and unoxidised aluminium in Al/SiC [59]

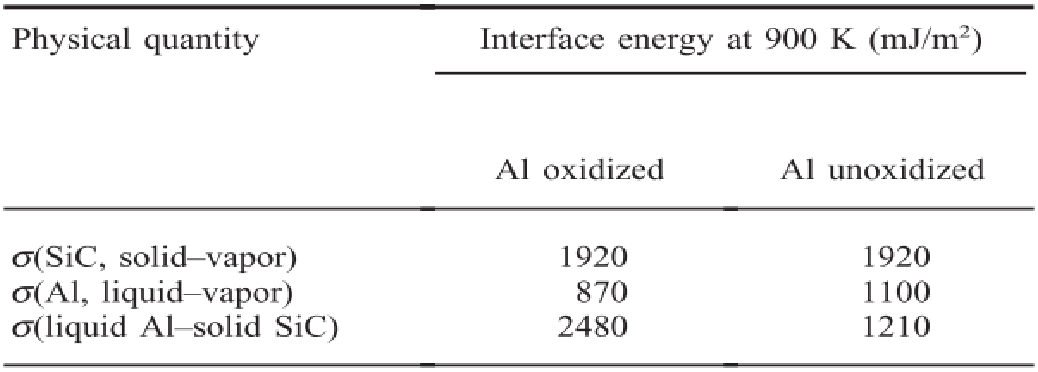

Physical quantity	Interface energy at 900 K (mJ/m^2)	
	Al oxidized	Al unoxidized
σ(SiC, solid–vapor)	1920	1920
σ(Al, liquid–vapor)	870	1100
σ(liquid Al–solid SiC)	2480	1210

2.4.2 Microstructural Interfacial Reactivity of AMCs

The general working behaviour of composites is influenced by the properties at the interface between the matrix and reinforcement [34,50,53,71], which can significantly affect the strength at the interface, thus the deformation and fracture of the composite. In addition, interfacial reactivity between the matrix and reinforcement can also change the metallurgy of the matrix alloy to affect basic properties such as melting point and mechanical strength [34].

Shorowordi et al. [50] conducted an investigation on the microstructure and interfacial characteristics of SiC, Al_2O_3 and B_4C reinforced Al composites by stir casting. The authors found a clear interfacial reaction layer at the interface of Al-SiC, whereas no reaction products were identified at the interface of Al_2O_3 and B_4C. The main issues with Al-SiC infiltration processing routes are with the considerable amount of residual porosity and the formation of deleterious reaction products (Al_4C_3, Al_4SiC_4). It has also been found that the stability of composites is affected by the temperature [67,71]. In the case of Al-SiC composites, as the temperature exceeds the melting point of Al (i.e. 660°C), SiC becomes thermodynamically unstable and reacts with the molten aluminium to form the products Al_4C_3 and Si (see Equation 2-9). Al_4C_3 product is unstable and can damage the matrix severely after longer reaction times [39]. Not only does it damage the matrix but can also slowly react with moisture from the atmosphere to form aluminium hydroxide [67].

$$4Al_{(L)} + 3SiC_{(S)} \longrightarrow Al_4C_{3\,(S)} + 3Si_{(S)}$$ **Equation 2-9**

Vreeling et al. [72] also conducted studies on the failure mechanisms associated with Al-SiC produced by laser melt injection. The authors identified four distinctive failure mechanisms on the fracture surface using SEM. They included: decohesion between Al-matrix and Al_4C_3, cracking of SiC particles, decohesion of particles (SiC) from matrix and ductile fracture of the aluminium matrix characterised by dimples. The study showed that the presence of Al_4C_3 was critical for crack initiation and propagation as shown in Figure 2-17.

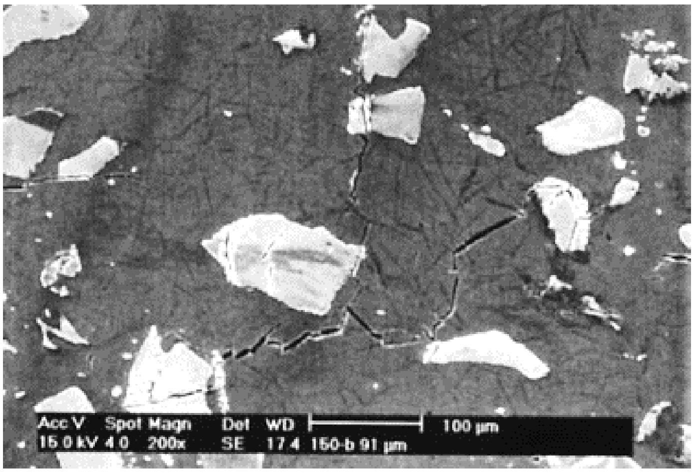

Figure 2-17: Crack initiation and propagation through Al_4C_3 and in SiC reinforcement particles [72]

Nonetheless, from the chemical reaction (Equation 2-9), a way to suppress Al_4C_3 formation in Al-SiC is to use high Si content aluminium [34,67]. This can help to overcome the formation of aluminium carbide products. Figure 2-18 [12] shows the required increase in Si content to avoid formation of reaction products for longer processing rate. On the other hand, the spray deposition technique is not susceptible to these effects because of its shorter processing time [34]. This also explains the reason why aluminium carbide is not formed in powder based processes.

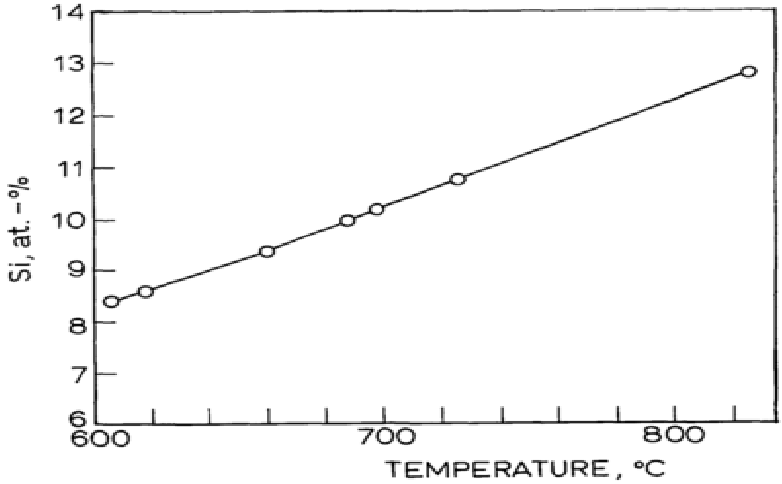

Figure 2-18: Required Silicon level to avoid aluminium carbide formation [34]

2.4.3 Mechanical properties

Particle size and weight fractions have been identified as crucial in determining the final properties of composites since the reinforcement bears a major portion of the load [8,19,51]. It has been shown that the yield stress is maximum at 15 % SiC volume reinforcement [34] (Figure 2-19). According to Lloyd [34], this could be due to the difficulties in mixing high reinforcement volume fractions.

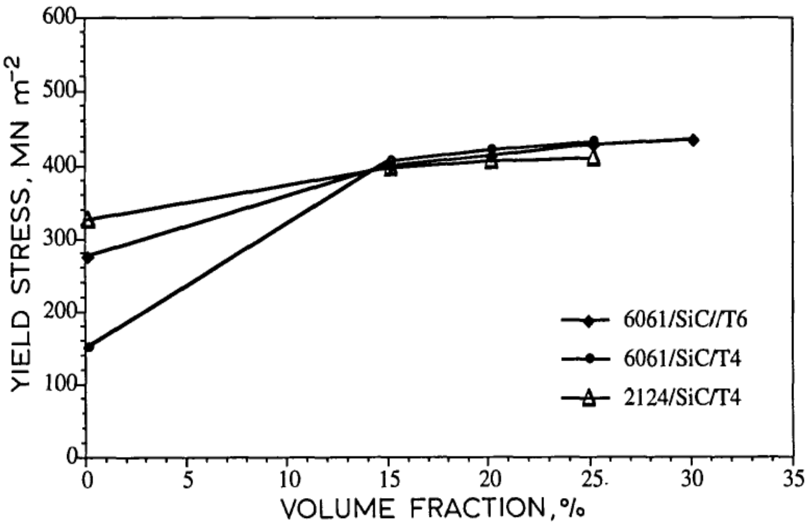

Figure 2-19: Yield stress versus % volume fraction of SiC reinforced in aluminium [34]

Meena et al. [8] also conducted an investigation into the mechanical properties of Al-6063 (Al-Mg-Si) matrix reinforced with SiC particles of different sizes produced using a resistance induction furnace. The authors found that increasing particle sizes between (37 µm and 74 µm) and weight fractions between (5 % and 20 %) increases the ultimate tensile strength and hardness respectively. Neelima et al. [73] also conducted studies on the effect of percentage (%) SiC volume fraction on the mechanical properties of Al-SiC. The authors also found that increasing the % volume fraction of SiC between 5 % and 20 % increased correspondingly the ultimate tensile strength with a maximum at 15 % volume fraction (see Table 2-3). On the other hand, maximum elongation was found in 20 % SiC volume fraction.

Table 2-3: Effect of % SiC volume fraction on UTS and Elongation of Al-6063 [73]

% SiC	**UTS (N / mm^2)**	**Elongation (%)**
5	80.84	5.42
10	88.11	5.92
15	94.21	5.57
20	83	6.87

Kok [38] conducted studies on Aluminium 2024 matrix reinforced with Al_2O_3 particles (10 % volume to 30 % volume) using the vortex processing technique.

The author found that the hardness and tensile strength of the produced composites increased with decreasing size (particles sizes 16 µm, 32 µm and 66 µm) and increasing weight fraction of the particles. A similar trend was identified by Nagaral et al. [74] in their study on the effect of Al_2O_3 on the mechanical and wear behaviour of 6061 Al alloy metal matrix composites (see Figure 2-20). The authors also found that increasing % volume fraction of Al_2O_3 (particle size = 125 µm) decreases the % elongation of the composite. The authors also observed that introduction of Al_2O_3 particles in the matrix led to a corresponding decrease in grain size as the reinforcement acted as sites for nucleation during solidification.

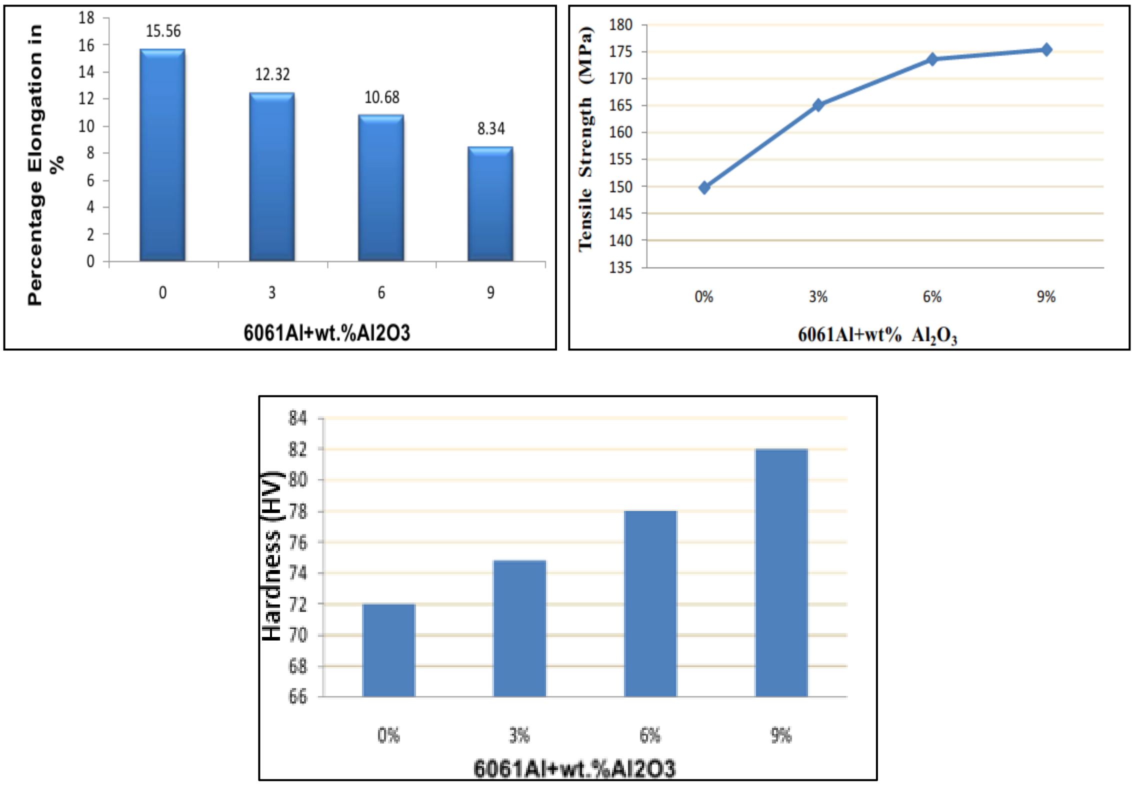

Figure 2-20: Effect of Al_2O_3 reinforcement volume fraction on tensile strength and hardness [74]

Suragimath & Purohit [19] studied the effect of fly ash (SiO_2, Al_2O_3, CaO) as reinforcement on the tensile strength of aluminium SiC (5 % SiC). Table 2-4 shows the results of their studies. This indicates the possibility of using fly ash which is an industrial waste for Al composite production.

Table 2-4: Tensile test results for Al-Si matrix reinforced with SiC and Fly ash (adapted from [19]**)**

Sample	UTS (N/mm^2)	Elongation (%)
Al-Si12	175.74	7
AlSi12 + 5% SiC + 5% Fly ash	182.64	5
AlSi12 + 5% SiC + 15% Fly ash	238.26	4

The fracture behaviour of MMCs is dependent on particle strength and interfacial strength, and failure will only occur within the particles if the interface has a higher strength than the particle strength [5]. Hence, a brittle failure transpires and results from shear localisation of fractured particles. Conversely, if the strength of particles is greater than interfacial strength, this results in decohesion of particles which leads to a ductile shear failure.

According to Lloyd [34], the main mechanical property which is improved in particle reinforced composites is the modulus of elasticity. The author identified that the quantitative measurement of the elastic modulus is dependent on the method of measurement. Dynamic measurements were found to give larger values than static measurements. On the other hand, static values can be measured in tension or compression. However, the difficulties in measurements results from the difference in thermal expansion between the matrix and reinforcement. These are affected by the presence of thermal residual stresses. For SiC and Al_2O_3 reinforcements, the Al matrix undergoes tension. This is because plastic flow occurs in tension when the composite is loaded. The total strain is made up of both the elastic and plastic components. Figure 2-21 depicts the increasing trend seen in modulus of elasticity of Al-SiC as the volume fraction of SiC reinforcement particles increases [34]. Al-SiC composites have also been found to show improvement in elastic modulus to that of unreinforced composites at high temperature, Figure 2-22. This makes them better candidates for high temperature application [75].

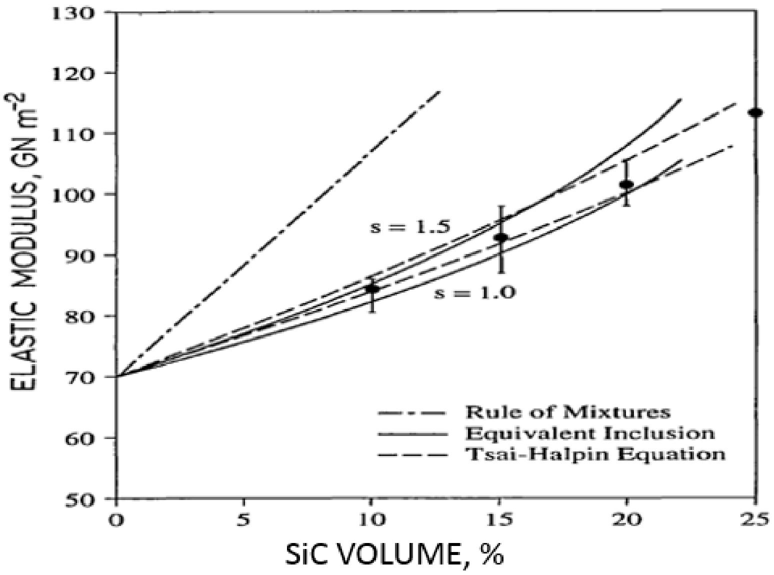

Figure 2-21: Effect of SiC reinforcement volume fraction (%) on elastic modulus [34]

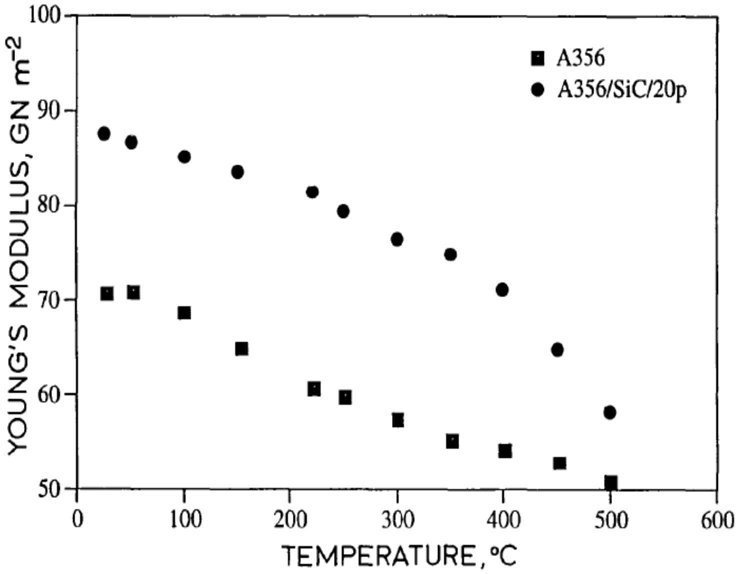

Figure 2-22: Temperature effect on elastic modulus for reinforced and unreinforced aluminium [34].

2.4.4 Composite strengthening mechanisms

In designing and selection of materials for engineering applications, consideration is given to the yield strength and ductility of the material. These properties are improved by the various strengthening mechanisms:

- Orowan strengthening: Occurs when closely spaced particles act as obstacles to dislocation motion. This increases the yield strength considerably if particles are highly dispersed [1,70].
- Hall – Petch (grain refinement): Reinforcement particles can act as heterogeneous nucleation sites in the molten matrix during solidification. This leads to improvement in grain refinement. Reinforcement particles can hinder recrystallisation when secondary processes such as hot rolling are applied. This occurs due to the grain boundary pinning effect of reinforcement particles [34,76].
- Load bearing effect: This involves the transfer of load from the matrix to reinforcement under external loads. Due to the excellent interfacial bond between reinforcement and matrix, MMCs exhibit better load bearing capacity than unreinforced aluminium alloys [76].

2.5 ADDITIVE MANUFACTURING (AM)

Additive Manufacture (AM) is a novel fabrication technique which produces near-net-shaped components and parts in a layer by layer fashion usually starting on a base plate as opposed to machining from a solid block using subtractive methods [15,16,77–79]. AM enhances short-lead times and design flexibility as well as overcoming extensive machining and the high cost of manufacturing. The qualities above makes AM a good approach for producing parts and components made of expensive materials such as nickel and titanium.

AM systems consist of a heat source, a motion system and a feed stock. Deposition of material (feed stock) layer by layer is achieved by focusing a heat source such as laser, electron beam or electric arc with the help of a motion system [16,80]. The most commonly used AM processes for depositing metallic components are powder bed fusion and directed energy deposition processes (see Figure 2-23). The material feed stock used in metal AM processes are typically metal powder and metal wire.

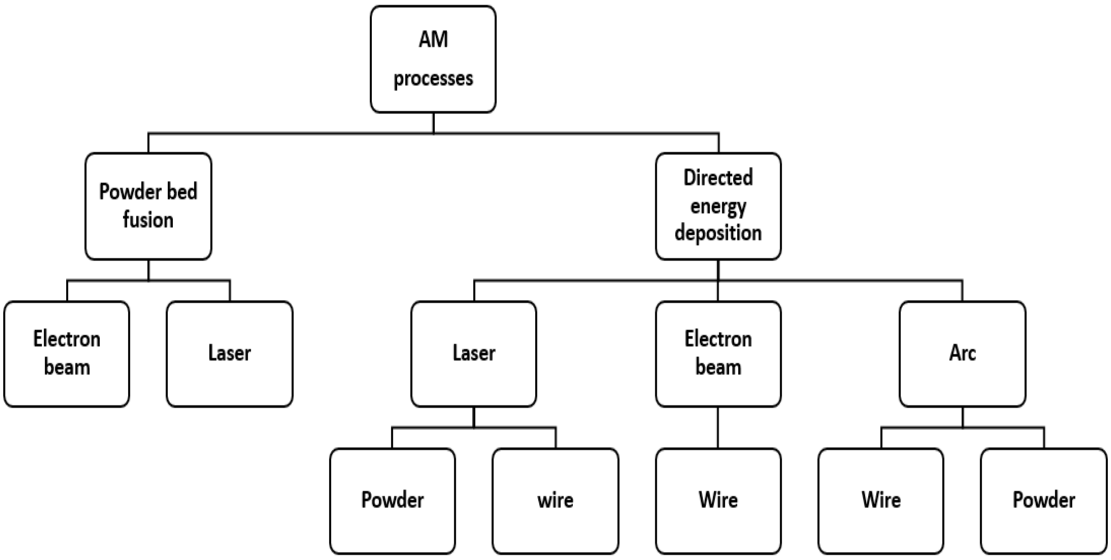

Figure 2-23: **Classification of additive manufacture processes**

2.5.1 Powder bed fusion (PBF)

Powder bed fusion processes (PBF) employ a laser or electron beam as a heat source. The heat source is used selectively to scan and melt partially or fully already spread powder in an additive fashion. PBF is conducted in an inert atmosphere to provide shielding for the liquid metal. After the heat source scans one layer, the building chamber piston goes down whereas the powder chamber piston goes up to the set layer thickness. Subsequently, the roller spreads powder across the build chamber to be scanned again by the heat source and this continues layer by layer until the part is complete. Figure 2-24 shows schematic of the PBF process. Common PBF processes include selective laser melting, selective laser sintering and electron beam melting.

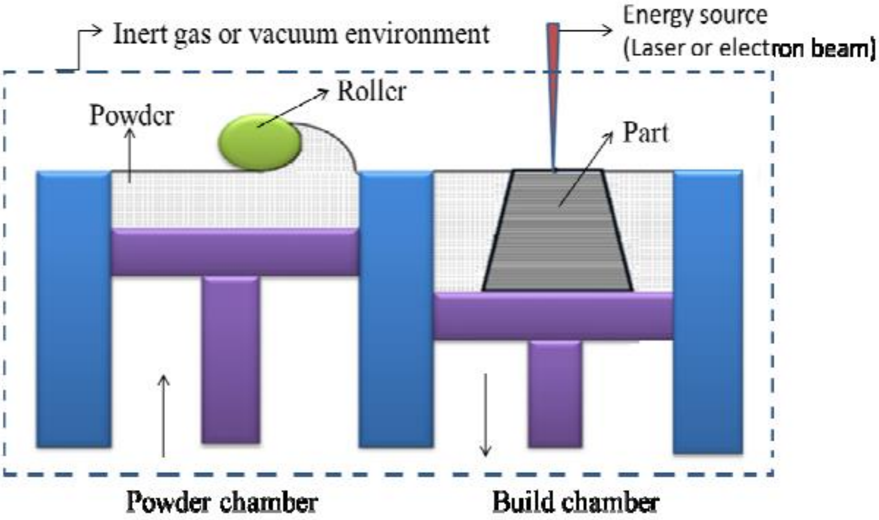

Figure 2-24: Powder bed fusion process [14]

An advantage of PBF process is its ability to build parts with high dimensional accuracy [14,16]. PBF has also been used in producing functionally graded parts [81]. Nonetheless, PBF processes are expensive and limited by its chamber to producing smaller built volumes (maximum: 500 mm x 350 mm x 300 mm). In addition, PBF processes have very low deposition rate 10 g/min [16] in comparison DED processes.

2.5.2 Directed energy deposition (DED)

In direct energy deposition, an energy source is used to melt powder or wire which is fed in the region of the heat source. DED has been classified into three groups based on the energy source. They include laser, electron beam and electric arc based processes. Figure 2-25 shows a schematic of direct laser deposition using powder as feed stock. Wire feed AM processes are 100 % efficient based on the material usage since all the wire is melted during component manufacture. In addition, there is minimum risk of exposure to harmful fumes in wire feed AM processes as compared to powder feed processes. The deposition rate of wire feed processes is also much higher (330 g/min) than powder feed processes and this allows medium to large components to be produced at a minimum cost [16]. For this reason, the research will focus on wire feed AM processes.

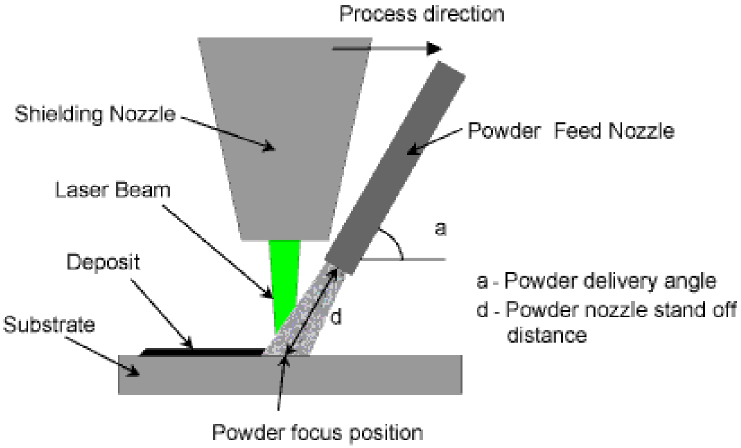

Figure 2-25: High speed direct laser deposition [82]

2.5.3 Wire feed processes

In the previous section, wire feed DED processes have been found to be more economical and good for building medium to large volume components. The current wire feed systems investigated for metal AM processes include:

- Wire and laser additive manufacture (WLAM);
- Electron beam freeform fabrication (EBFF) and
- Wire + arc additive manufacture (WAAM)

WLAM is a metal additive manufacture process that uses laser as energy source, wire as feed stock and a robot or CNC machine as a motion system. In WLAM, the laser is used to generate a melt pool on the substrate with subsequent feeding of wire to be melted in an additive fashion for part and components to be produced. Figure 2-26a shows the schematics of WLAM process. The main limitations of WLAM are low deposition rate (<1 kg/hr) and low energy efficiency (2-5%) [16].

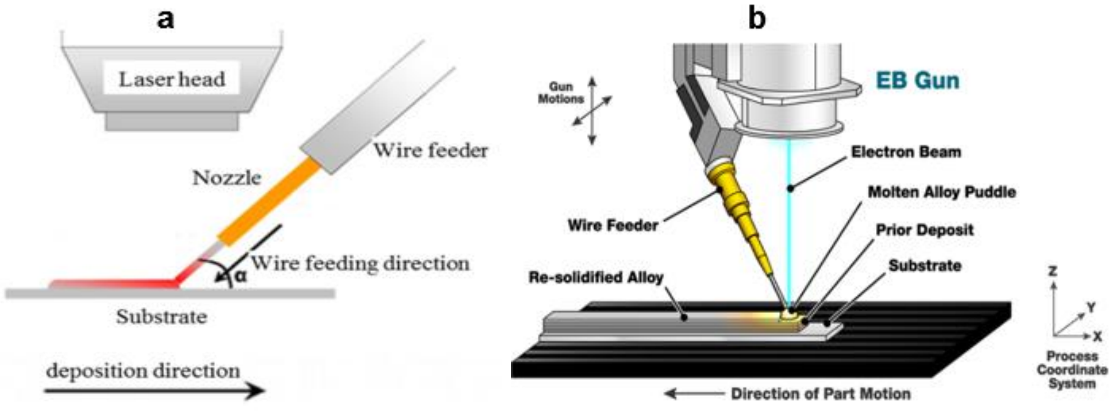

Figure 2-26: Schematic diagram of (a) WLAM and (b) EBFF [83,84]

EBFF process (Figure 2-26b) has also been found to produce parts of higher build up rates (over 2500 cm^2/hr) due to its high energy density in combination to high scanning speeds [16]. The process feeds wire into a melt pool created by electron beam in vacuum and are very effective for extremely reflective materials such as aluminium and copper. Nevertheless, EBFF process is also characterised by poor surface qualities and also limited to the size of its chamber [14].

Wire + arc additive manufacture (WAAM) has gained research interest because of its low cost, excellent efficiency and deposition rates in comparison to WLAM and EBFF [15,85–88]. WAAM processes use an electric arc as heat source to melt wire layer by layer on a substrate. A number of research works have investigated WAAM process using MIG, TIG and Plasma arc as heat source. WAAM processes also use computerised numerically controlled gantries or robotic systems and can be performed in and out of chamber as shown in Figure 2-27 [89].

Figure 2-27: WAAM set – up (a) in open air; (b) in an enclosure

WAAM has been used in building medium to large parts and components for a number of materials such as titanium, steel, aluminium and many more. Figure 2-28 shows WAAM parts which have been produced in Cranfield University using titanium, steel and aluminium wire by plasma and CMT WAAM.

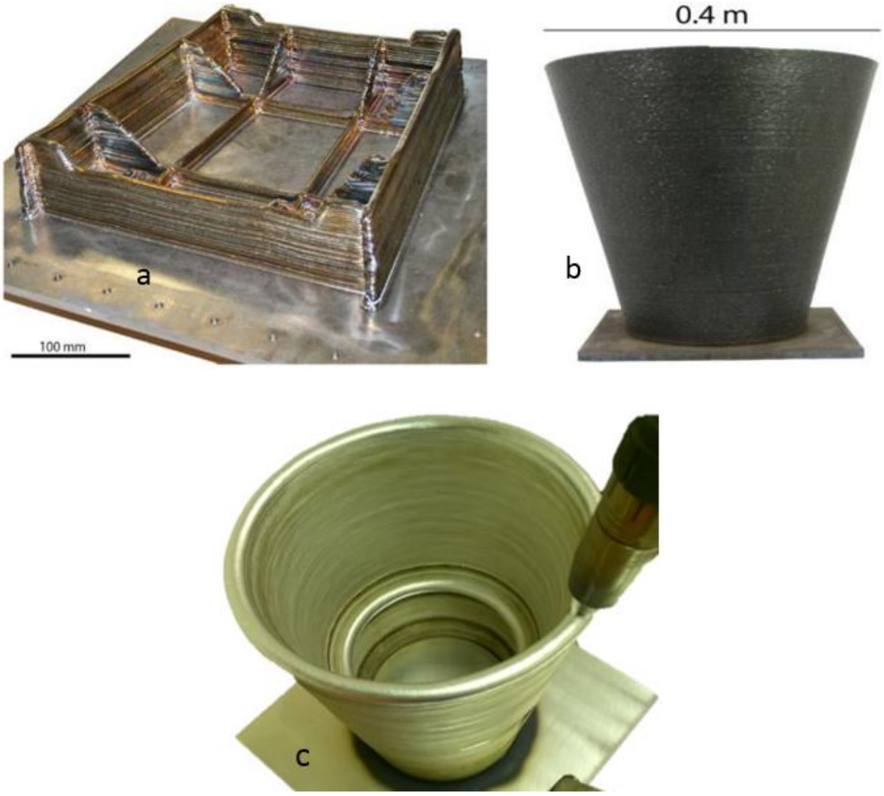

Figure 2-28: Parts produced by WAAM at Cranfield University: (a) 24Ti-6Al-4V external landing gear assembly; (b) mild steel truncated cone (c) Aluminium complex cone

A number of parameters have been identified to affect wire + arc additively manufactured part geometry [86,90]. These include the wire feed speed, travel speed, current, voltage and the wire diameter. These parameters affect the melt geometry during part and component manufacture.

2.5.4 Aluminium Wire + Arc Additive Manufacture (Al-WAAM)

WAAM of aluminium alloys have been investigated by numerous researchers to identify suitable processes for producing aluminium parts and their corresponding properties [91–96]. The commonly used WAAM deposition techniques been used in deposition of aluminium include tungsten inert gas (TIG) [95,96] and metal Inert gas (MIG) [91–94] processes.

2.5.4.1 TIG WAAM

In TIG-WAAM process, wire melting and deposition is achieved by striking an arc between a tungsten (non-consumable) electrode and the substrate [15,16]

(Figure 2-29). Generally ferrous metals such as stainless steel have been welded with the direct current electrode connected to the negative part of the power source. In this condition, the current is conducted by plasma, partly by ions and primarily by electron emission from tungsten electrode (thermionic emission) [23].

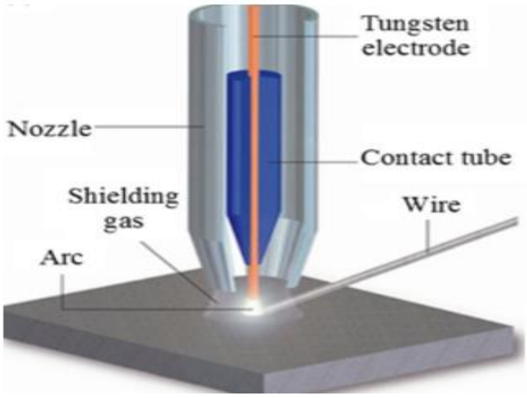

Figure 2-29: TIG Process [16]

Conversely, this is not the case for non-ferrous metals such as aluminium and magnesium due to the oxide layer (Al_2O_3) which forms on the surface of these materials [26]. These oxides have a high melting temperature of about 2050 ^oC and must be removed to facilitate good bonding during welding [97]. Therefore, aluminium alloys have been welded by the use of alternating current (AC) with TIG process. During ACTIG welding, Al_2O_3 oxides are removed by cathodic cleaning in the electrode positive (% EP) part of the AC cycle. % EN is not suitable for welding aluminium alloys even though they can achieve very high temperatures. Figure 2-30 compares % EN and % EP with respect to the contact area between the arc and the work piece. It can be seen that the contact area between the arc and surface is higher in the anode sleeve (A1) than cathode sleeve (A2) [97]. This is because cathode sleeve is fixed at a point and despite its ability to achieve high temperature, minimal wear is achieved [97]. Conversely, A2 has a higher energy density than A1. % EP behaves differently to that of % EN. In this state, the plate is the main supplier of electrons by establishing a strong electrical field known as field emission. During field emission, the cathode sleeve which is located at the point of the electrode begins to move randomly. This promotes the removal of oxides which forms on the surface of aluminium. Nonetheless, this feature also makes the arc unstable and enhances the wear of electrode. Therefore, it is difficult to maintain a process connected exclusively to % EP. Hence, the alternating current have been used which balances the % EP to % EN to enhance both fusion and cleaning.

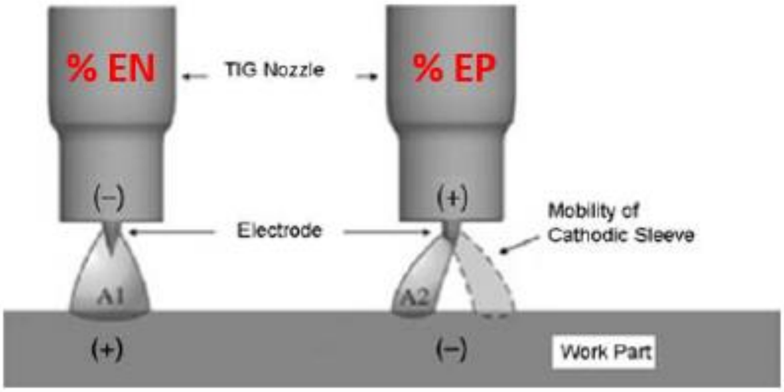

Figure 2-30: Effect of % EN and % EP on voltaic arc [97]

The fusion behaviour during variable polarity ACTIG welding of aluminium has been investigated [97–99]. The authors found that increasing the electrode positive polarity of the AC cycle increases the weld bead width and penetration (Figure 2-31). Furthermore the possibility of producing aluminium WAAM parts using ACTIG has been shown by Bai et al. [95] in their studies on the mechanical properties of aluminium 2319 linear walls.

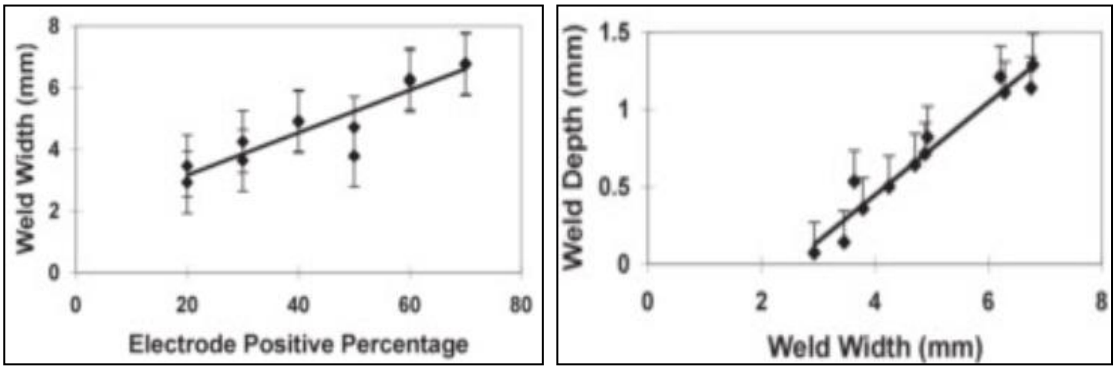

Figure 2-31: Effect of % EP on width and depth of a melt bead [98]

2.5.4.2 MIG WAAM

In MIG-WAAM, deposition is achieved by the striking of an arc between a consumable wire electrode and the substrate in an inert atmosphere (Figure 2-32). A number of research studies have been focused on cold metal transfer

(CMT), a MIG process variant in WAAM of aluminium due to its low heat input, high deposition rate and low spatter thereby enhancing its ability to control droplet transfer and dilution [91–93,100]. The process deposits filler materials mainly by surface tension transfer when the arc is on as the filler travels into the weld pool. The arc is finally extinguished by lowering the welding current to zero and the wire is retracted by the backward movement [101].

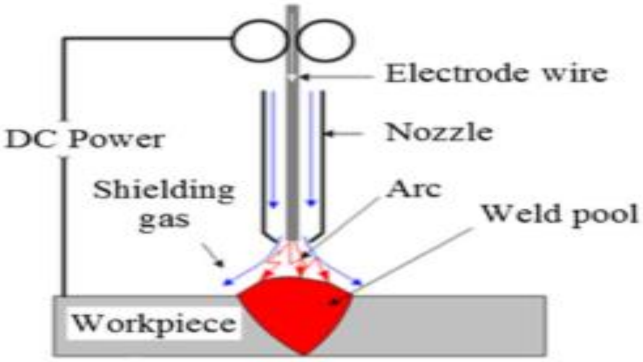

Figure 2-32: MIG Process [16]

Cong et al. [93] conducted studies on the different arc modes of CMT process on porosity and found the CMT pulse advance process to be the best as it was characterised by fine microstructure and almost zero porosity. Gu et al. [91] also conducted studies on the strengthening effect of interlayer cold working and post deposition heat treatment using the CMT - PA WAAM. The authors found that both work hardening and T6 heat treatment increase strength and hardness (Figure 2-33). Cong et al. [94] further conducted a comparative study between thin and block structures using CMT processes and found that the large thermal mass showed higher hardness values (Figure 2-34). This was as a result of the increase in number of grain boundaries from the fine microstructure.

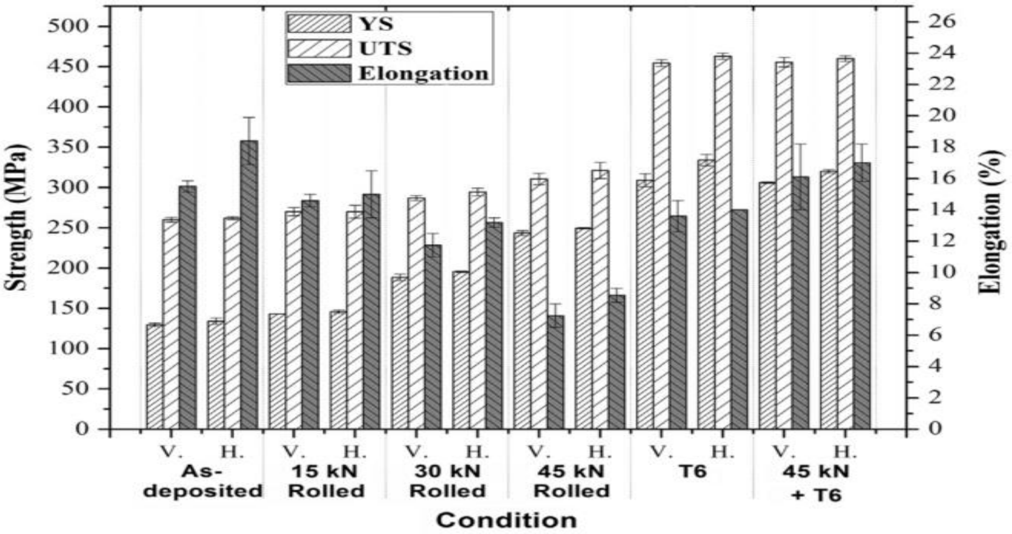

Figure 2-33: Tensile properties of as-deposited, interlayer rolled and T6 heat treated WAAM of linear walls [91]**.**

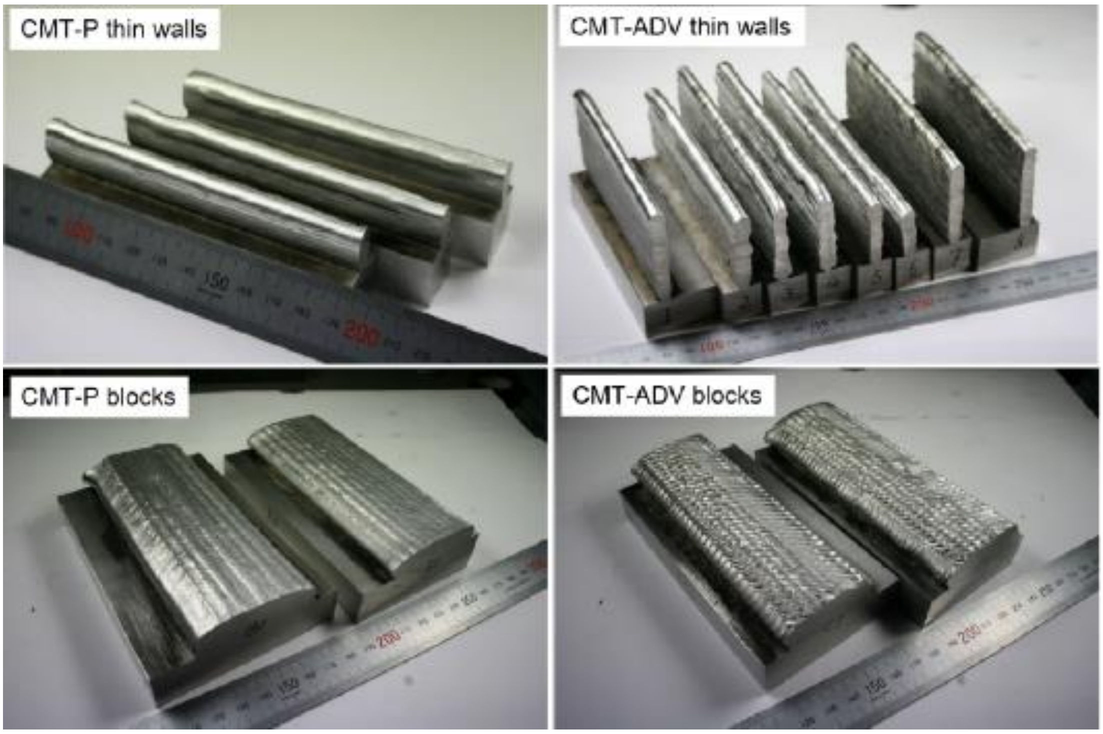

Figure 2-34: Aluminium WAAM thin and block structures [94]

2.6 Weldability of Aluminium Alloys

Generally, aluminium is considered to be of lower weldability compared to steels [102]. This results from the material's high thermal and electrical conductivity, thermal expansion, affinity to atmospheric gases and solidification range. The above mentioned properties makes aluminium alloys susceptible to defects such as porosity, hot cracking and stress corrosion cracking [23,102,103]. In view of this, to avoid such defects, various measures have been adapted such as: shielding the weld pool from atmospheric gases by using inert gases (Ar; He) and the use of high power density processes to reduce weld thermal cycles.

2.6.1 Porosity in Al-WAAM

Porosity poses a serious problem in Al-WAAM and so it is important to understand the mechanisms by which it forms and the methods for reducing them in WAAM [92,93]. Porosity is mainly caused by hydrogen contamination which results in formation of bubbles in molten aluminium as it tries to escape before solidification [93]. These bubbles are trapped if they are unable to escape in time before the molten metal solidifies. Therefore, the higher thermal conductivity of aluminium increases the cooling rate which results in trapping gas bubbles [103]. Nevertheless, porosity in Al-WAAM can be reduced by cleaning and removal of the oxide layer of the substrate prior to deposition and by using a low current and short arc length (low heat input process) such as the CMT process. Cong et al. (2014) investigated the different transfer modes of CMT on porosity using Al - 2319 wire on wrought 2219 (T851) substrate. The CMT pulse advance arc mode was found to be the most suitable in terms of porosity due to its effective oxide removal, low heat input and fine equiaxed grain structure. The authors believed that the process combined the advantages of CMT-P and CMT-ADV process. In addition, the authors again found that the reduction in porosity was also because of the competition during heterogeneous nucleation of grains, dendrite growth and pore nucleation rate.

2.7 Physics of metal transfer and governing parameters for producing Al-SiC

In arc welding, a number of parameters affect the quality and rate of deposition [26,104]. In view of this, there is the need to understand the physics of the arc (arc forces) and their effect on melt pool behaviour. This will be important during AMC production by WAAM to be able to identify the key factors for successful injection of particles into aluminium melt. The principal forces that affect the flow of the melt pool include: buoyancy; Lorentz force; Marangoni convection and arc plasma shear stress. For the purpose of the study, Marangoni convection and plasma shear stress have been reviewed due to their considerable effect on the melt pool behaviour.

The melt flow direction due to Marangoni convection depends on surface tension gradient [105]. According to Kou [104] surface tension of molten metal decreases as temperature increases in the absence of surface active agents. In view of this, the warm melt pool of low surface tension is pulled outward by the colder melt pool of high surface tension (Figure 2-35 a; b). This causes the surface tension gradient to induce an outward shear stress at the surface of the melt pool thereby causing the liquid metal to flow from the centre to the edge of the melt surface.

The movement of plasma at a high speed on the surface of melt pool can also induce a shear stress on the melt surface [104,106]. The existence of arc plasma shear stress is due to the fact that arc plasma possess kinetic energy and momentum [106]. This causes the melt pool to flow from the centre to the edge and below the surface of the melt when the arc plasma strikes (Figure 2-35 c; d). Although force generated by the Plasma jet is not comparable to surface tension, according to Wang et al. [106] the arc plasma could increase significantly for higher arc length processes.

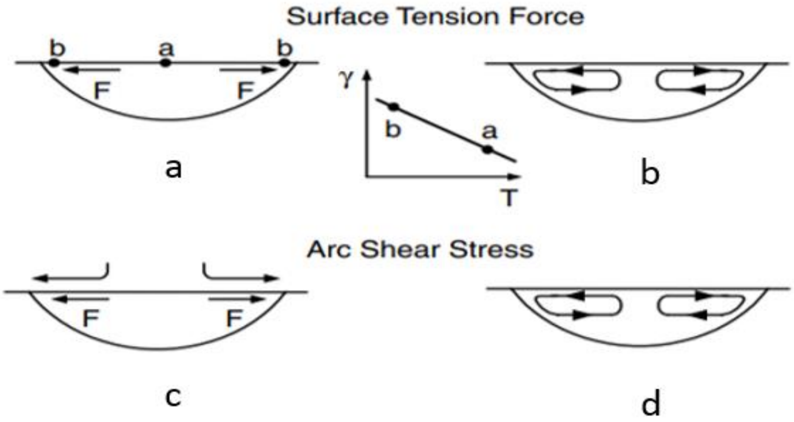

Figure 2-35: Effect of Marangoni convection and arc plasm shear stress on melt pool behaviour [104]

2.7.1 Shielding gas

During TIG and MIG deposition, shielding gas not only provides a protective shielding for the arc but also influences the final melt geometry due to its specific effects on melt and droplet transfer. The common shielding gases used in aluminium welding are Ar and He with pure Ar being the most frequently used in GTAW and GMAW welding [107]. A number of studies have also been conducted on the effect of Ar and He mixture on detachment, transfer and impingement on the workpiece. Rao et al. [108] studied the effect of shielding gas composition on metal transfer and plasma arc in MIG welding. The authors found that increasing the helium content of the shielding gas resulted in an increase in droplet size with a decrease in droplet detachment frequency. The authors explained that this is affected by the high thermal conductivity of He gas which produces a larger hot arc core as compared to Ar. Murphy et al. [109] also modelled the effect of mixing shielding gases in GTAW. The study revealed that addition of hydrogen or nitrogen increases the shear stress and arc pressure but decreases with addition of helium. In addition the study also revealed that addition of He, H and N also increases the flux density close to the centre of the anode which in turn increases melt penetration depth. Campbell et al. [110] also derived the forces acting on the melt pool as a result of He/Ar mixed shielding gases in GTAW process. The following conclusions were made:

- He produces a higher plasma shear stress to that of Ar;

- Ar has a higher Lorentz force than He; with Ar having a greater Lorentz force at the core while He showed a greater Lorentz force at the outer core;
- Ar shows a greater arc plasma force than He;
- He has a stronger Marangoni convection than Ar.

Dong et al. [111] conducted studies on the effect of welding parameters on melt pool convection and melt bead geometry in He shield environment. The study indicated that Marangoni convection decreases with increasing welding speed and electrode gap. The authors also found that increasing the current increases the electromagnetic force which enhances the inward convection of the melt.

Peasura and Watanapa [112] conducted studies on the effect of shielding gas on Al 5083 alloy mechanical property and microstructure. Their studies indicated that He shielding gas had higher heat input than Ar shielding gas which contributed to larger grain sizes and a reduction in hardness. He gas is associated with higher ionisation energy and higher thermal energy which explains the increase in heat input [112,113].

2.8 Summary of Literature Review

The following research areas have been reviewed as part of the literature review preceding this research:

- Aluminium matrix composites (AMCs) manufacturing techniques
- Aluminium wire + arc additive manufacture (Al-WAAM)

Table 2 summarises findings on the production techniques of aluminium matrix composites by detailing a brief description in addition to processing benefits and limitations.

Table 2-5: Benefits and limitations of solid and liquid processing routes

Processing Route	Description	Benefits	Limitations
Solid fabrication processes (powder metallurgy and diffusion bonding)	These processes feed particles into a mould of preferred shape and then pressure applied to enable further compaction of the powder by cold pressing. Subsequent heating at low temperature below the melting point of the powder can facilitate bond strength.	Overcomes wetting difficulty between ceramic particles and molten metal	Complex process; Long processing time; Difficulty in handling highly reactive powders; Expensive process
Liquid fabrication process (casting, and liquid infiltration)	These techniques use a furnace to melt the molten metal which is then poured around reinforcing particles in a mould. Process developments such as pressure infiltration and Vortex or stir casting have been used to improve upon the issues with wettability, interfacial reactions and particle distribution.	Economical Efficient process Ease of handling liquid metal	Often displays inhomogeneous distribution of particles; Difficulty of reproducing parts and components (due to the limited control of process parameters); Detrimental interfacial reactions

It has been found that Liquid fabrication techniques have been used extensively in Al-MMC manufacturing because of their low cost of manufacture and the ease of handling the liquid Al metal. Nevertheless, they are limited by structure reproducibility and inhomogeneous distribution of particles due to the limited control of process parameters. In addition, their long processing times also results in formation of reaction products which may be detrimental to aluminium alloys. Therefore there is a need to use a shorter melt processing methods for manufacturing MMCs.

The laser melt injection (LMI) process, a shorter time processing technique has also been reviewed for production of AMCs. However, the process is difficult to achieve and limited to a narrow operating area owing to the high reflectivity of laser beam by aluminium.

Wire + arc additive manufacture has been identified as a potential process for production of aluminium matrix composites. From the review, the main process variants which have been used in aluminium WAAM include the TIG and MIG processes.

2.8.1 Research Gap

The review has shown that Wire + arc additive manufacture (WAAM) has not been used in production of aluminium matrix composites. However, its ability to produce repeatable parts or components to near net shapes may be a way out to overcome the limitations of conventional liquid fabrication techniques (such as inhomogeneous distribution of particles, structure reproducibility and elimination of detrimental products). Furthermore, the effect of shielding gas type (Ar or He) on heat input and WAAM wall geometries has not been conducted.

3 Materials and Equipment

Context:

This section presents all the equipment and materials used in the successful completion of the entire studies. This comprises of full descriptions of equipment used to enhance future repeatability and improvement of the research. These include the cold metal transfer (CMT) and tungsten inert gas (TIG) welding power sources as well as the Sulzer Metco twin powder feeder equipment. In addition, equipment used in process monitoring and metallurgical analysis have also been described. The chapter also specifies the chemical composition of all materials used and the methods adapted in their preparation prior to deposition.

3.1 Materials

The materials used in this study were aluminium matrix and particulate reinforcement materials. The matrix materials comprised of aluminium wire and substrate whereas the reinforcement material consisted of SiC particulates.

3.1.1 Matrix material

The aluminium wire grades used in the study were the non-heat treatable alloy (Al 5556) and the heat treatable alloy (Al 2319). The substrate used in the entire study was the AA 6082-T6 extruded plate. The chemical composition of the materials are shown in Table 3-1. The selected materials were based on the interesting mechanical properties as well as the associated low cost which have been achieved using WAAM.

Prior to the experiments, the material substrates were cleaned to remove dirt and grease with ethanol allowing them to dry. A glass fibre polishing disc was subsequently used to remove the oxide layer and then cleaned finally with acetone.

Table 3-1: Chemical composition of wires and the substrate materials

	Al	Si	Mg	Cr	Mn	Ti	Cu	Zn	Fe	Zr	other
Al 2319	Bal	0.20	0.02	-	0.20-0.40	0.10-0.20	5.8-6.8	0.10-0.25	0.30	-	0.15
Al 5556	Bal	0.20	4.7-5.5	0.05-0.20	0.50-1.0	0.05-0.20	0.10	0.25	0.40	-	0.15
Al 6082-T6	Bal	0.88	0.89	0.059	0.55	0.022	0.083	0.049	0.48	-	0.15

3.1.2 Particle Reinforcement

For the reinforcement, angular SiC particles were used with average sizes of 75 µm and 150 µm. Figure 3-1 shows scanning electron micrograph of the particles.

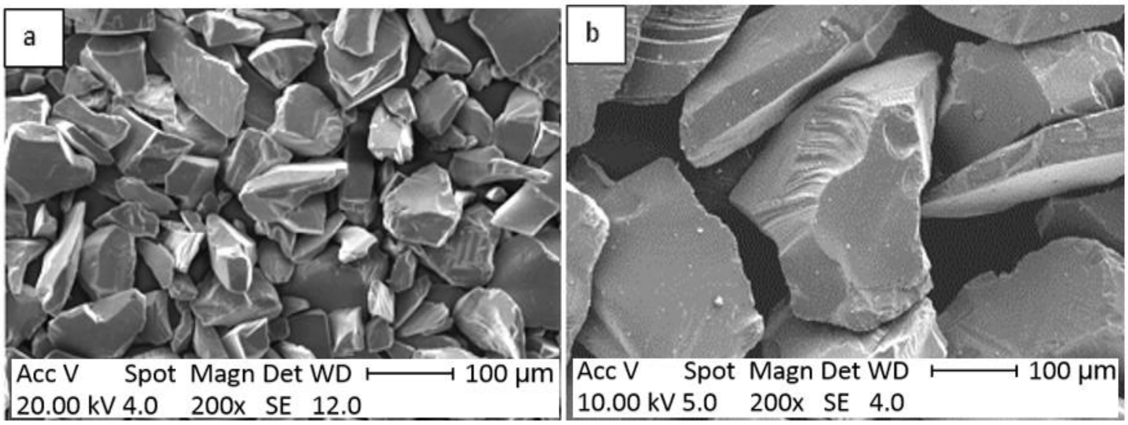

Figure 3-1: Scanning electron micrographs of SiC particles used with average particle sizes (a) 75 µm and (b) 150 µm

3.2 Equipment

3.2.1 Cold metal transfer (CMT) set-up for WAAM

The Fronius cold metal transfer (CMT) advanced 4000R power source (Figure 3-2) was used in the pulse and pulse advance CMT mode. This was used with the IRB2400 ABB robot with contact tip to work distance (CTWD) of 13.5 mm. A pure argon shielding gas with flow rate of 25 L/min was used to provide the protective environment.

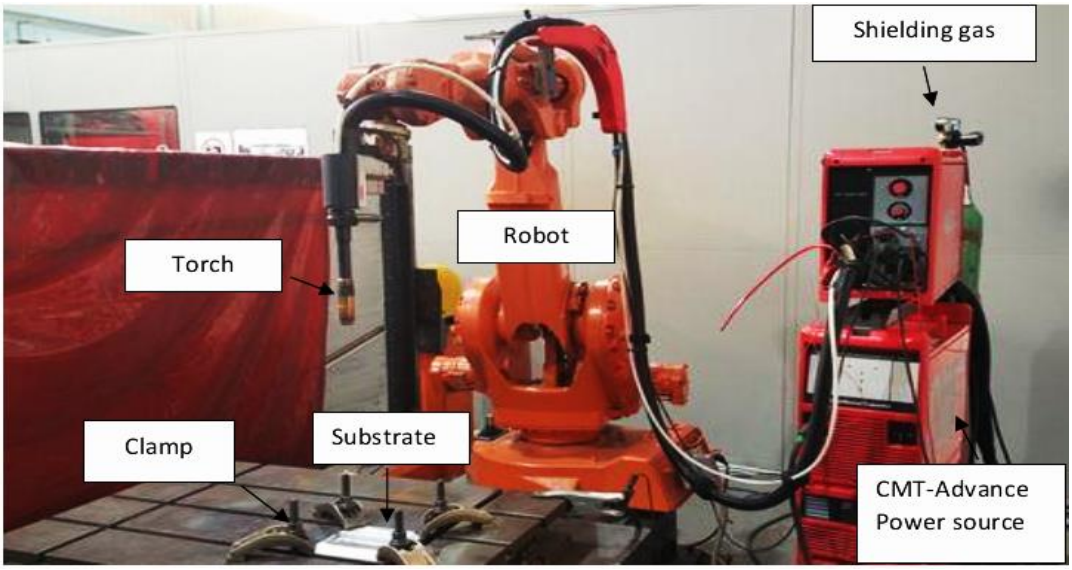

Figure 3-2: Cold metal transfer WAAM experimental set-up

The AMV4000 was used to measure the transient data (current and voltage) and monitor the recordings of the wire feed sensor from which the average WFSs were calculated (Figure 3-3). The relationship between the set wire feed speed (WFS) and the actual WFS during welding was determined (Figure 3-4). It can be seen that a linear correlation was achieved between the set wire feed speeds (WFSs) and the measured average WFSs for wire feed speed to travel speed ratios (WFS/TS) of 10 and 20. However it can also be seen that there is small deviation downwards of the measured WFS compared to the set WFS as the WFS increases.

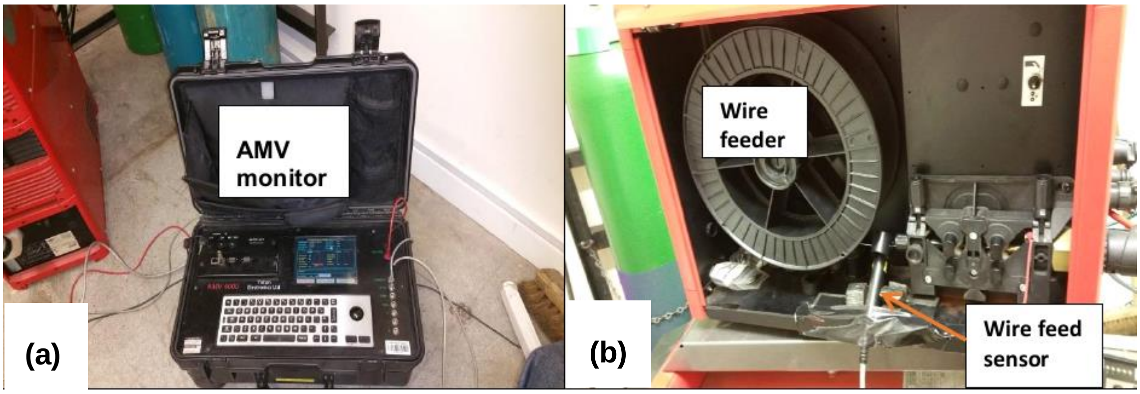

Figure 3-3: Wire feeding monitoring set-up. (a) AMV monitor; (b) Wire feed system

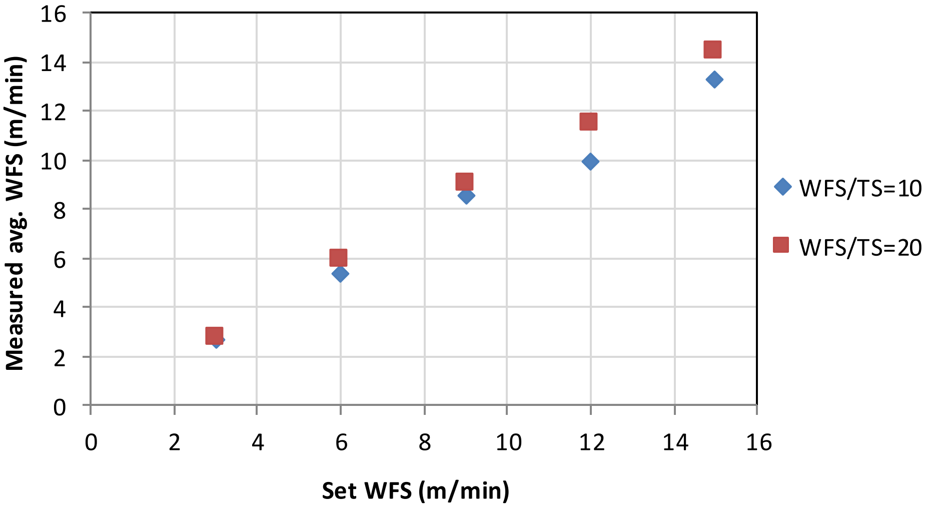

Figure 3-4: CMT wire feeder calibration

3.3 Tungsten Inert Gas Welding Set-up (TIG) for WAAM

The Migatronic TIG commander 330 AC/DC power source was used with the Trio axis motion system CNC. A multi-strike tungsten electrode of diameter 3.2 mm was used. This was set to have an arc length of 5 mm perpendicular to the substrate. Figure 3-5 illustrates the ACTIG WAAM set-up used in this study. The wire was fed from the front to align with the centre of the electrode by touching the substrate. Argon shielding gas at a flow rate of 15 L/min was used as the protective environment. A cooling system placed underneath the substrate was used to cool down the substrate to room temperature between layers.

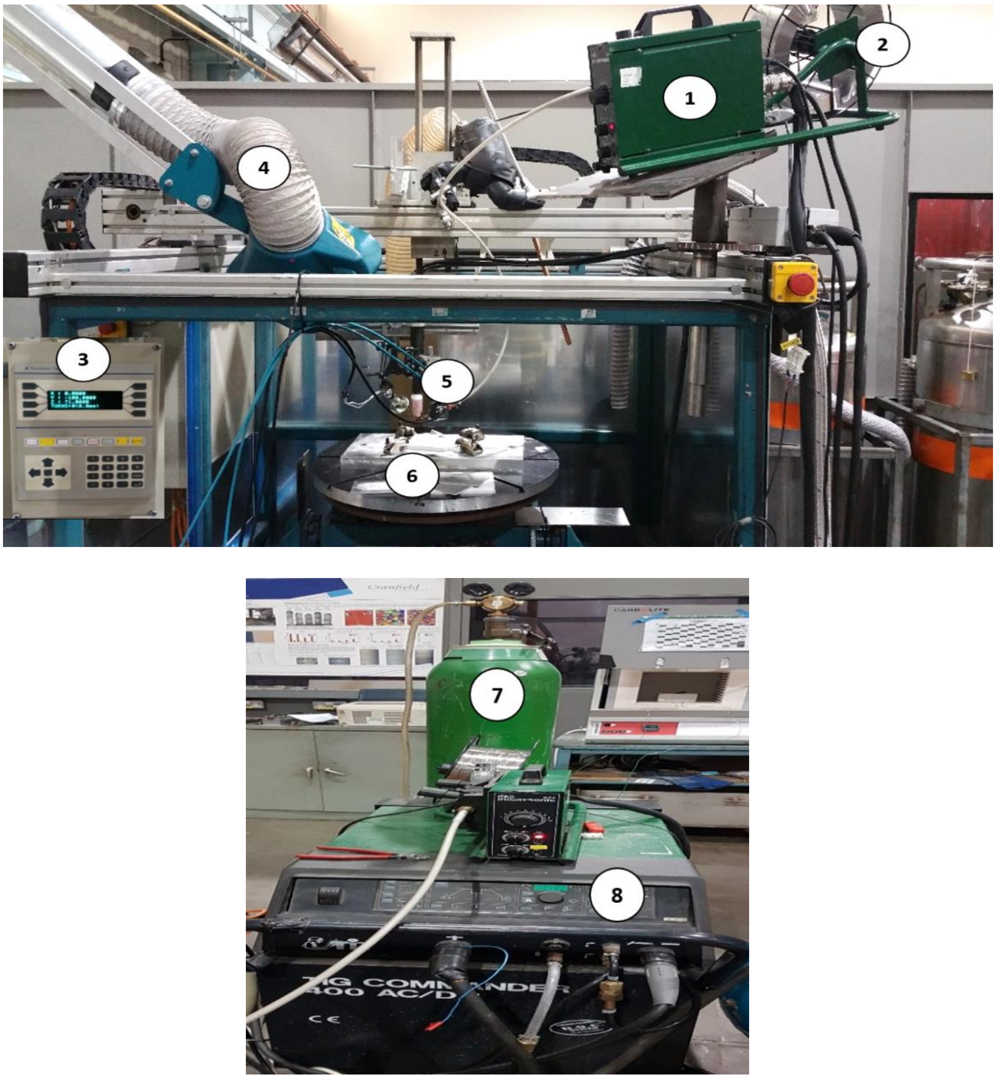

Figure 3-5: ACTIG WAAM set-up in Trio axis motion system rig: (1) wire feeder; (2) Al wire; (3) Controller; (4) gas extractor; (5) torch; (6) table; (7) Ar shielding gas; (8) TIG power source

Prior to the experiment, the KT-4 wire feeder was calibrated to determine the relationship between the set wire feed speed and the actual wire feed speed. A linear correlation was established between the set wire feed speed and the actual wire feed speed (Figure 3-6). Furthermore, the relationship between the set current and the recorded current (actual current) of the power source was also monitored using the AMV monitoring system. This monitoring also identified a linear correlation between the set current and the actual current recorded (Figure 3-7).

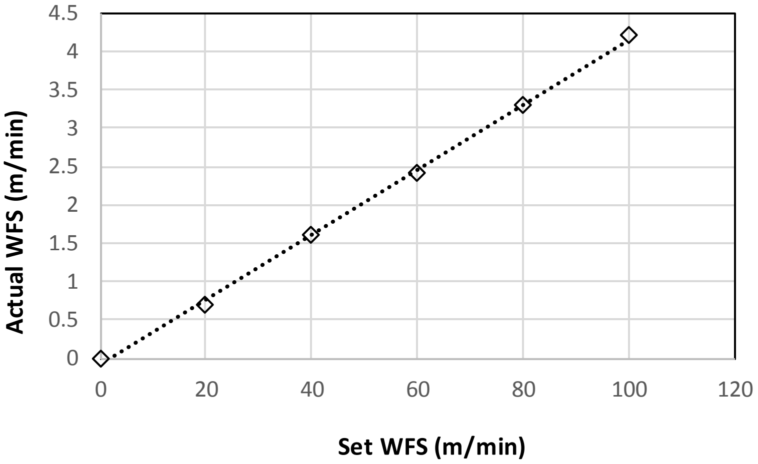

Figure 3-6: KT4 wire feeder calibration

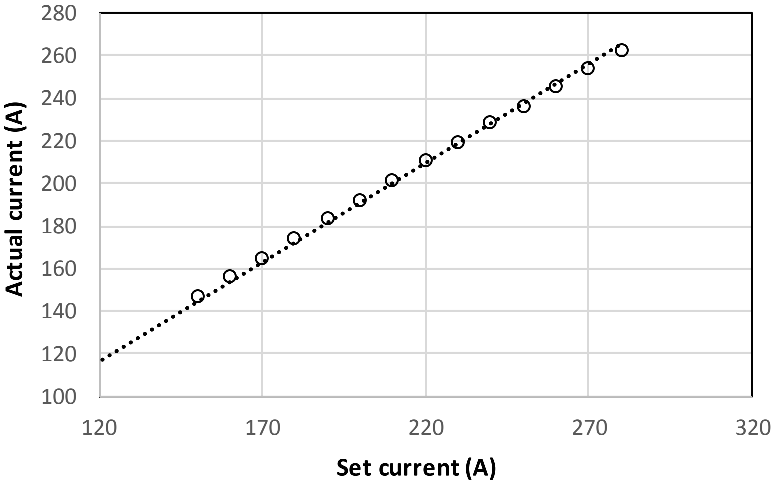

Figure 3-7: Relation between set and actual current for the TIG Migatronic power source

3.4 Powder feeder set-up

Figure 3-8 illustrates the WAAM set-up used in the production of aluminium matrix composites. The Migatronic TIG commander 330 AC/DC power source described in Section 3.3 was used with the IRB2400 ABB robot. The ceramic powder was delivered using the Sulzer Metco TWIN-10-C R2 powder feeder. The powder injection system works either by using argon, helium or nitrogen shield gas. The system also enables the possibility of feeding two powders at the same time. However, in this study, Ar gas was used as the carrier gas and only one feeding system was utilised. The flow rate of the system is in normal litre per minute and was converted to Ar litre per minute using the chart displayed in Figure 3-9.

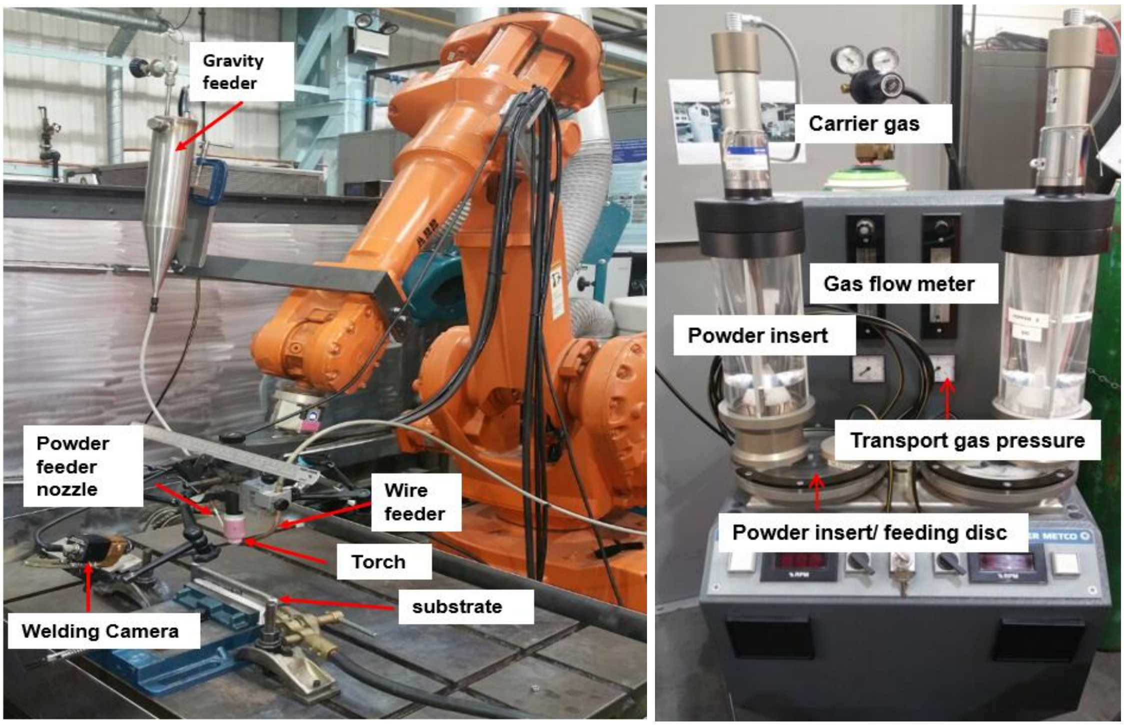

Figure 3-8: WAAM set-up for aluminium matrix composite production (left) and Sulzer Metco TWIN-10-C R2 powder feeder (right)

The powder system has a stirrer which allows the homogenous distribution of particles during the injection process. The powder feed rate was also adjusted by regulating the speed of the feeding disc. The rotation speed represents an equivalent feed rate in grams per minute (g/min). In view of this, the actual feed rates were calibrated for both fine particles (avg. size: 75 µm) and coarse particles (avg. size: 150 µm), Figure 3-10; 3-11. The feeder disc employed was the NL

16/1.2 for higher feed rates. The calibration was done by feeding SiC particles into an empty container for 30 sec (0.5 min) and subsequently measuring the mass (M_2) using a digital scale. The mass of particles fed was calculated by subtracting the initial mass of the container (M_1) from M_2. The powder feed rate was calculated from Equation 3-1.

PFR = ($M_2 – M_1$) g / 0.5 min **Equation 3-1**

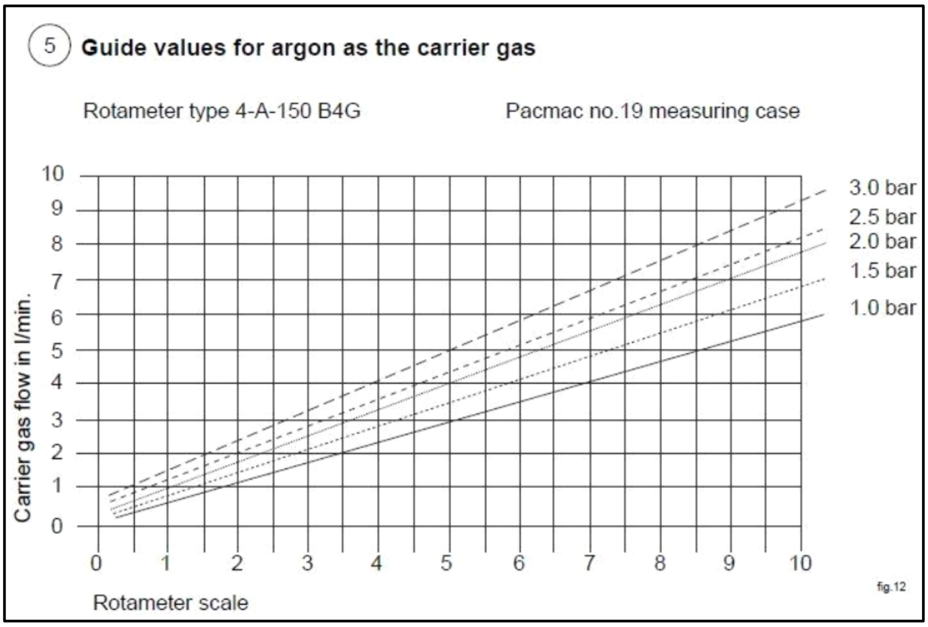

Figure 3-9: Flow chart for converting from NLPM to Ar litre per minute

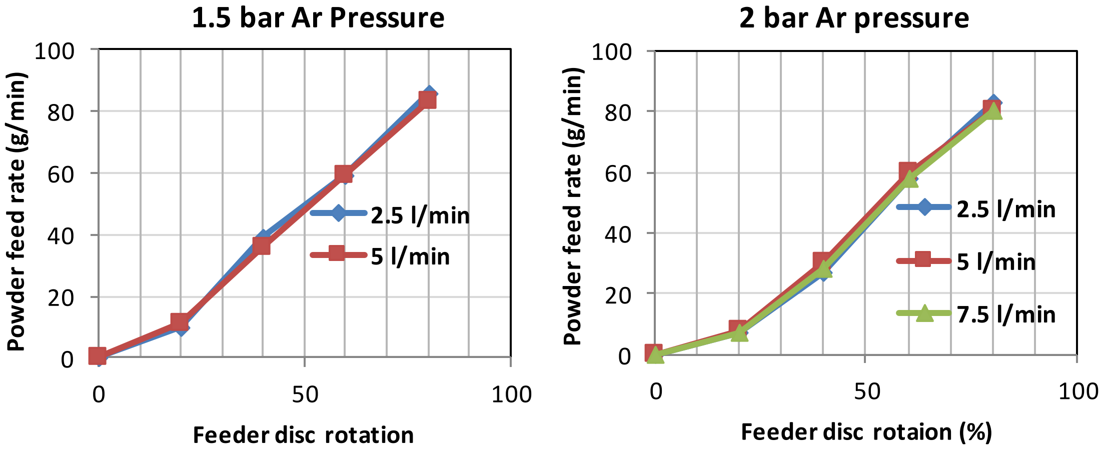

Figure 3-10: 75 µm SiC feeder calibrations plotted against feeder disc rotation with an Ar transport gas flow rate from 2.5 l/min to 7.5 l/min.

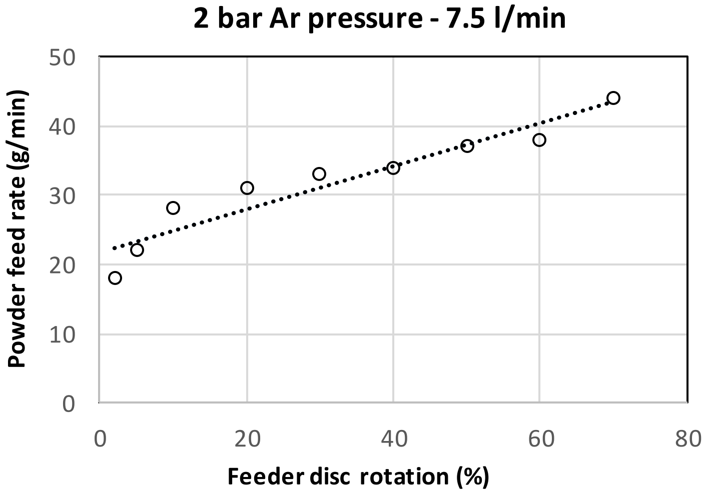

Figure 3-11: 150 µm SiC feeder disc rotation speed versus powder feed rate for 150 µm SiC particles

Most of the experiment were conducted using a designed gravity feeder (Figure 3-12) to reduce the injection gas pressure used in transporting the particles. This hopper was designed to release the Ar gas pressure after the particles are conveyed into it to further transport particles through the outlet to the powder nozzle (Figure 3-13). The powder nozzle consist of a copper tube and an aluminium oxide ceramic tube (Al_2O_3) which can resist the high heat of the process. This was the last point of particle injection into the melt pool.

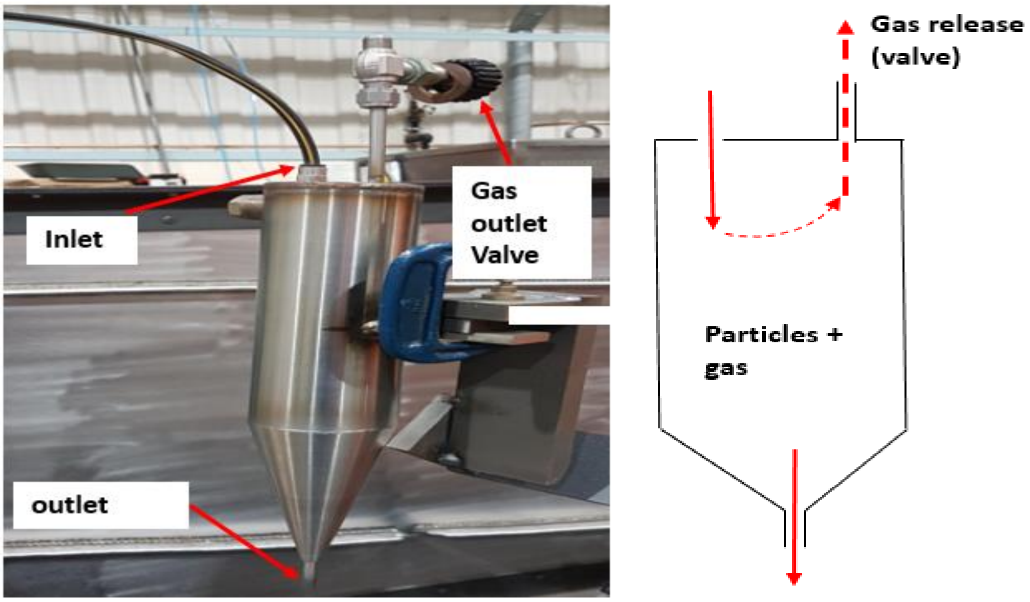

Figure 3-12: Powder gravity feeder

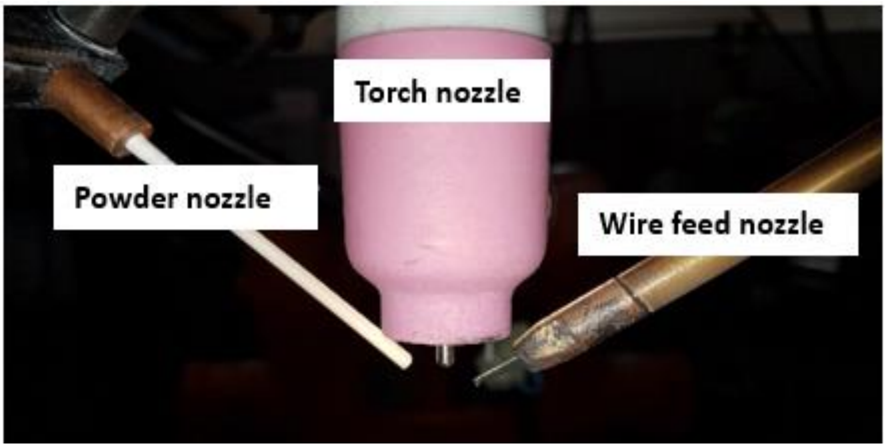

Figure 3-13: Set-up configuration for the injection process perpendicular to the substrate

3.5 Metallographic preparation

All metallographic samples were prepared and examined in the Metallurgy laboratory at Cranfield University. Samples were cut using the vertical and horizontal band saw and subsequently sectioned using the Struers Discontom-60 machine. This was set to a cutting speed of 0.60 m/min to prevent overheating and severe damage to the samples which result with high cutting speed. Samples were then mounted either by cold mounting using epoxy or hot mounting. Subsequently, samples were ground with the following SiC grit papers: 240, 600, 1200 and 2500 using an automatic grinding and polishing machine (Figure 3-14). This was then polished to mirror finish using 3 µm diamond paste and 1.5 µm colloidal silicon suspension. Furthermore, prior to microstructure analysis, samples were etched with Kellers etchant as shown in Table 3-2.

Table 3-2: Etchant used and methods

Etchant	Composition	Method
Kellers Etch	190 ml distilled water, 5 ml Nitric acid, 3 ml Hydrochloric acid, 2 ml Hydrofluoric acid	The surface of samples were wiped with soaked cotton wool for 10 - 30 s and then washed with water.

Figure 3-14: Automatic grinding and polishing machine

3.6 Microstructure analysis

Figure 3-15 shows the equipment used in the microstructure analysis. The Nikon optihot-66 and the confocal laser scanning microscopes were used in analysing the macrostructure and microstructure after the samples were etched.

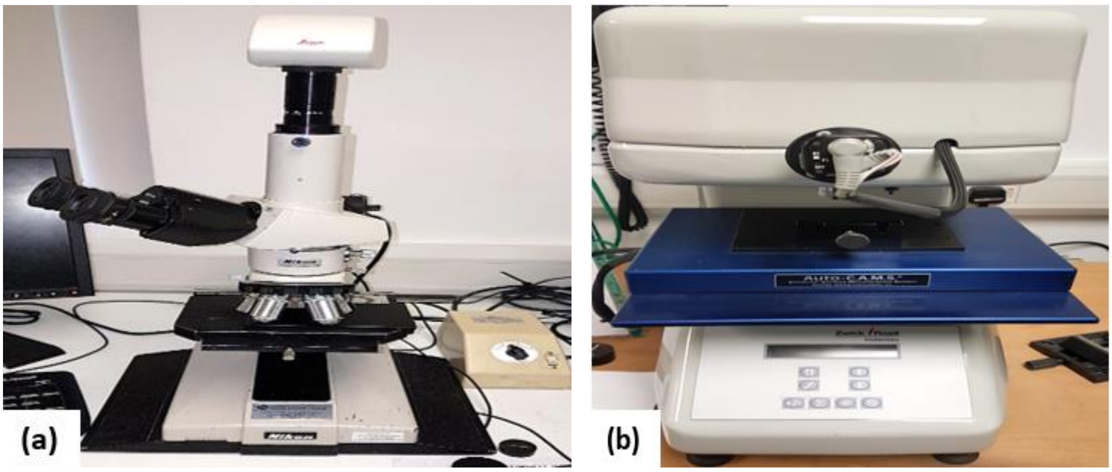

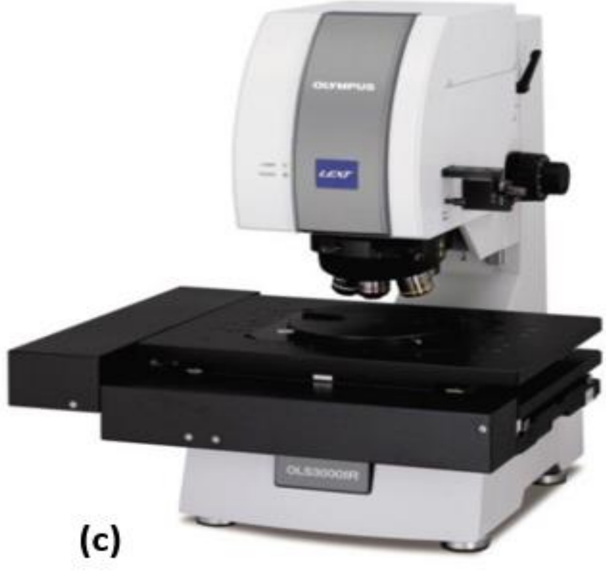

Figure 3-15: Microstructure analysis equipment (a) Nikon Optihot-66 (b) Vickers micro hardness indenter and (c) Confocal laser scanning microscope.

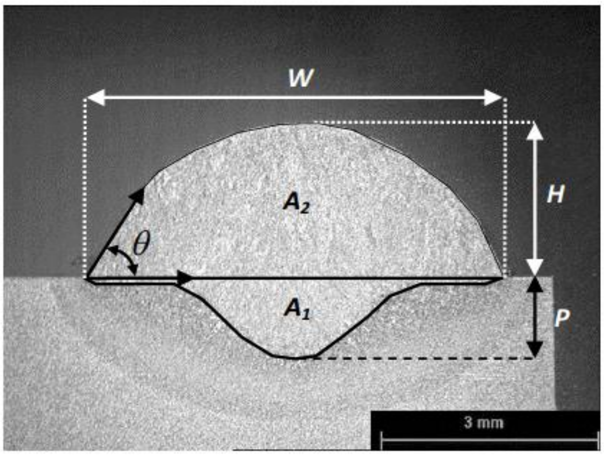

W: Bead width, (mm)
H: Bead height, (mm)
RR: Remelting ratio = A_1/A_2, (%)
P: Penetration depth, (mm)
D: Dilution = $A_1/\ A_1+A_2$, (%)
DR: Deposition rate, (kg h^{-1})
CA: Contact angle θ, (°)
A_1: Penetration area, (mm^2)
A_2: Reinforcement area, (mm^2)
AR: Aspect ratio = $H\ W^{-1}$

Figure 3-16: Single bead transverse macro cross section [90]

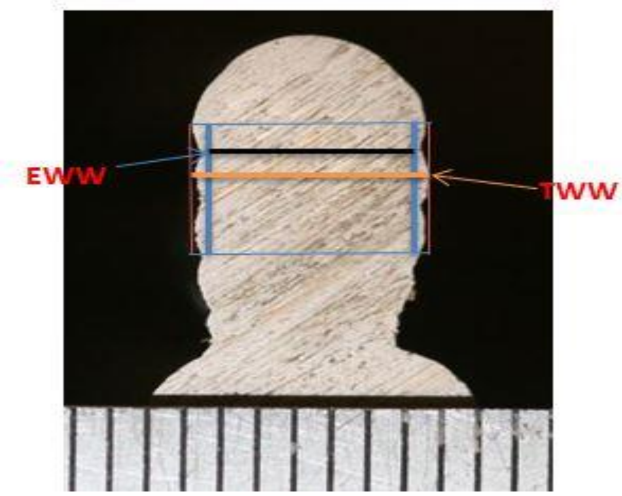

$$SW = \frac{TWW - EWW}{2} \qquad \textbf{Equation 3-2}$$

Figure 3-17: Linear wall dimensions measured

The Axiovision 4.8 software was used to measure single layer melt bead geometry as depicted in Figure 3-16. In addition, linear wall dimension were analysed by measuring the effective wall width (EWW) and total wall width (TWW) as can be seen in Figure 3-17. The Surface waviness was determined from Equation 3-2, depicting how much of material needs to be machined for accurate dimensions. In addition, pore counts were made along the middle section of transversely cut walls by using the IMAGE J software. For the hardness measurement, the Vickers micro hardness indenter (Figure 3-15b) was used by applying a load on the prepared specimen. The scanning electron microscope was also used to analyse the composition of major elements in weight % as well as the phases present in fractured surfaces.

4 Process studies of metal inert gas (MIG) deposition on aluminium wire + arc additive manufacture

This chapter includes data reported in the publication below:

Ayarkwa, K. F., Williams, S., & Ding, J. (2015). Investigation of pulse advance cold metal transfer on aluminium wire arc additive manufacturing. Int. J. Rapid Manufacturing, 5(1), 44–57.

Context:

This section reports on studies conducted on MIG process variants; CMT-pulse (CMT-P) and CMT pulse advance (CMT-PA) processes for aluminium wire + arc additive manufacture. This has been done with the view to assessing their suitability for aluminium matrix composite production. From the Literature review (See Section 2.5.1), the CMT process has been identified as suitable for Al-WAAM due to its effective control on heat input, droplet transfer and dilution. In view of this, firstly, the effect of process parameters on CMT-PA process variant was investigated for aluminium single bead linear walls. Further studies were also conducted on CMT-P process variant for multi-bead thicker section walls produced by oscillation and parallel deposition strategies.

4.1 Introduction

In the production of aluminium matrix composites, shorter processing techniques have been identified as suitable to overcome issues with formation of reaction products which may be detrimental to aluminium alloys. From the literature review (Section 2.5), wire + arc additive manufacture (WAAM) has been identified as a potential production route. Presently, the CMT-PA process variant has been identified due to its ability to control heat input with almost zero porosity. However, the effect of CMT-PA process parameters on WAAM linear wall dimension has not been conducted.

Most studies have mainly been conducted on thin section linear walls [80,91,93]. It is also noteworthy that thin walls are limited in layer wall width during thicker component building. In WAAM, the deposition strategy plays an important role in the manufacture of parts. Therefore for thicker section walls which exceed the limit of single layer wall width, multi-layer deposition strategies have been used [94,114]. The most popular multi-layer deposition strategies are the parallel and oscillation deposition strategies. During parallel deposition, single weld beads are placed side by side to each other with an overlap increasing the size of the bead. Therefore, the arc is turned off and on at the end of every pass. On the other hand, in the oscillation strategy, there is no arc off prior to the next overlapping weld bead. Figure 4-1 depicts schematics of both oscillation and parallel multi-layer bead deposition strategies.

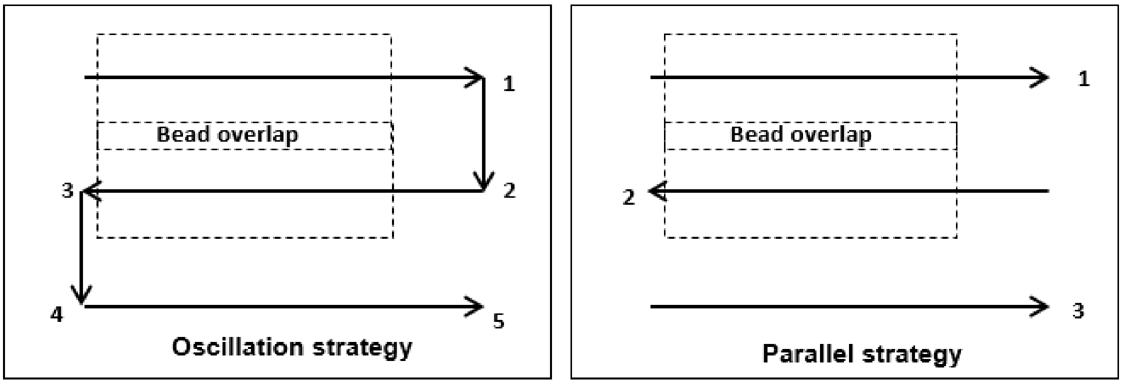

Figure 4-1: Schematics for oscillation (left) and parallel (right) deposition strategy

The advantages of the oscillation over parallel strategy include the reduction in fabrication time, process flexibility, high energy efficiency, less likely of lack of fusion defects [115]. These improve productivity and results from the continuity of the process without the arc going off during deposition. Previous studies of different strategies on titanium deposition exhibited different properties. This results because the deposition strategy has an impact on the thermal cycles which in turn affect microstructure and mechanical properties differently. However, the effect of the various deposition strategies on wire + arc additive manufacture of aluminium alloys have not been conducted yet.

In this section, the effect of CMT-PA arc mode on aluminium wire + arc additive manufacture was conducted by assessing the effect of process parameters on the effective wall width (EWW), total wall width (TWW) and layer height (LH). In addition, studies on the effect of parallel and oscillation deposition strategies on aluminium WAAM multi-layer bead walls have also been reported. The study also considered the effect on microstructure and mechanical properties.

4.2 Experimental set-up

All equipment and material compositions used in this section have been detailed in section 3. The Fronius CMT advanced 4000R power source (see Section 3.2) was used in its pulse and pulse advance modes. The material substrate and wire used were 6082-T6 (dimensions: 200 mm x 200 mm x 12 mm) and 2319 (diameter: 1.2 mm) respectively (section 3.1).

4.3 Effect of pulse advance cold metal transfer on single bead width linear walls

4.3.1 Experimental procedure

An initial working envelope was developed for CMT-PA process to identify the process limits and working range. To establish the working envelope, walls of 10 layers were built using the CMT-PA process. These walls were 140 mm long and were built with subsequent layer deposition in the opposite direction as shown in Figure 4-2. A thermocouple was used to measure the temperature of the substrate prior to deposition of subsequent layers and the AMV4000 equipment was used to measure the current and voltage. Subsequent layers were only deposited after initial layer was cooled to room temperature. The welding parameters for the first three layers were selected to account for the high cooling of the base plate prior to the actual welding parameters (Table 4-1). Consequently, layer height increments used were obtained from the average of the initial layer height taken from 4 different points 25 mm apart.

Wall quality was assessed by determining the average peak height variation of the top surface waviness of the respective walls built Figure 4-3. A Canon EOS 400D digital camera was used to take macros of walls and axiovision Rel. 4.8 software was used to measure the surface profile of the last layer of which the average variation was determined. Non-linear surface profiles characterised by 'humps' having different peak heights (variation > 0.3 mm) were tagged as unacceptable (Figure 4-3b), whereas those with approximately constant surface profiles (variation < 0.3 mm) were tagged as acceptable (Figure 4-3a). In addition, walls which were characterised by bead slipping on top of the previous layer deposited resulted in irregular side surface waviness.

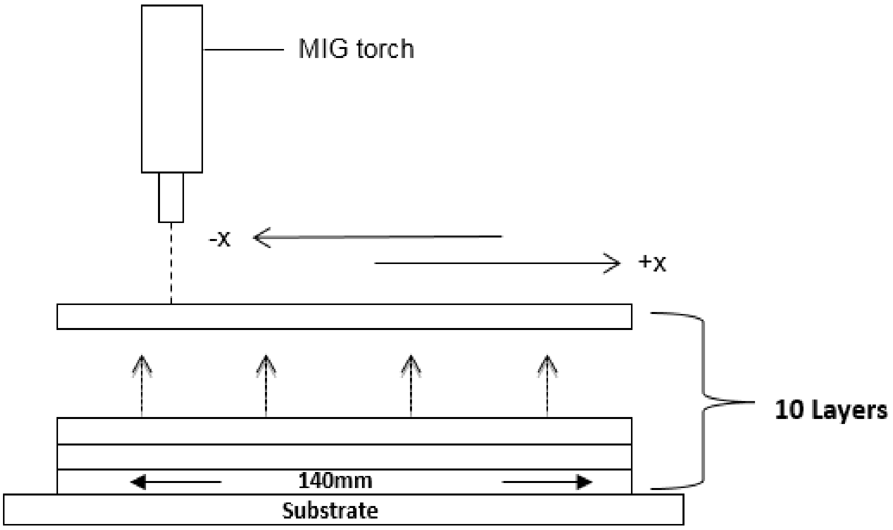

Figure 4-2: Al-WAAM 10 layer wall built on substrate with subsequent layer starting point alternating in opposite directions (-x, +x) respectively.

Table 4-1: Input process parameters

Layer number	Process	WFS (m/min)	TS (m/min)
1	Pulsed MIG	12	0.6
2	Pulsed MIG	9	0.6
3	Pulsed MIG	7	0.6
4-10	CMT-PA	x	x

Where x = actual inputs for the experiments; CTWD = 13.5 mm

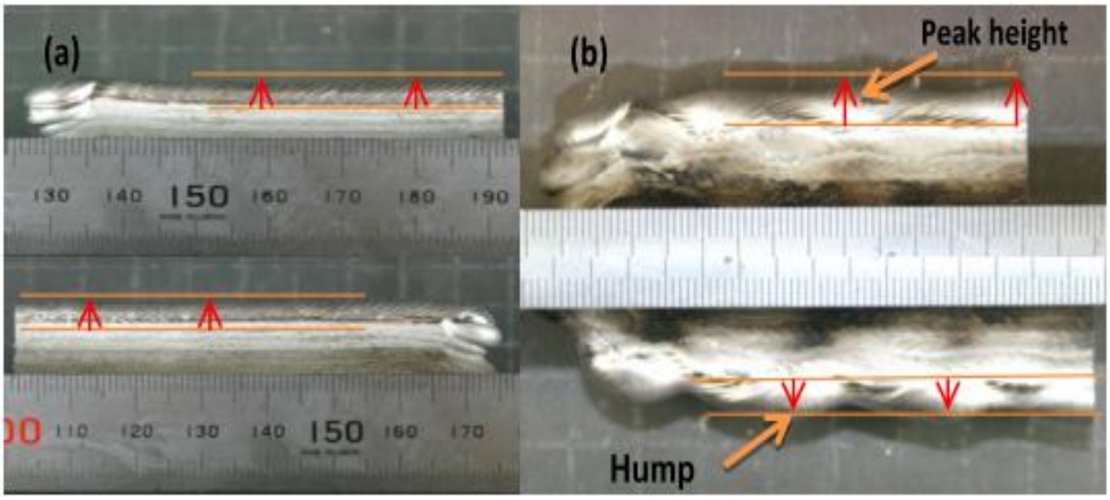

Figure 4-3: Wall Top surface profile measurements

Samples were cut using the Struers Discontom-60 machine and macros were taken using the dell camera. Subsequently, Axiovision 4.8 software was used to measure the effective wall width (EWW) and total wall width (TWW) (see Section 3.6). The Surface waviness was determined from Equation 4-1 depicting how much of material needs to be machined for accurate dimensions.

Microstructure analysis was also conducted using the optical microscope (Figure 3-16). In addition, pore counts were made along the middle section (112 mm^2) of transversely cut walls by using IMAGE J software. This was conducted for the respective wire feed speed to travel speed ratios (WFS/TSs) of 10, 15, 20 and 25 at constant WFS of 6 m/min.

4.3.2 Results

Figure 4-4 shows aluminium walls built by the cold metal transfer pulse advance (CMT-PA) process. This depicts the physical features with input wire feed speeds (WFSs) and travel speeds (TSs) used in building the walls for constant WFS/TS of 10. It can be seen that walls a, c and d, with WFSs of 4 m/min, 6 m/min, and 8 m/min respectively, were characterised by regularly shaped beads with uniform surface profile whereas b and e with WFSs of 10 m/min and 12 m/min were characterised with an uneven surface profile (humps). Figure 4-5 also shows the effect of process parameters on the average peak height variation of the wall top surface profile. It can be seen that walls characterised by uniform surface profiles have lower peak variations between 0.04 mm and 0.24 mm whereas walls characterised by uneven surface profiles had higher peak variations between 0.53 mm and 0.85 mm.

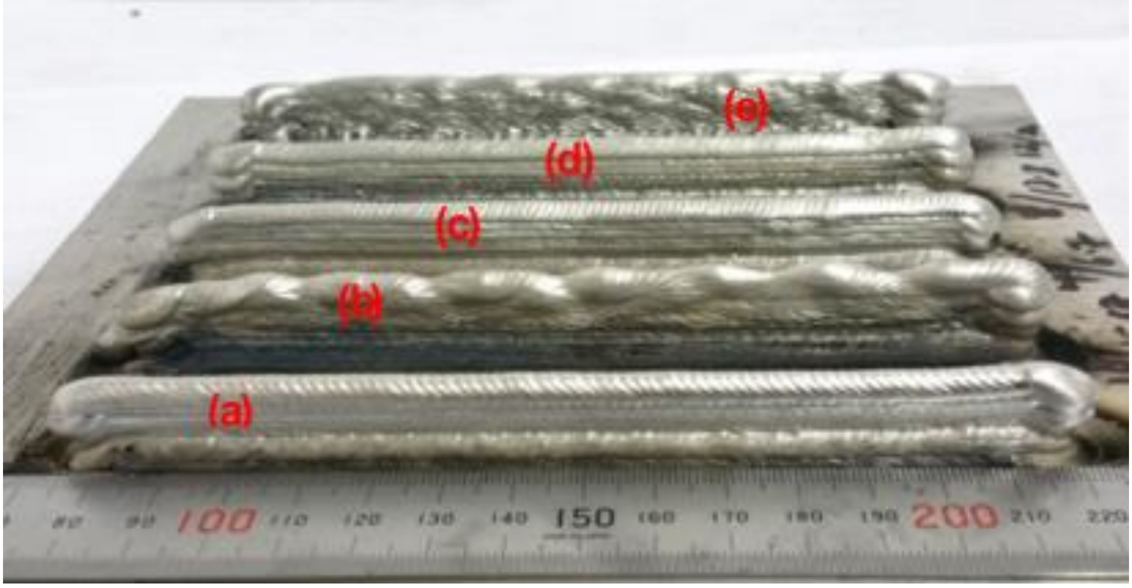

Figure 4-4: Physical features of built walls at constant wire feed speed to travel speed ratio of 10 with input parameters: (a) WFS: 6 m/min, TS: 0.6 m/min; (b) WFS: 10 m/min, TS: 1 m/min; (c) WFS: 4 m/min, TS: 0.4 m/min; (d) WFS: 8 m/min, TS: 0.8 m/min, and (e) WFS: 12 m/min, TS: 1.2 m/min

Based on the physical characteristics of walls as depicted in Figure 4-4 and Figure 4-5, a working envelope was developed for cold metal transfer pulse advance (CMT-PA) wire arc additive manufacturing (WAAM) and this is shown in

Figure 4-6. It can be seen that acceptable walls were obtained with a wire feed speed to travel speed ratio (WFS/TS) ranging between 5 and 25. Furthermore, it can be seen that as the WFS/TS increases the lower limit of the WFS increases.

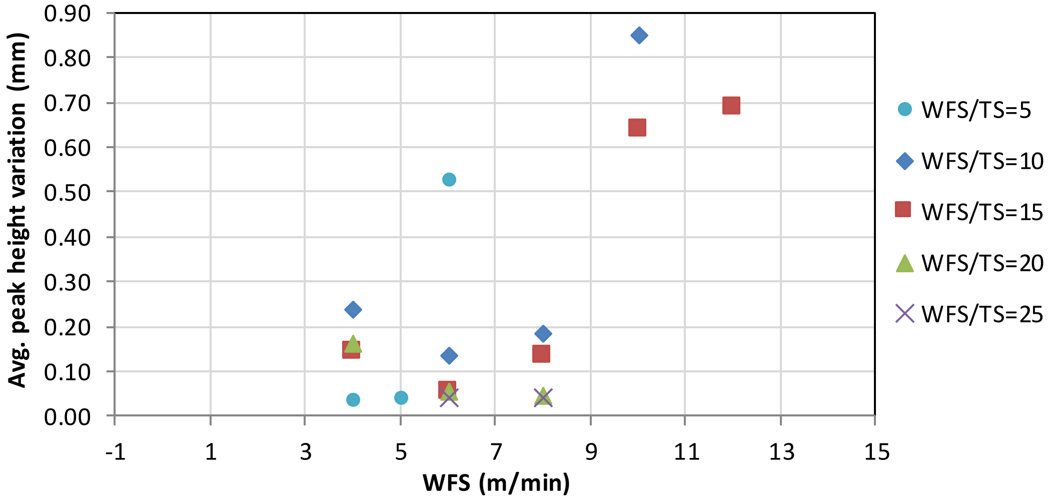

Figure 4-5: Effect of the WFS on the average peak height variation for the respective WFS/TSs: 5, 10, 15, 20 and 25

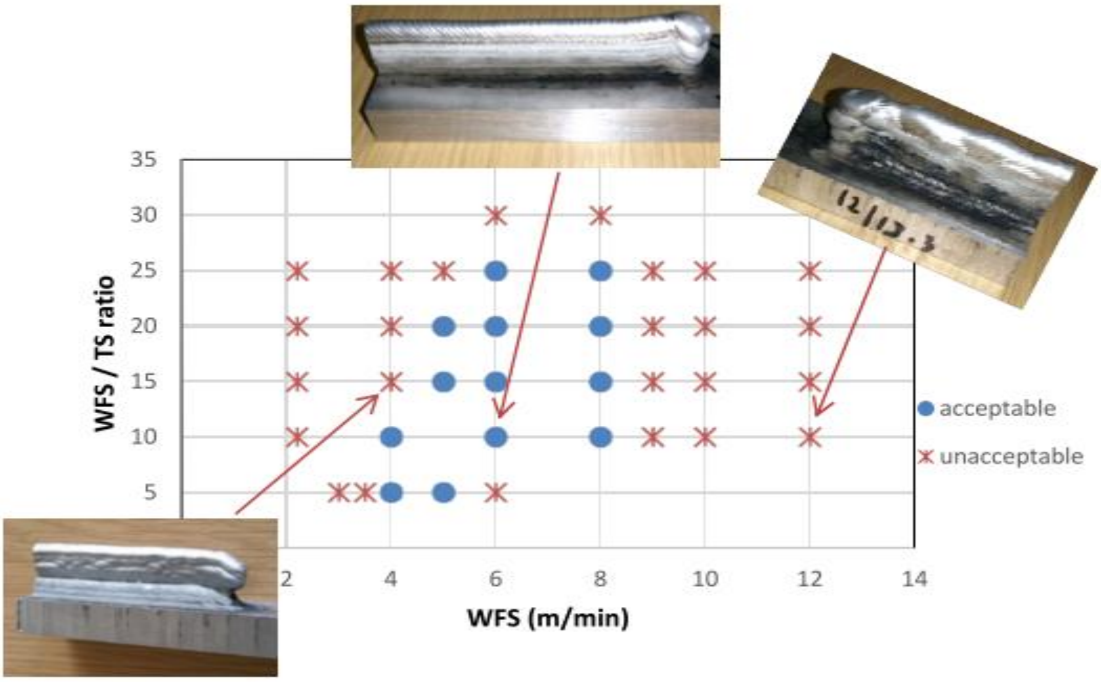

Figure 4-6: CMT-PA Working Envelope for WFS against WFS/TS

Figure 4-7a and Figure 4-7b show the effect of wire feed speed (WFS) on effective wall width (EWW) and total wall width (TWW) for wire feed speed to travel speed ratios (WFS/TSs) of 5, 10, 15, 20 and 25. It was possible to build walls with EWW and TWW ranging between 4.9 mm – 8.0 mm and 5.3 mm - 9.8 mm respectively. It can be seen from the figures that both EWW and TWW increase as WFS/TS increases for all the ratios studied. The results also show that for each ratio, EWW and TWW appear to be approximately constant as WFS increases.

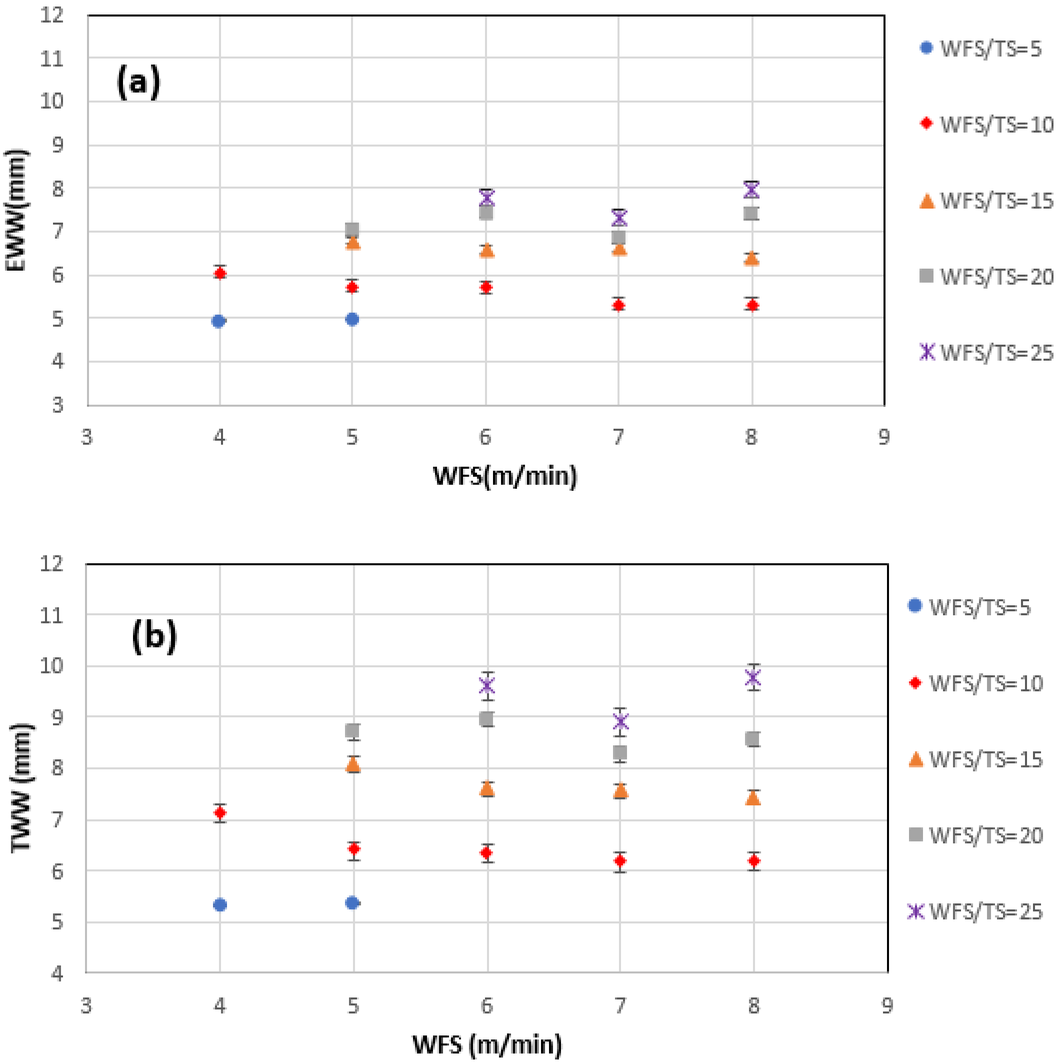

Figure 4-7: The effect of the WFS on the EWW and TWW for the respective WFS/TS ratios: 5, 10, 15, 20 and 25

Figure 4-8 shows the effect of the WFS on the layer height for the fixed WFS/TS ratios. Generally, the layer height (LH) increases as the WFS/TS increases. The results also show that for each ratio, LH appears to be nearly constant or slightly increasing as WFS increases.

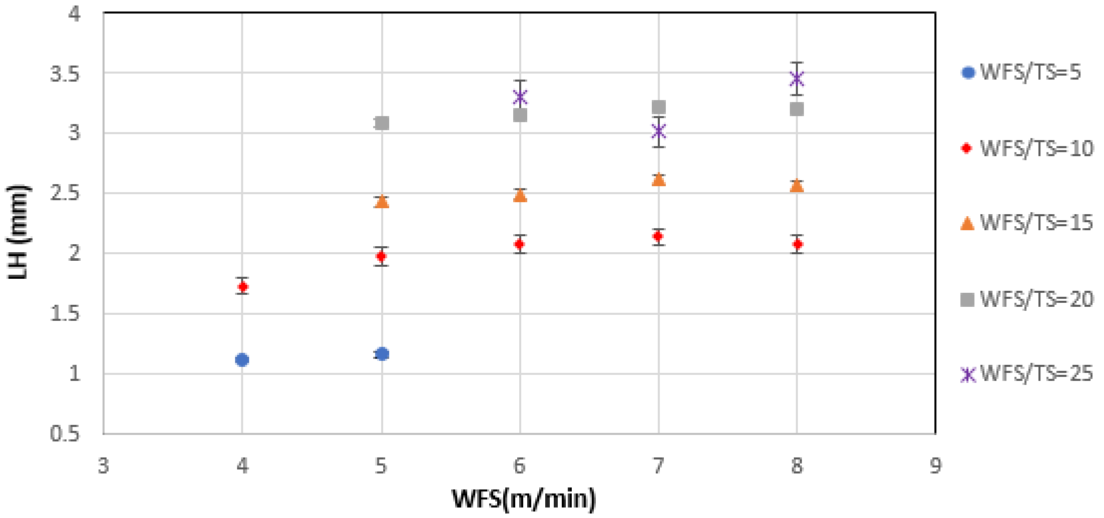

Figure 4-8: The effect of the WFS on the layer height (LH) for the respective WFS/TS ratios: 5, 10, 15, 20 and 25

Figure 4-9 shows the effect of WFS on surface waviness (SW) for the fixed WFS/TS ratios. The results show that SW increases as the WFS/TS increases.

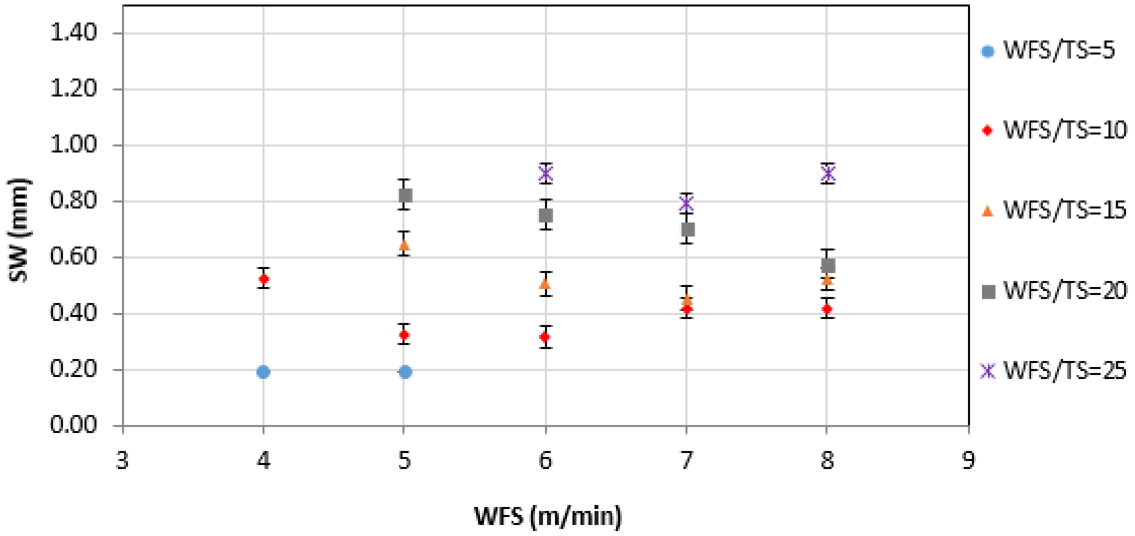

Figure 4-9: The effect of WFS on surface waviness for the respective WFS/TS ratios: 5, 10, 15, 20 and 25

Figure 4-10 compares the LH and SW for the respective WFS/TS ratios. Generally, it can be seen that there is a direct correlation between LH and SW. Therefore increasing the WFS/TS ratio increases both the surface waviness and layer height correspondingly.

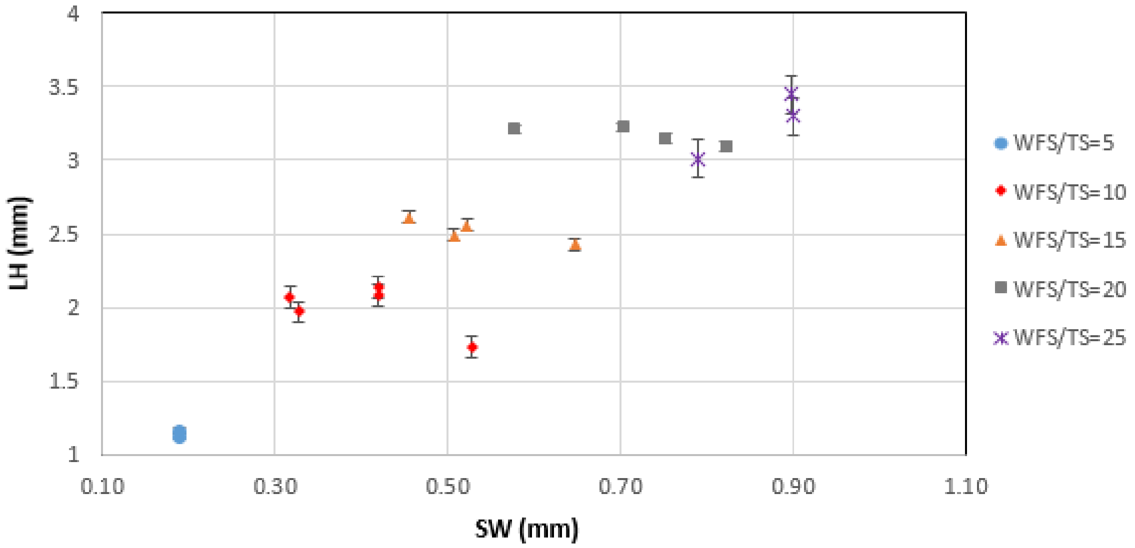

Figure 4-10: A plot of Layer height (LH) against surface waviness (SW) for the respective WFS/TS ratios: 5, 10, 15, 20 and 25

Figure 4-11 shows the effect of WFS on heat input (HI) for fixed WFS/TS ratios. It can be seen that heat input increases as WFS/TS ratio increases. However, heat input decreases linearly as WFS increases for each given ratio.

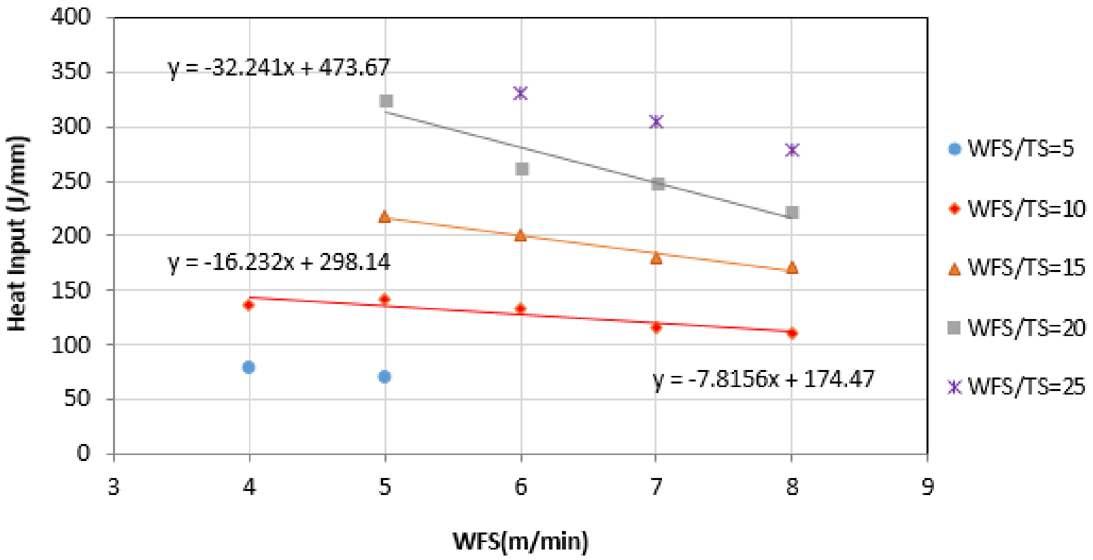

Figure 4-11: The effect of the WFS on heat input (HI) for the respective WFS/TSs

Figure 4-12a shows the microstructures of wall produced with wire feed speed to travel speed (WFS/TS) ratio of 15 for WFS of 6 m/min. It can be seen that the structure is characterised by dendrite grains within layers and equiaxed grains at the interphase of deposited layers. It can also be seen that these grains are separated at the interphase by an interlayer boundary (Figure 4-12b).

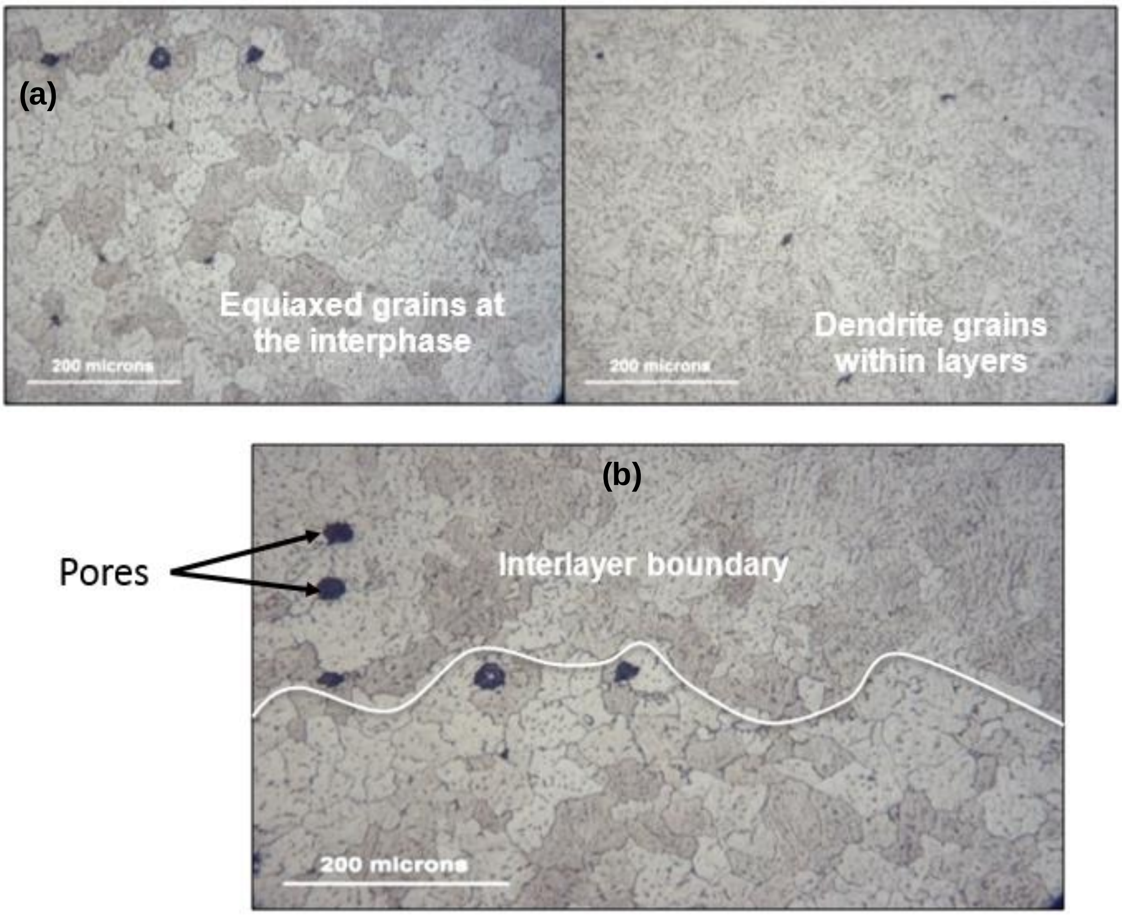

Figure 4-12: (a) Microstructure of wall deposited with WFS/TS = 15, WFS = 6m/min, HI = 177.52 J/mm (b) Grain structure of Aluminium WAAM Walls

Figure 4-13 shows the influence of the wire feed speed to travel speed (WFS/TS) ratio on porosity (for WFS = 6m/min). It can be seen that for pore sizes of 10 - 50 µm, pore counts increase as the WFS/TS ratio increases from 10 to 20 and then decreases at a WFS/TS ratio of 25. However for pore sizes of 50 - 100 µm, pore counts marginally increase as the WFS/TS ratio increases from 10 to 25. It was also observed that for a WFS/TS ratio of 25 pore sizes were found mainly on the top region of the wall.

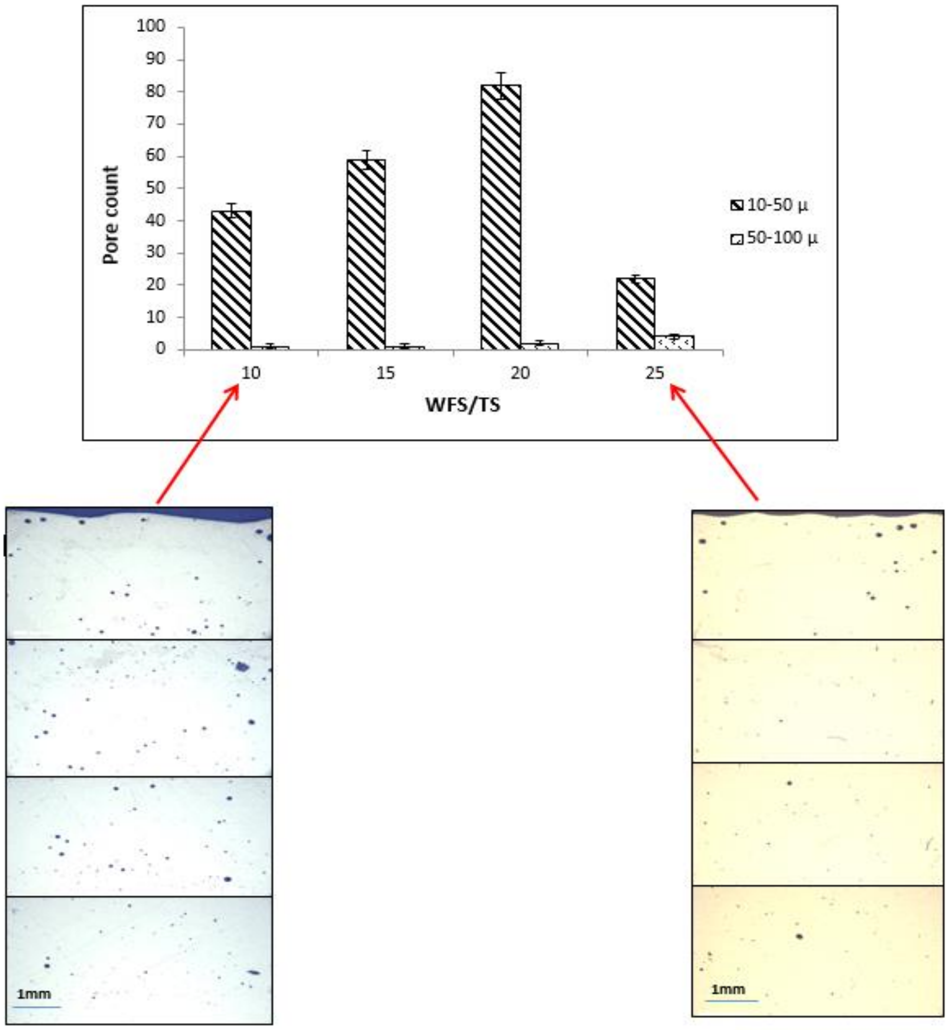

Figure 4-13: The effect of WFS/TS ratio on Porosity (WFS=6 m/min)

4.4 Effect of CMT-PA and CMT-pulse processes on multi-layer bead linear walls

4.4.1 Experimental procedure

In this section, initial studies were carried out into oscillating the torch to assess the effect of CMT-PA process on thicker section walls which exceed the limit of single layer bead width. The experiments were conducted by selecting parameters which have been successfully used in building single bead width (SBW) linear walls in Section 4.3 (as shown in Table 4-2). Oscillation step advancement used in the building strategy were selected based on the quality of the wall. Moreover, the quality of the wall was based on the stability of the process by inspecting the sectioned walls to see if they were free of lack of fusion defects.

Table 4-2: Parameters used during Oscillation in CMT-PA mode

WFS (m/min)	TS (m/min)	SBW (mm)	Ratio	Actual Step advancement (mm)
5	1	5.4	5	3.6
6	0.6	6.4	10	4.2
6	0.4	7.7	15	5.1
6	0.3	9.0	20	5.9

Oscillation step advancement (%) = 66 %

Further investigations were also carried out using the CMT-pulse (CMT-P) process to produce thicker section walls using oscillation and parallel deposition strategies (as shown in Figure 4-1). Table 4-3 shows parameters used for performing the experiments. Subsequent layers were also deposited on top of the initial layers by using the weld bead height as the layer height increment. Deposited walls were sectioned and grouped into four different conditions. These included oscillated and parallel as-deposited walls and oscillated and parallel T6 post-deposited heat treated walls.

For the post-deposition T6 heat treatment, a two stage process was used. This consisted of solution treatment and artificial ageing. Firstly, samples were heated from room temperature to 515 °C at 60 °C/h and then from 515 °C to 535 °C at 20 °C/h. These samples were left at the temperature for 90 min and followed by rapid cooling in cold water. Afterwards, artificial ageing was then conducted at a ramping speed of 60 °C/h from room temperature to 151 °C and then at 20 °C/h from 151 °C to 171 °C for 12 hours. Finally, samples were allowed to cool to room temperature in the furnace.

Table 4-3: Process parameters for oscillated and parallel walls built using CMT-P process

Process strategy	WFS (m/min)	TS (m/min)	Step advancement (%)	SBW (mm)	Layer height (mm)	Actual Step advancement (mm)
Oscillation	5	0.6	66	8.5	2.5	5.6
Parallel	5	0.6	66	8.5	2.5	5.6

Samples were then analysed for microstructure, pore distribution and macro hardness. Porosity anlalysis was conducted 100 mm^2 along the deposited wall. Prior to the analysis, metallographic samples were cold mounted and prepared following the procedures as explained in (section 3.5).

For mechanical testing, three tensile test specimens were sectioned from the walls in both the longitudinal and transverse directions as depicted by Figure 4-14a. The sectioned samples where then machined to finish, Figure 4-14b. Tensile tests were then conducted in both the longitudinal and transverse directions using an Instron - 5500R in accordance to BS EN ISO 6892 –1:2009 standard. The capacity of the load cell and test speed used were 30 KN and 1 mm/min respectively.

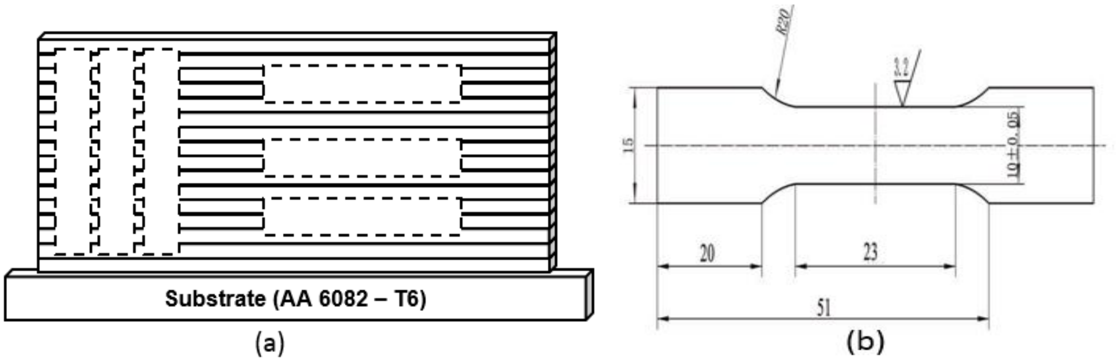

Figure 4-14: (a) The sectioned directions of tensile specimens (b) tensile specimen dimension

4.4.2 Results

The physical features of walls built by oscillating the torch of the CMT-PA process is shown in Figure 4-15. It can be seen that larger widths were possible during oscillation for WFS to TS speed ratios of 10, 15 and 20. In Figure 4-16, the effect of oscillation on wall quality has also been shown. It was observed that walls were characterised by lack of fusion defects in both transverse and longitudinal sections. These defects where present in between layers as depicted in Figure 4-16a and Figure 4-16b.

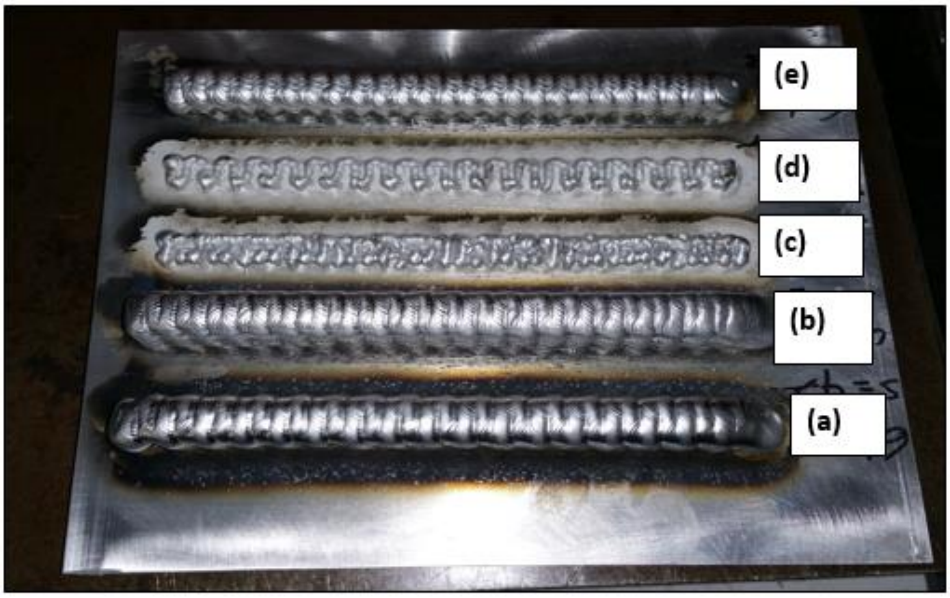

Figure 4-15: Physical features of walls built by oscillating in CMT-PA mode: (a) WFS/TS=10; (b) WFS/TS=15, (c, d) WFS/TS= 5 and (e) WFS/TS=20

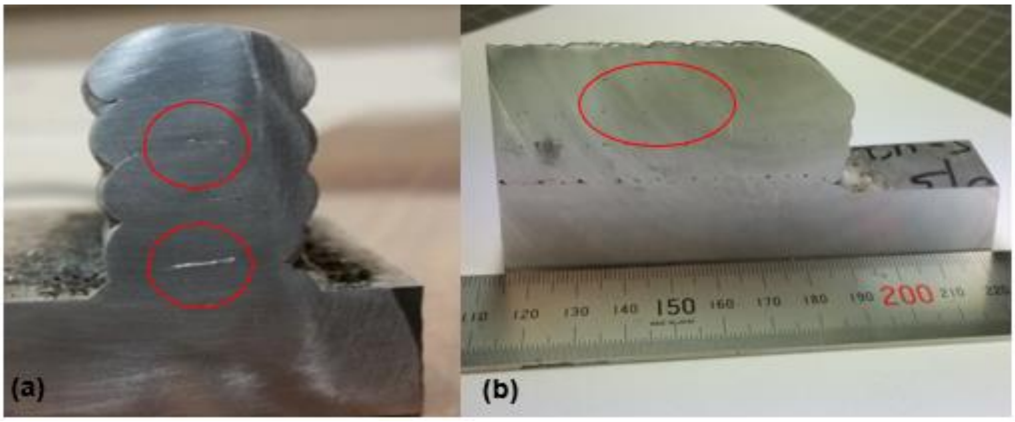

Figure 4-16: Lack of Fusion defects in CMT-PA oscillated wall, WFS/TS = 20: (a) transverse section and (b) longitudinal section

In Figure 4-17, the effect of CMT-P process on thicker section walls have also been shown for both oscillation and parallel deposition strategies. It can be seen that both walls are characterised by smut which is the dark substance covering the surface of the walls.

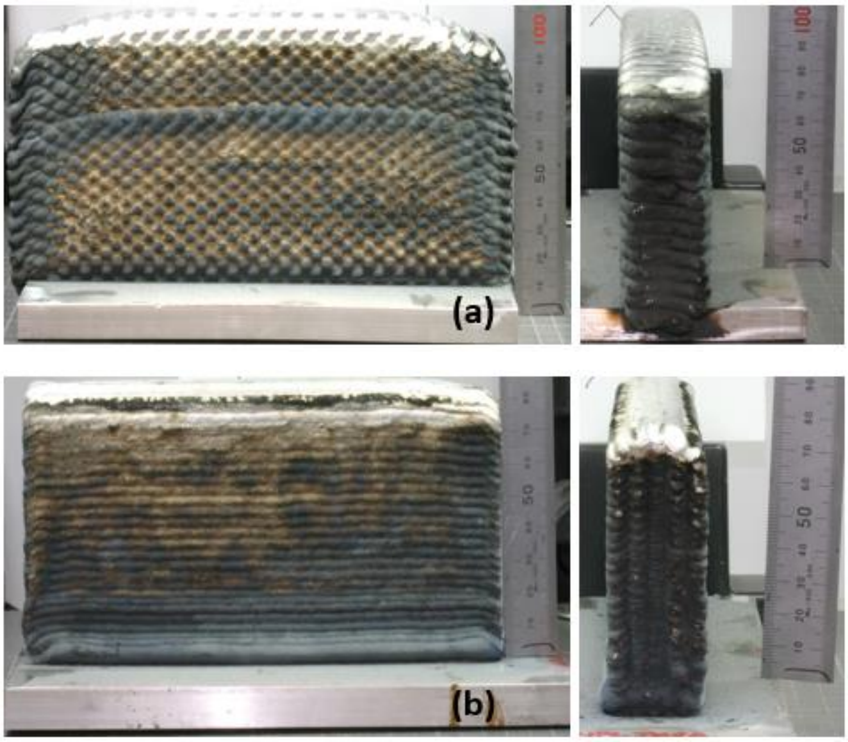

Figure 4-17: Physical quality of aluminium 2319 WAAM walls produced: (a) oscillated deposited wall; (b) parallel deposited wall

Figure 4-18 compares the hardness values of oscillated and parallel walls to that of single bead walls in both longitudinal and transverse directions. From the hardness results, it can be seen that oscillated walls display lower hardness values in comparison to the other deposition strategies. It was observed that parallel walls and single bead walls exhibited similar hardness values. The results also show no significant variation in the hardness measurement for the different sectioned directions (transverse and longitudinal).

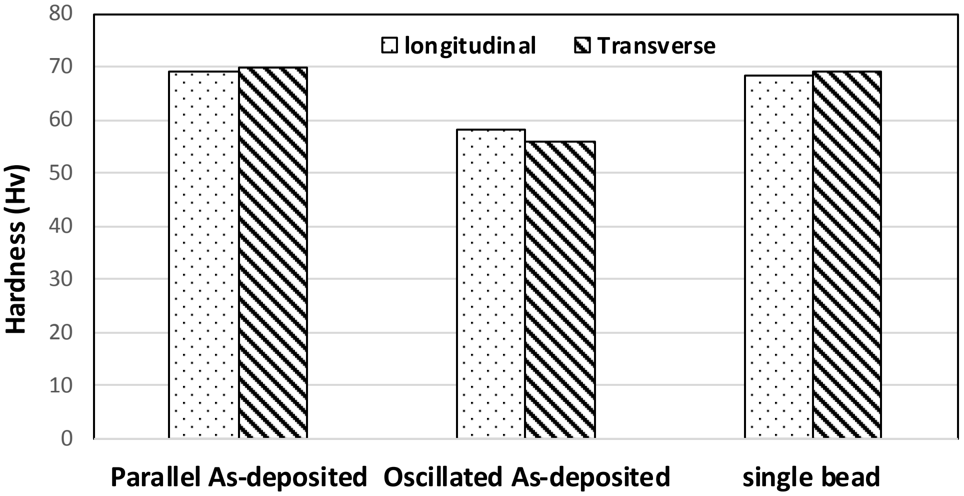

Figure 4-18: Macro hardness measurement of oscillated, parallel and single bead as-deposited walls

The optical micrographs of as-deposited and post-deposited T6 heat treated oscillated and parallel aluminium WAAM walls have been shown in Figure 4-19. In the as-deposited microstructures, oscillated walls showed equiaxed grains (Figure 4-19a) whereas parallel walls showed a two phase structure (Figure 4-19b) comprising of columnar and refined equiaxed grains respectively. After T6 heat treatment, the grain structure of both strategies were refined with oscillated walls characterised by fine equiaxed grain structure and parallel walls consisting of columnar and fine equiaxed grains (Figure 4-19b and d).

From porosity analysis (Figure 4-20), it can also be seen that both strategies are characterised by pores in the 100 mm^2 cross section. The results show less pores in parallel walls but larger ones (Figure 4-20c) as compared to oscillated wall micrograph (Figure 4-20b). It can also be seen that larger pore sizes are mainly at the interface between layers whereas smaller pores are scattered within the deposit.

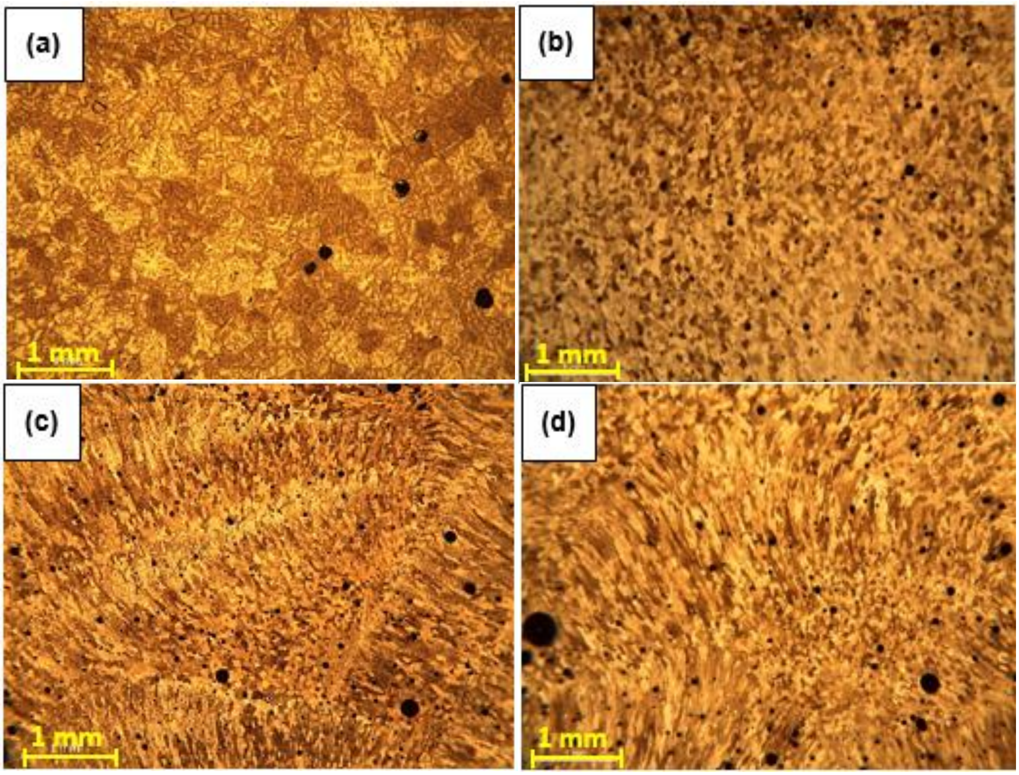

Figure 4-19: Microstructure of aluminium 2319 WAAM walls: (a) as-deposited oscillated; (b) oscillated post-deposition heat treated T6; (c) as-deposited parallel; (d) parallel post-deposition heat treated T6

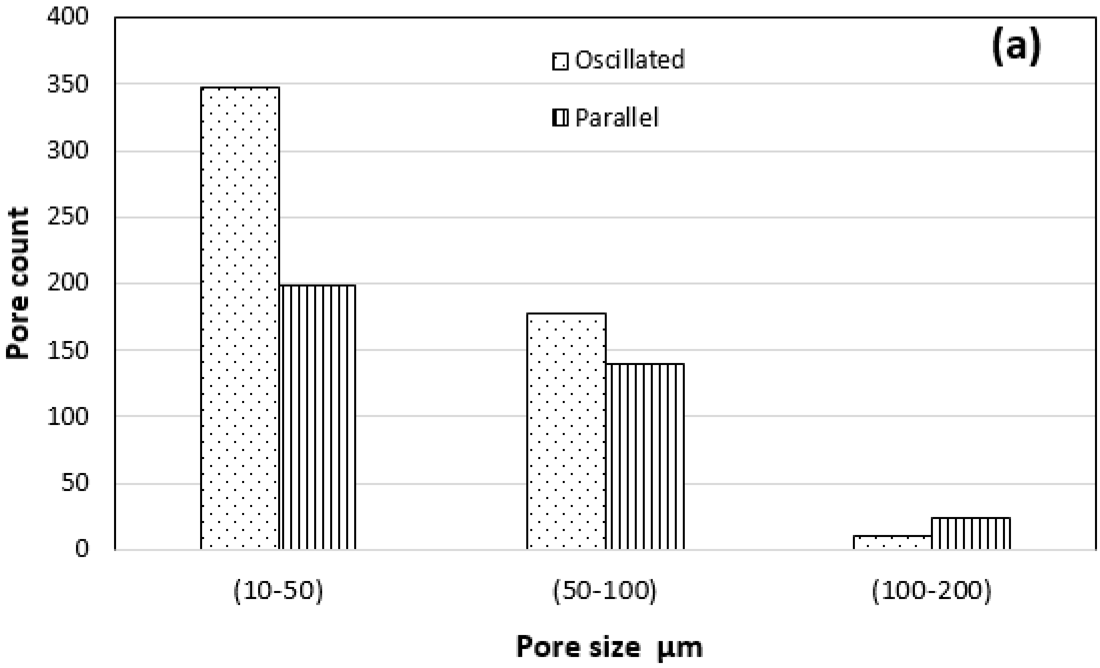

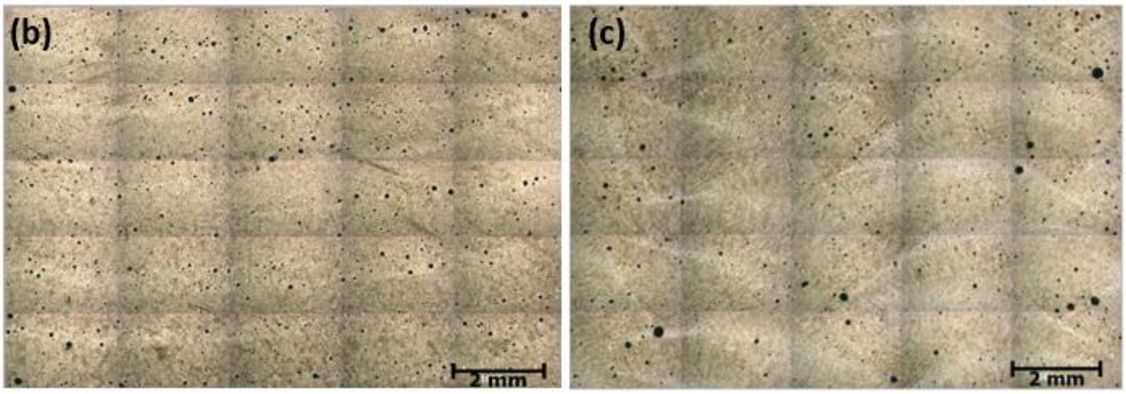

Figure 4-20: (a) Pore distribution in as-deposited walls (Area 100 mm^2); (b) oscillated; (c) parallel walls

Figure 4-21 and Table 4-4 show the effect of oscillation and parallel deposition strategies on the ultimate tensile strength (UTS), yield strength (YS) and elongation (%) of 2319 aluminium WAAM walls of as-deposited and post-deposited T6 heat treated samples. The results show optimum UTS and YS in parallel post-deposited T6 heat treated walls with about 56 % and 86 % increase respectively in comparison to their corresponding as-deposited WAAM walls. It can also be seen that mechanical properties are similar in the different directions of oscillated walls but differ in elongation for parallel walls. It was observed that elongation in parallel walls were dissimilar for the different test directions for both as-deposited and T6 heat treated walls. From the results, maximum elongation was observed in the horizontal direction of parallel as-deposited walls with a minimum in the vertical direction after T6 treatment. In addition, by comparing mechanical test results of thicker section walls to single bead width walls produced by Gu et al. [91], it can be seen that the UTS and YS results were higher in single bead width walls after T6 treatment with no significant differences in the as-deposited condition. The results also show higher elongation values in the single bead width walls as compared to thicker section walls built.

The fracture surface of WAAM tensile test specimens are shown for the vertical direction of walls produced (Figure 4-22). It can be seen that all the tested specimens were characterised by dimples. In Figure 4-22d, the fracture surface is also seen to be characterised by porosity as depicted by the arrow.

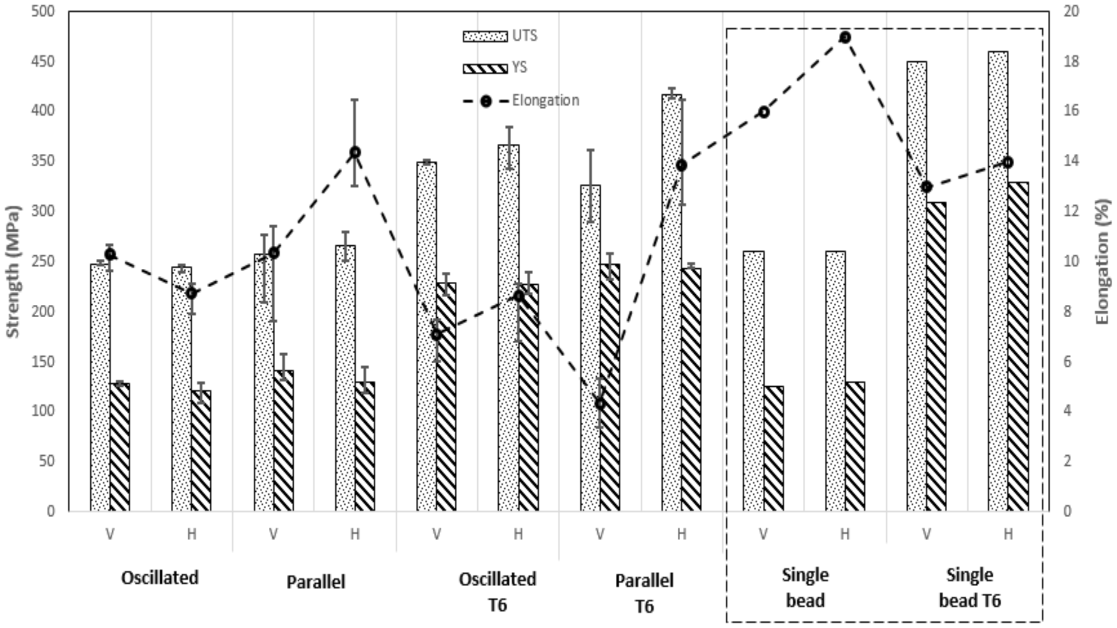

Figure 4-21: Tensile properties for oscillated and parallel 2319 WAAM walls in comparison to single bead width walls produced by Gu et al. [91] **in the as-deposited and heat treated conditions (V and H are the vertical and horizontal test directions)**

Table 4-4: Tensile test values for oscillated and parallel walls

	UTS		YS		Elongation	
Direction	**V**	**H**	**V**	**H**	**V**	**H**
Oscillated	247	245	128	121	10	8
Parallel	257	266	140	130	10	14
Oscillated T6	349	367	228	227	7	8
Parallel T6	326	417	247	243	4	13
Single bead	260	261	125	130	16	19
Single bead T6	452	460	310	330	13	14

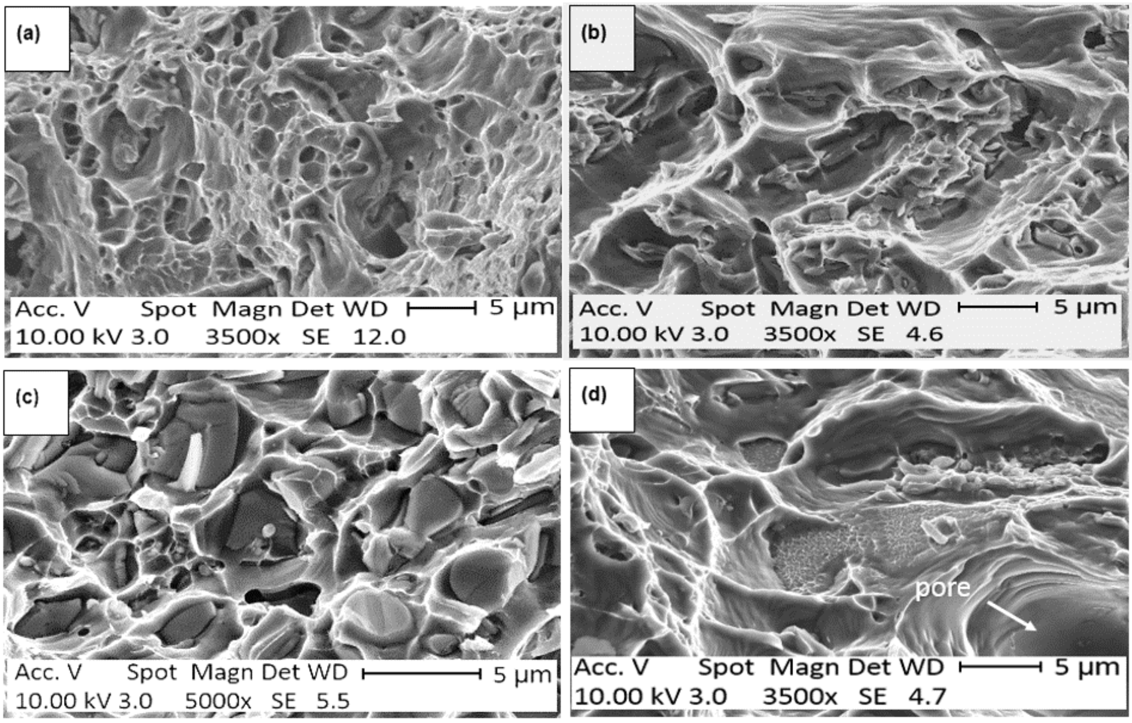

Figure 4-22: Fracture surface of WAAM 2319 tensile test specimens (a) oscillated as-deposited; (b) oscillated post-deposition T6 heat treated; (c) parallel as-deposited; (d) parallel post –deposition T6 heat treated

4.5 Discussion

4.5.1 Effect of CMT-PA on single bead linear walls

For the CMT-PA transfer mode in Al-WAAM, acceptable quality walls could be built with the wire feed speed to travel speed ratio (WFS/TS) ranging between 5 and 25 giving an effective wall width (EWW) of 4.9-8.0 mm. Unacceptable walls were mainly characterised by bead humping leading to non-uniform surface profile as shown in Figures 4-3 and 4-6. Assuming that the heat input profile with WFS continues as shown in Figure 4-11 for low WFS (below 4 m/min), this may explain the unstable deposits at these low WFSs. The higher heat input for the same amount of material deposited could lead to a very fluid and large melt pools not suitable for building on the top of the previous weld bead. For high WFSs above 8 m/min the deposits again become unstable. Pickin et al. [100] previously showed for conventional CMT that for a WFS below 8 m/min the waveform was CMT and the transfer mode was all short circuit. Above 8 m/min the waveform became a mixture of pure CMT and pulsed leading to a two part transfer mode (spray and short circuit). This mixed mode of transfer is likely to have resulted in the non-uniform bead surface profiles for WFSs above 8 m/min.

All geometric dimensions, effective wall width (EWW), total wall width (TWW) and layer height (LH), increase with increasing WFS/TS ratio. This is because more material is deposited per unit length as the WFS/TS ratio increases and because the current increases as the WFS increases. The effects of WFS at a given WFS/TS ratio are small, with any changes likely to be as a result of the reduction in heat input with increasing WFS. It was also found that surface waviness (SW) increased as the WFS/TS increased between 5 and 25 (Figure 4-9). There is a direct correlation between LH and SW as shown in Figure 4-10. Increasing the layer height increased the surface waviness. However, this increase was below 1 mm indicating that less material will be machined during actual production for low WFS/TS thereby decreasing material wastage.

In contrast to work performed by Cong et al. [93], significant porosity was observed in the cold metal transfer pulse advance (CMT-PA) wire + arc additive manufacture (Figure 4-13). It is believed that this was due to variations in the wire quality from batch to batch [116]. For this work, the same wire spool was used throughout and in general the number of pores increased with wire feed speed to travel speed ratio (WFS/TS). As the amount of deposited material per unit length increases with WFS/TS ratio this may have been due to the larger weld bead size limiting the ability of hydrogen bubbles to escape before solidification of molten aluminium [103]. However there was a decrease with a WFS/TS ratio of 25 which may be attributed to the escape of these bubbles due to their high heat input characterised by slow cooling due to the very large mass of hot material. For pore sizes of 50-100 µm these were mainly seen in the top region which could be associated with entrapped gases unable to escape.

4.5.2 Effect of CMT-PA and CMT-pulse on multi-layer bead linear walls

The effect of oscillating the torch in the CMT-PA mode was possible for WFS/TS between 10 and 20 (Figure 4-15). However, macrographs of sectioned walls were characterised by lack of fusion defects which is not suitable for engineering structures. This was eliminated using the CMT-P process. Comparing the geometry of single bead layers produced by CMT-PA and CMT-P processes, it has been found that CMT-PA melt bead geometry is characterised by low contact angle, θ (see Figure 4-23). This is likely to result in the lack of fusion defects observed during multi-layer bead deposition. From the heat input recordings, it was found that the heat input of CMT-PA process is about 25 % lower than CMT-P process which could decrease the melt bead dilution also contributing to the lack of fusion defects.

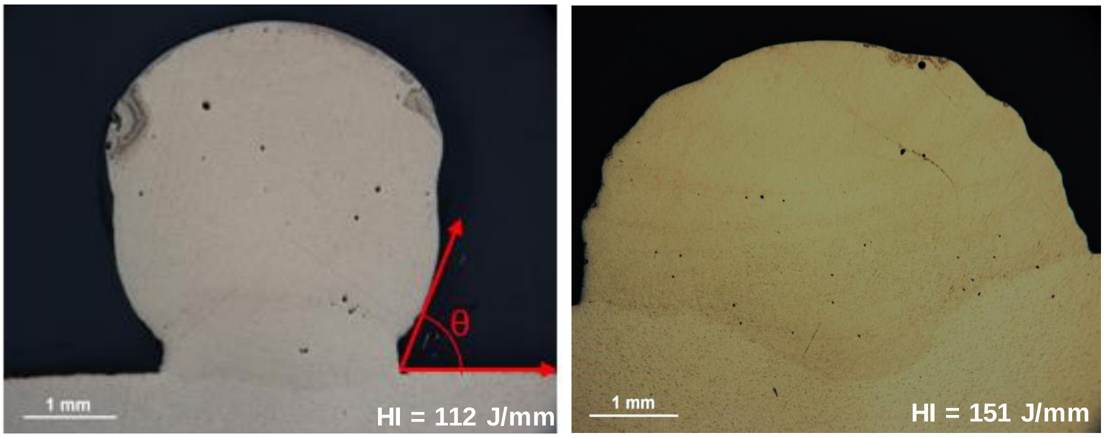

Figure 4-23: CMT-PA (left) and CMT-P (right) single layer bead geometry (WFS: 6 mm, TS: 0.6 m/min)

The CMT-P process was utilised for thicker section wall building using both parallel and oscillation deposition strategies. In this study, it is evident that walls built by CMT-P process are characterised by smut. This was also identified in studies conducted by Pinter [116] on aluminium wire + arc additive manufacture. The author explained that the quality of wire influences the amount of smut formed on the melt bead surface. Therefore the authors highlighted that organic contaminants and lubricant residues could be a source for smut formation. Additionally, the high heat input of the CMT process could increase the temperature of the melt which in turn causes vaporisation of low boiling point alloy elements such as, magnesium and zinc to form smut on the surface of melt bead tracks produced [117]. This problem will apply to all GMAW based processes where the wire forms the electrode and therefore the material is always in the hottest part of the arc.

The hardness results shows that parallel walls were 20% higher than oscillated walls (Figure 4-18). During parallel deposition, the arc is stopped prior to the deposition of the next overlapping bead as compared to the local heat build-up during oscillation as there is no arc stop. In view of this, during parallel deposition, the initial bead cools down prior to deposition of subsequent overlapping beads. Furthermore, the already cooled melt bead could act as a heat sink to the next melt bead deposited. From the literature review conducted (Section 2.1.2), the rapid cooling rate of the melt is likely to increase the amount of copper retained in the matrix and therefore increase the hardness value [104,118]. This can also explain the similar results obtained in the case of single layer bead deposited walls.

From mechanical test results (Figure 4-21), it is evident that the UTS and YS were maximum after T6 post-deposition heat-treatment. This corroborates studies conducted by Gu et al. [91] on the effect of post deposition heat treatment on Al-6.3 Cu single bead deposited linear walls. The authors found that the low strength of as-deposited walls is related to their microstructure. These were characterised by the absence of fine strengthening Al_2Cu precipitates and segregation of the solute along the grain and dendrite boundaries. Aluminium 2319 is a copper (Cu) based alloy and obtains its strength by precipitation hardening which has a dependency on time and temperature. During precipitation hardening, the alloy is heated to a point (between 500 ^{0}C and 580 ^{0}C) where the second phase (Cu) dissolves in Al solution [27] and then rapidly cooled to retain the Cu in the alloy as metastable supersaturated solid solution. The rapid cooling rate results in formation of fine strengthening precipitates which in turn increases the strength of the alloy [91]. Using the oscillation strategy, the cooling rate will be reduced as there is no arc stop and waiting time which will induce coarser strengthening precipitates which will reduce the strength of the alloy. The difference in elongation values for the different test directions of parallel walls can also be correlated with the microstructure. This consisted of a mixed microstructure of columnar and fine equiaxed grains. Columnar grains are elongated in one direction making the properties different in the different test directions. According to Kurz et al. [119], columnar growth results from a unidirectional oriented heat flux during heat transfer from a melt into a cooler solid as observed in the case of parallel walls. Conversely, the isotropy of oscillated walls also is likely to be as a result of the coarse equiaxed grain structure resulting from the low temperature gradient of the process. Furthermore, the difference in mechanical properties of T6 heat treated single bead width [91] and thicker section walls of this study can be ascribed to the different ageing times used. For this study, longer aging resulted in a reduction in the mechanical properties as compared to work performed on single bead width walls. The fracture surface of broken tensile test specimens depicted ductile fracture for all the walls as observed by the dimples on the surface. Furthermore, the results indicate that porosity could also be a contributing factor to failure as can be seen in Figure 4-22.

The porosity analysis conducted in Figure 4-20 showed that parallel walls were characterised by increased pore sizes and number as compared to oscillated walls. From studies conducted by Cong et al. [93] and Gu et al. [80], the narrow finger shaped melt pool characteristics of CMT-P process will likely inhibit the escape of gas pores. Furthermore, the authors also identified a close relationship between porosity and grain size due to the competition between pore nucleation and grain size. This may explain the larger pores identified in parallel walls which are characterised by columnar grains. Moreover, the high cooling rate of parallel walls is likely to result in more trapping gas pores as they try to escape prior to solidification. Furthermore, the high amount of smut on the surface of melt beads could also lead to contamination of the melt pool which in turn increases the amount porosity [116].

4.6 Capability of the CMT process for production of AMCs

In this section, the possibilities of using CMT process for AMCs have been evaluated. From the studies conducted, it has been found that CMT process is suitable for walls but has limitations in independent current control. The inability to control current independently of WFS could limit the working range in terms of controlling the process to produce specific melt bead shapes during production of AMCs. Moreover MIG based processes are also violent with minimum control compared to TIG based processes. The studies also found that porosity is a big factor especially for thicker section walls which could also be detrimental during production of AMCs. Likewise, the process is also characterised by a noticeable amount of smut which results in contaminating the melt pool during deposition. This could result in formation of reaction products which may be detrimental to the produced AMCs.

5 Process studies of tungsten inert gas (TIG) deposition of aluminium wire + arc additive manufacture

This chapter includes data reported in the publication below:

Ayarkwa K. F., Williams S. W., Ding J. (2017). Assessing the effect of TIG alternating current time cycle on aluminium wire + arc additive manufacture. Additive Manufacturing. Elsevier B.V.; 2017; 18: 186–193. ***(Published)***

Context:

This section reports on studies conducted on alternating current TIG (ACTIG) process for aluminium wire + arc additive manufacture. It exploits the independent control of current and WFS to control WAAM process energy and melt bead shape to overcome the limitations of the MIG WAAM process variants identified in Section 4. Initially, the effect of the electrode positive time cycle of the alternating current TIG process was investigated to assess its effect on oxide removal and melt bead geometry. Furthermore, the effect of process parameters on linear wall dimension were also investigated.

5.1 Introduction

In section 4, the capability of the CMT WAAM process was considered with the view to producing aluminium matrix composites. It was found that the process was limited by the inability to vary current independently of the wire feed speed (WFS) making it challenging to achieve some specific bead geometries. Conversely the TIG process can independently control the current and WFS. In the literature review (Section 2), the flexibility of controlling the electrode positive (% EP) and negative (% EN) time cycle, Figure 5-1 has been found to influence removal of oxides and melt fusion respectively during deposition. The mechanism of oxide removal involves the generation of anions from the arc plasma which are directed towards the aluminium base metal [23,120]. The impact energy of the anions results in breaking the bonds between the oxides prior to their removal.

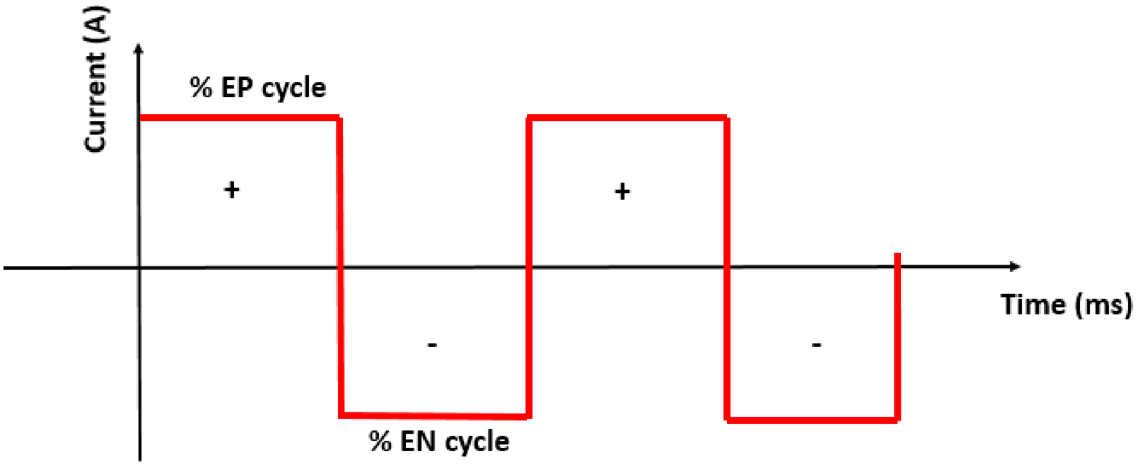

Figure 5-1: Schematic of an alteranting current square wave form depicting % EP and % EN time cycles

ACTIG has been used for aluminium WAAM to show the possibility of producing WAAM parts such as cone and linear wall structures [96,99]. However, the effect of alternating current time cycle on Al WAAM fusion and oxide removal is still unidentified. This study therefore investigated the effect of ACTIG on Al WAAM by assessing the effect of alternating current time cycles on cleaning and linear wall dimensions (wall width and layer height). In addition, the effect on mechanical properties and microstructure was also investigated.

5.2 Experimental set-up

Section 3 gives detailed descriptions of all equipment and material compositions used in this section. The experiments were performed using a Trio 3 axis motion system CNC with a Migatronic TIG commander 330 AC/DC power source. The wire was fed from the front to align with the centre of the electrode by touching the substrate at an angle of 36 degrees. A cooling system placed underneath the substrate was used to cool down the substrate to room temperature between deposits.

5.3 Effect of ACTIG process on single layer bead deposition

5.3.1 Experimental procedure

Prior to linear wall building, single layer beads of aluminium 5556 wire were deposited on a 6082-T6 substrate of dimensions 200 mm x 200 mm x 6 mm. The study was conducted by varying % EP between (5 and 50 %EP) to assess its effect on oxide removal and bead geometry. In addition, the effect on electrode wear was measured after deposition with reference to a spot which was made on the electrode prior to deposition. Table 5-1 shows the parameters used in depositing the layers. Melt bead deposition was carried out in a pure inert argon environment at a flow rate of 15 L/min.

Table 5-1: Parameters used for ACTIG single layer deposition

Parameters	Current (A)	WFS (m/min)	TS (m/min)
Set	192	1.6	0.15

For each experiment, two single layer beads (160 mm long) were deposited. Subsequently, two sections were cut from each layer around the centre where the weld beads were stable and the average geometric dimensions were measured for each.

5.3.2 Results

Figure 5-2(a) and (b) show the effect of % EP on the width of oxide removal. The results indicate insufficient cleaning effect for 5 %EP, as observed by the dark spots on the deposited layer. It can also be seen that the width of cleaning (white band), Figure 5-2a increases as % EP increases between 10 % and 50 % (Figure 5-1b).

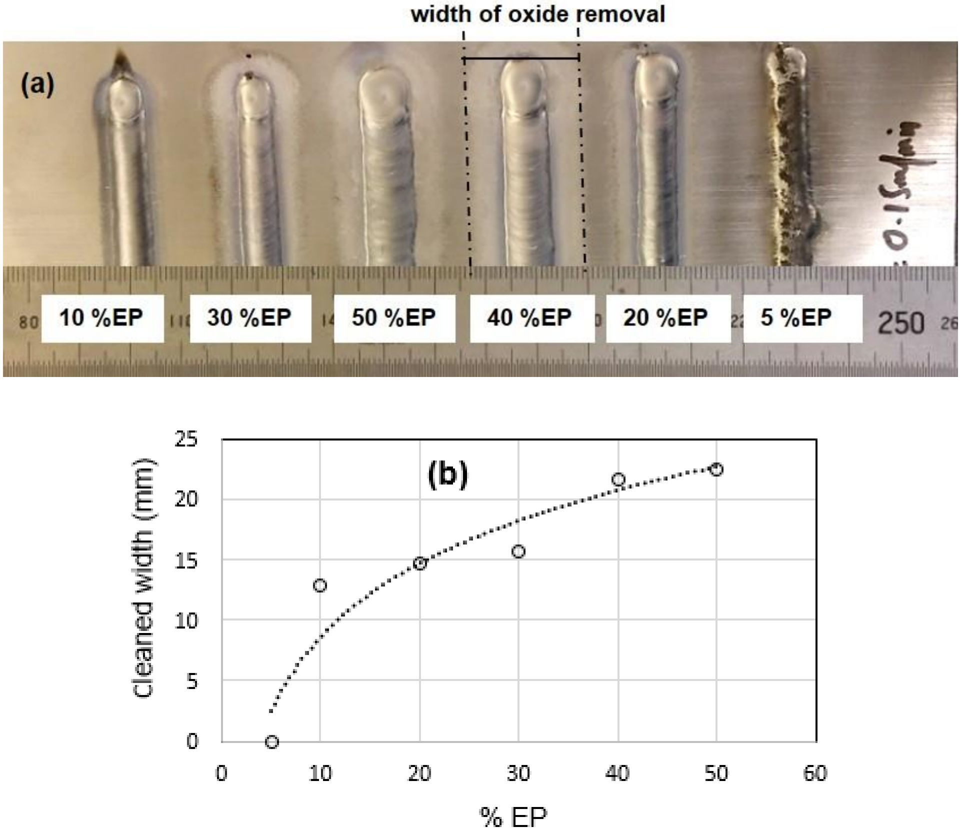

Figure 5-2: Effect of % EP on cleaning width: (a) Weld seam nature; (b) Cleaning trend

Figure 5-3(a) and (b) show the effect of % EP on electrode wear after the first deposited layer. It was observed that increasing % EP increases the wear of the electrode and this becomes significant for % EP > 30.

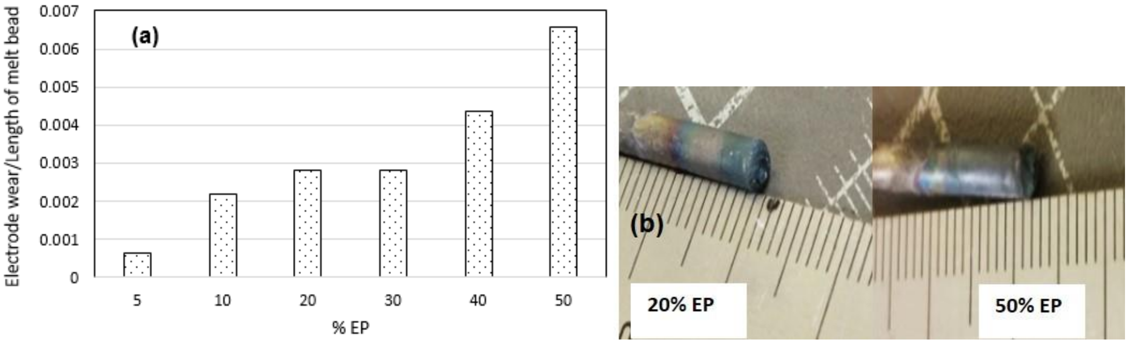

Figure 5-3: The effect of % EP on electrode wear per length melt bead

Figure 5-4 show the macrostructures of aluminium 5556 single layer beads deposited. It can be seen that the geometry of each melt bead differ for the different % EPs used. It can also be seen that melt beads produced were characterised by porosity which is the white spots seen in the melt geometries.

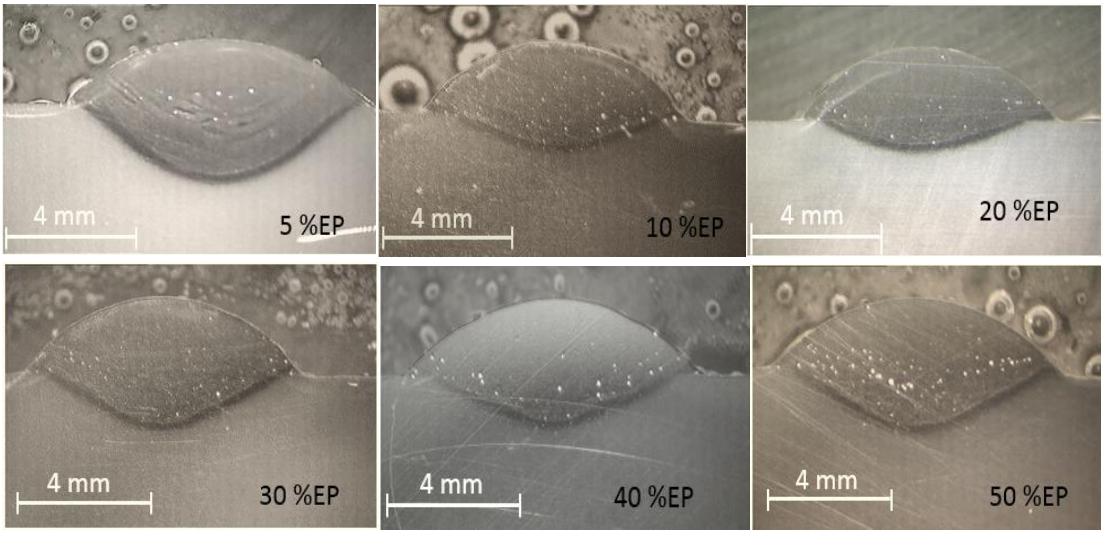

Figure 5-4: Macrostructure of single bead deposition

Figure 5-5 shows the effect of % EP on weld bead geometry. The results generally show that bead width, penetration and contact angle increases as the % EP increases with a minimum at 20 %EP. It can also be seen that the layer height decreases as % EP increases with a maximum at 20 %EP.

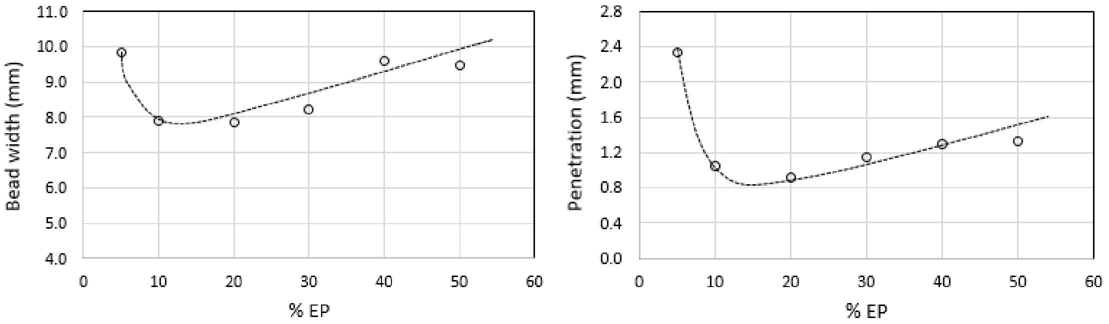

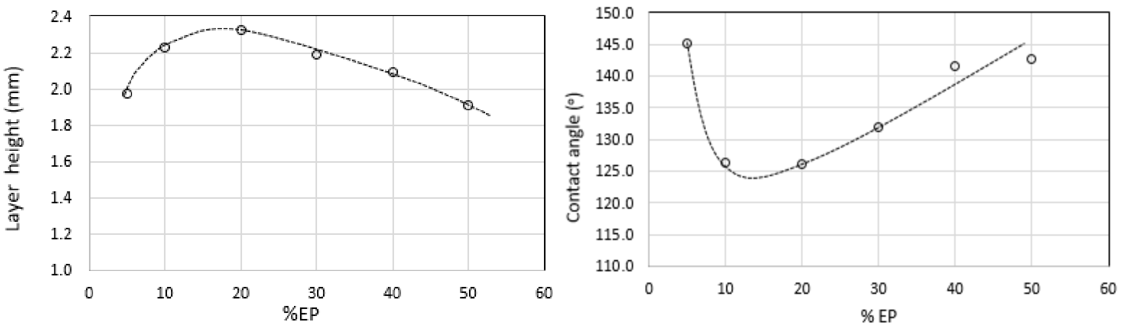

Figure 5-5: Effect of % EP on single layer bead geometry

5.4 Effect of ACTIG on linear wall dimensions

5.4.1 Experimental procedures

The effect of TIG alternating current time cycle on wire + arc additive manufacture was conducted by building walls of twenty layers on a substrate of dimensions 160 mm x 10 mm x 20 mm. These walls had a length of 140 mm and were built in one direction (+x) as illustrated in Figure 5-6. The subsequent layer height increments used were the average layer heights of previously deposited layers and were allowed to cool to room temperature prior to deposition of the subsequent layer. A cooling system (set to 20 ^{o}C) was used to reduce the waiting time after each deposition. The deposition wire feed speed (WFS) was set to 1.6 m/min throughout the experiment. To account for the cooling of the substrate for the first four layers, the welding current (I) was varied at a constant travel speed of 0.15 m/min as shown in Table 5-2. Subsequent layers were deposited with TS of 0.3 m/min and current of 110 A at a constant frequency of 50 Hz whiles the % EP time cycle was varied at 10 %EP, 20 %EP, 30 %EP, 40 %EP and 50 %EP. Further experiments were also conducted by varying the frequency at a constant % EP of 50 %EP. An AMV4000 equipment was employed to measure the current and voltage. The average heat input (HI) was then calculated using Equation 5-1.

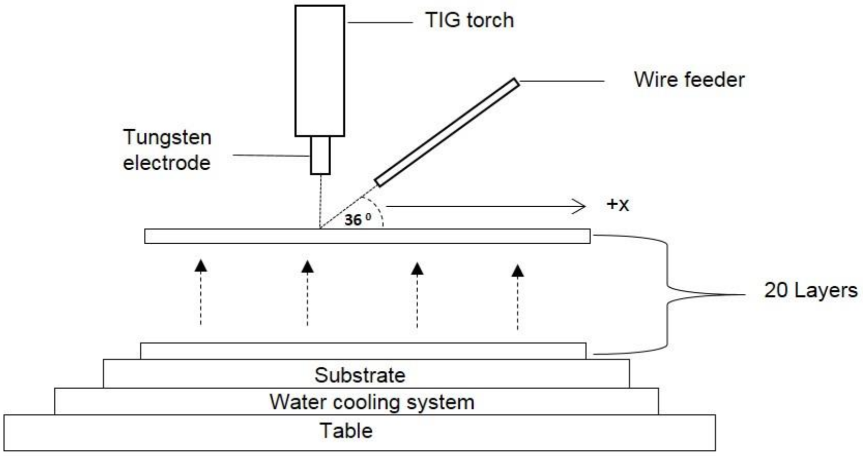

Figure 5-6: Schematic illustration of TIG WAAM of a 20 - layer wall built on substrate, subsequent layers in the same direction (+x)

$HI = n\,(I \times V) / v$ **Equation 5-1**

(current (I), voltage (V), travel speed (v), efficiency (n = 0.6 [121])

Table 5-2: Input process parameters

Layer Number	Actual I (A)	TS (m/min)
1	192	0.15
2	174	0.15
3	156	0.15
4	138	0.15
5-20	110	0.30

Linear walls built were sectioned and their bead dimensions were measured using an optical microscope. Electron backscattered diffraction (EBSD) was also conducted to observe the microstructure. Pore counting was conducted along the middle section (approximately 100 mm^2) using the optical microscope and the IMAGE J software.

Hardness measurements were conducted using a micro hardness indenter by applying a load of 200 g at 10 different points across the test specimens. An average hardness value was calculated in each test. Tensile tests were also conducted in the longitudinal direction using an Instron - 5500R (load cell capacity = 30 KN, test speed = 1 mm/min) at room temperature on 20 % and 50 % EP walls built. For this test, 33 layer walls were built on a substrate of dimension 500 mm x150 mm x 12.7 mm and three test specimens were taken in the longitudinal direction from each wall of which the average values were calculated. During wall building, a constant % EP of 30 % was used in the first four layers (Table 5-2) to account for the cooling of the substrate.

5.4.2 Results

Figure 5-7 shows aluminium wire arc additively manufactured linear walls by variable polarity ACTIG process. This shows the physical characteristics of walls built and the parameters used. It can be seen that the cleaning effect was reduced below 20 %EP as shown by 10 %EP wall built which was slightly darkened in comparison to the other linear walls.

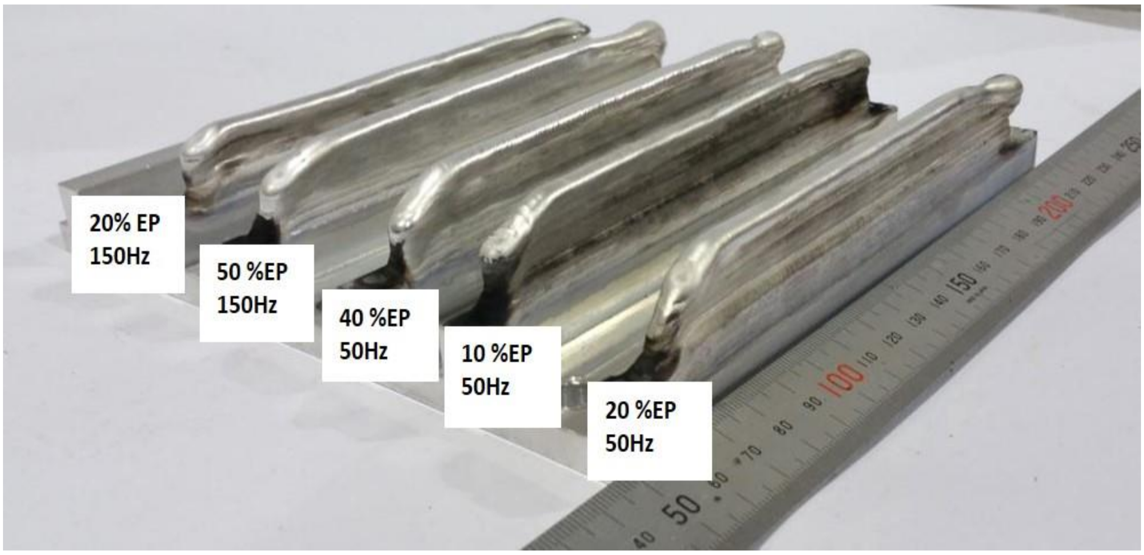

Figure 5-7: Physical characteristics of WAAM walls built by ACTIG

Figures 5-8 (a), (b) and (c) show the effect of % EP on the effective wall width (EWW), layer height (LH) and surface waviness (SW) of the linear walls built. It can be seen that the effective wall width is minimum at 20 %EP with a corresponding maximum in layer height. It can also be seen that surface waviness appears to be approximately constant between 10 %EP and 40 %EP with a maximum at 50 %EP.

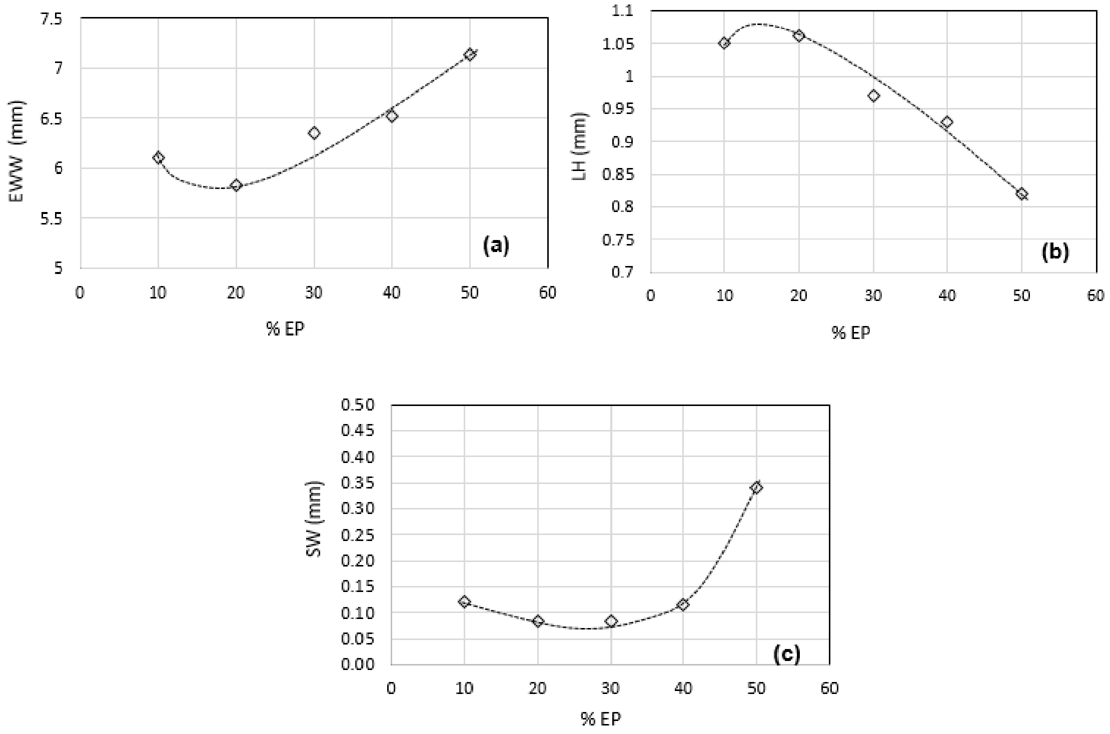

Figure 5-8: The effect of % EP time cycle on (a) effective wall width (EWW), (b) layer height (LH) and (c) surface waviness (SW) of aluminium 5556

Figure 5-9a shows the effect of frequency at 50 %EP on EWW and LH for walls built. The results show that increasing the frequency has no significant effect on linear wall dimensions.

Figure 5-9b also shows the effect of % EP and frequency on the average calculated hardness for AA 5556 WAAM. The results also show no significant effect of % EP and frequency on the hardness for the WAAM walls produced.

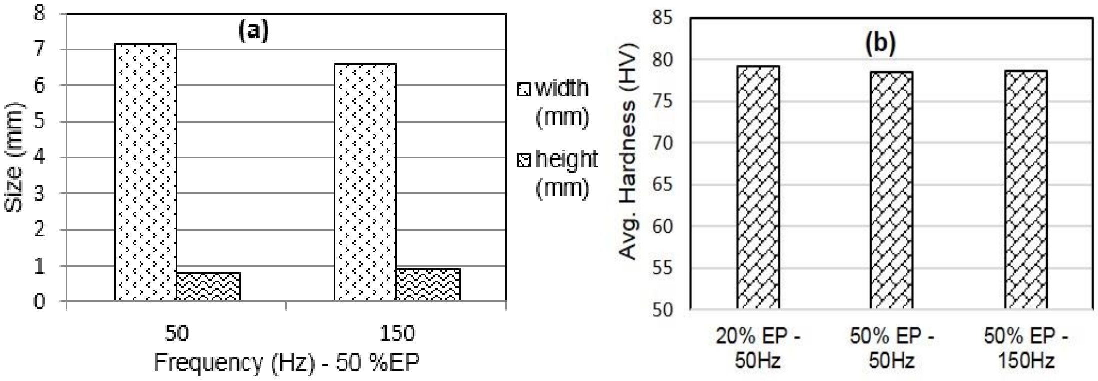

Figure 5-9: The effect of ACTIG Frequency on (a) wall dimensions and (b) hardness

Figure 5-10(a) and (b) show the effect of % EP on voltage and heat input for the wire arc additive manufactured walls. It can be seen that the voltage and therefore the heat input are minimum at 20 %EP.

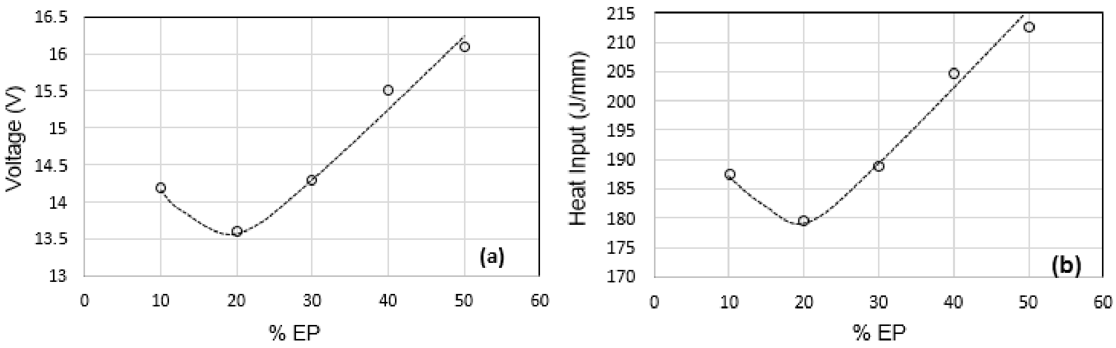

Figure 5-10: Effect of % EP on (a) voltage and (b) heat input for linear walls built

Figure 5-11 shows the effect of 20 % and 50 % EP on microstructure of walls built for a given area. It can be seen that for the same area the grain sizes were coarser in 50 %EP than 20 %EP.

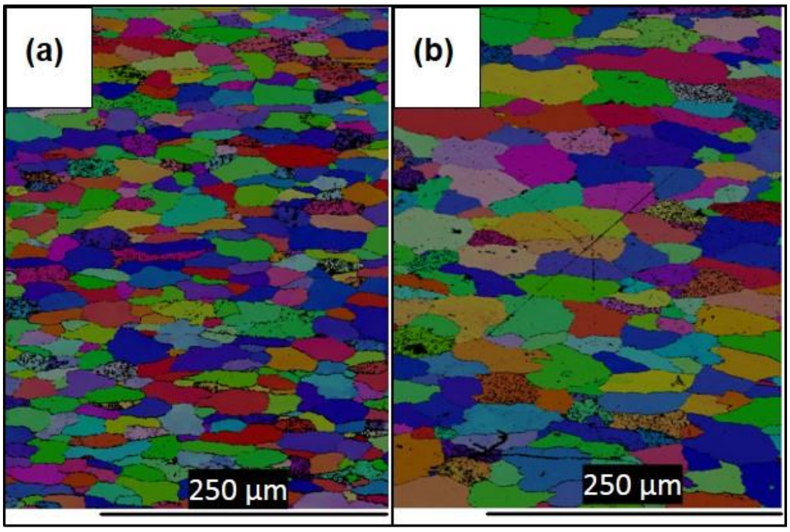

Figure 5-11: Microstructure of (a) 20 %EP and (b) 50 %EP linear walls built (*Image is artificially coloured)*

Figure 5-12 shows the effect of % EP on porosity for 20 % EP and 50 %EP. It can be seen that for pore sizes ranging between 10 – 100 microns, pore sizes and number slightly increased in higher % EP (50 %EP) than lower % EP (20 %EP). It can also be seen that pores are in lines all through the microsection. The results also show that pore sizes and number increases in the initial layers closer to the substrate.

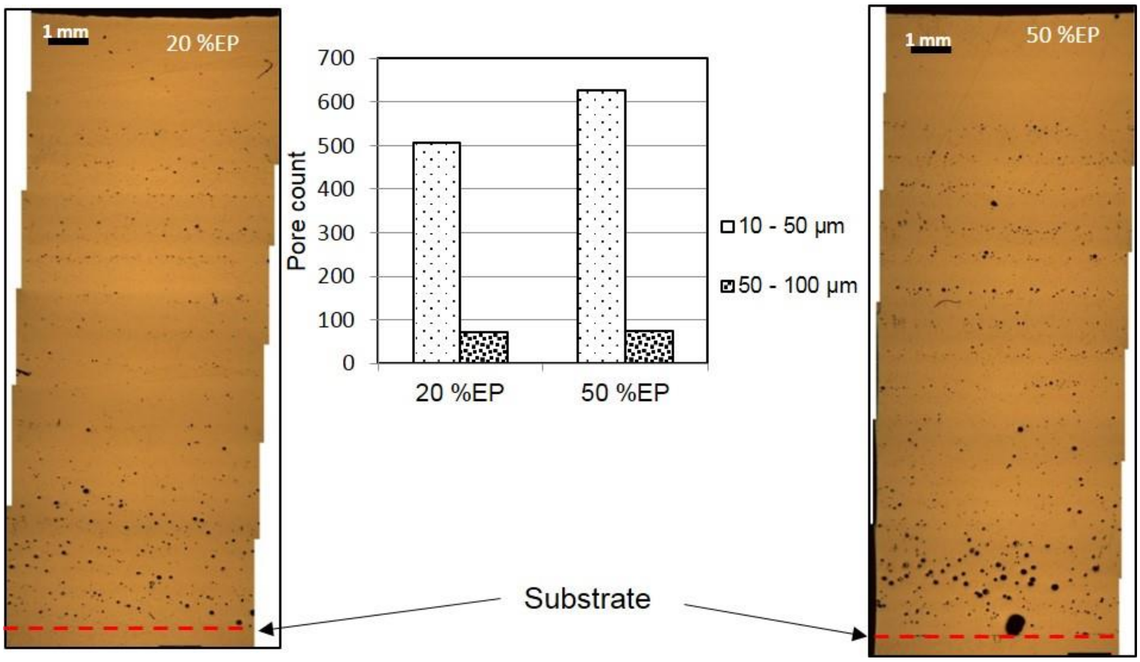

Figure 5-12: Effect of % EP on porosity: 20 % EP (left); 50 %EP (right)

Figure 5-13 shows the effect of % EP on the ultimate tensile strength (UTS), 0.2 % proof strength (0.2 %PS) and elongation (%) of 20 %EP and 50 %EP walls produced. The results show no significant effect of % EP on the mechanical properties.

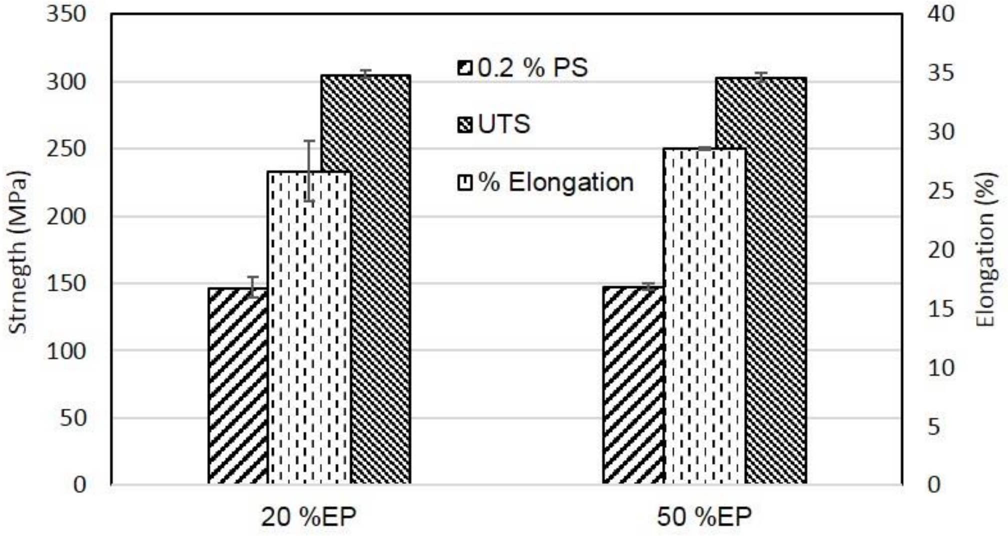

Figure 5-13: The effect of %EP on tensile test results

Figure 5-14 shows the fracture surface of linear walls produced by 20 %EP and 50 %EP. It can be seen that both fractured walls are mostly characterised by dimples

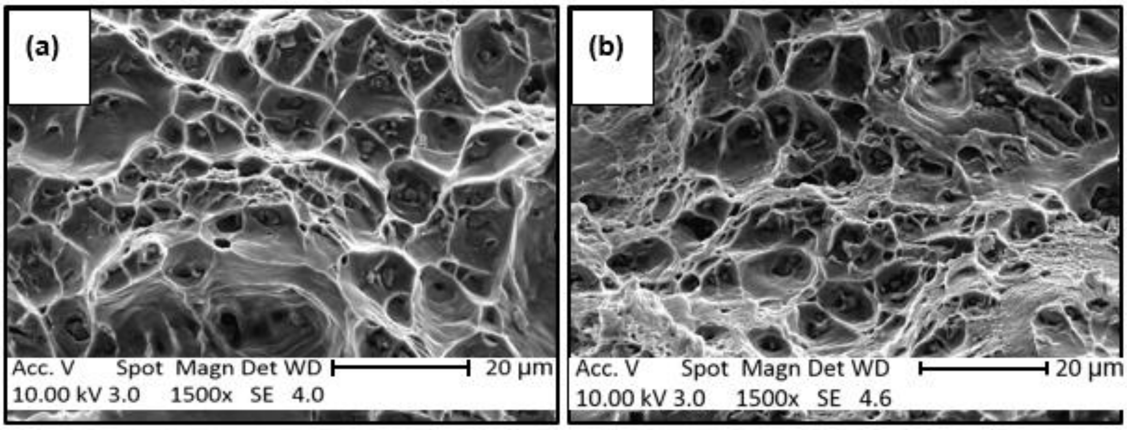

Figure 5-14: Fracture surface of (a) 20 %EP and (b) 50 %EP

5.5 Process envelope development for aluminium ACTIG wire + arc additive manufacture

5.5.1 Experimental procedure

In this section, studies were conducted on AA 2319 aluminium ACTIG WAAM with the view to developing a working envelope prior to powder feeding (ceramic reinforcement). This assesses the effect of process parameters on wall dimension (EWW, and LH) and microstructure. To establish the working envelope, 8 layer walls were built on a 6082-T6 substrate of dimensions (200 mm x 200 mm x 12 mm). These walls were 170 mm long with subsequent layer deposition in one direction. Table 5-3 shows the parameters used in the experiment.

Table 5-3: Experimental parameters for working envelope

Run	WFS/TS	I (A)	TS (m/min)
1	6	200	0.4
2	6	240	0.4
3	12	200	0.2
4	12	210	0.2
5	12	220	0.2
6	12	230	0.2
7	12	240	0.2
8	20	200	0.12
9	20	240	0.12

WFS = 2.4 m/min % EP = 20 %

5.5.2 Results

Figure 5-15 shows the effect of the current on the effective wall width (EWW) and layer height (LH) for WFS/TS ratios 6, 12 and 20. Generally, it was observed that both the EWW and LH increases as the WFS/TS ratio increases. The results also show that the EWW increases with increasing current for the respective WFS/TS ratios. The results also show that the LH decreases as the current increases in the respective WFS/TS ratios.

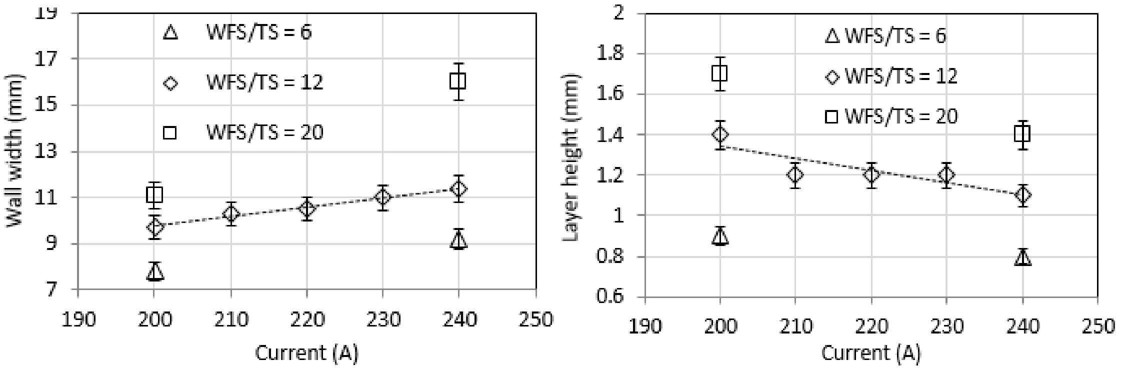

Figure 5-15: The effect of current on the wall width and layer height for the respective WFS/TS ratios: 6, 12 and 24

5.6 Discussion

5.6.1 Effect of ACTIG process on aluminium WAAM

The effect of TIG alternating current time cycle on aluminium wire + arc additive manufacture has been investigated for aluminium 5556. It was possible to build linear walls by varying % EP time cycle between 10 % and 50 % obtaining effective wall width (EWW) and layer height (LH) of 5.8 mm to 7.1 mm and 0.8 mm to 1.1 mm respectively. The limiting factor for lower % EP was based on insufficient oxide removal and an unstable weld bead profile (Figure 5-2), which confirms previous studies by Cirino and Dutra [97] and Yarmuch and Patchett [98]. In this study, it was found that minimum cleaning ranged between 10 % and 20 %EP. For higher % EP above 30 %, the stability of the arc was affected by the corresponding electrode wear (Figure 5-3) due to the heating of the electrode. This was apparent since increasing the % EP increased the wear of the electrode tip correspondingly. From initial studies conducted by Cho et al. [122], it is believed that the melting of the electrode tip affects the absorption of electrons on its surface which in turn makes the arc unstable.

In view of this, by reducing the current by 20 % (Figure 5-16), it was possible to deposit stable welds for higher % EP. This is because of the reduced electrode heating thereby minimising the electrode wear and making the arc stable.

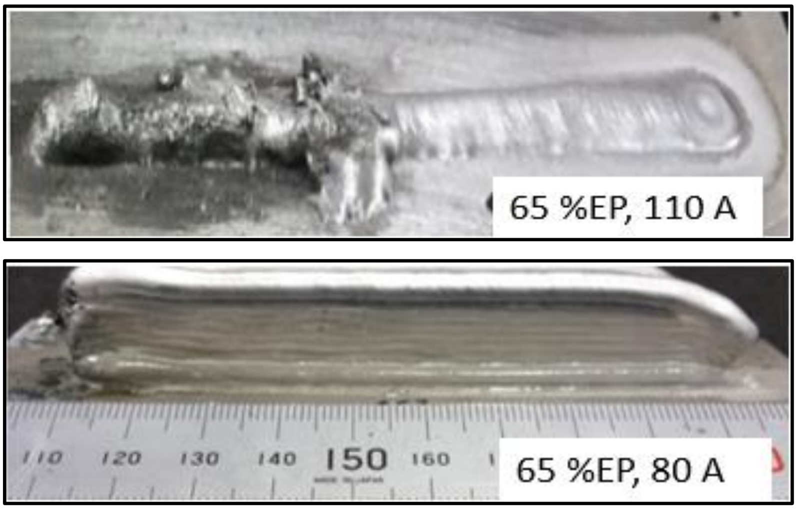

Figure 5-16: Effect of current on higher % EP deposition

From Figure 5-8 (a) and (b), it appears that the EWW has a minimum at 20 %EP with corresponding maximum in LH. It has been shown previously in WAAM that as the heat input increases, the EWW increases and the LH decreases so the effect of % EP on wall geometry can be explained by the change in heat input [90]. A similar trend has also been identified in single layer bead tracks produced (Figure 5-5).

Previous studies on the effect of positive polarity time on ACTIG welding of aluminium indicates that above 20 %EP, electrons are emitted mainly by field emission whereas below this threshold thermionic emission is the main driver of electrons which could explain the fall and rise in the voltage below and above 20 %EP [97,123]. The authors also explained that in the % EP cycle, the oxide is removed when the arc concentrates on the cathode spot of the thin oxide film. After the oxide is removed, the spot rapidly moves to a new spot and the process repeats itself. Moreover, higher % EP generates more cathode spots with longer arc concentration time which also leads to higher heat input and the resulting increase in fusion area [98]. From this study, surface waviness has also been shown to be approximately constant in the linear walls produced with % EP ranging between 10 %EP and 40 %EP (Figure 5-8c). It was found that the surface waviness was about 0.1 mm indicating the minimum machining requirement during actual production. Conversely, the slightly higher surface waviness in 50 %EP could be attributed to the arc instabilities resulting from the increased electrode wear rate. This could cause disturbances in the melt pool during deposition. According to Syed et al. [124], when the melt pool is disturbed, it is likely to show increased surface waviness and vice versa. Furthermore, the study has also shown that for a given % EP, frequency does not have any significant effect on WAAM wall dimensions (Figure 5-9a).

A further experimental technique of adjusting the heat input of 20 %EP to produce similar melt bead geometry to that of 50 %EP was conducted by adjusting either the arc length (distance from the tip of electrode to the substrate) to change the voltage or by adjusting the current from the power source. From this study, it is apparent that the controlling factor for melt bead geometry is the heat input as illustrated in Table 5-4. Therefore increasing the heat input in 20 %EP increased the bead width with a corresponding decrease in layer height.

Table 5-4: Effect of balancing the heat input of 20 %EP to that of 50 %EP, (WFS = 1.6 m/min, TS = 0.15 m/min)

Trial	% EP	Current (I)	Voltage (V)	Arc Length (mm)	HI (J/mm)	EWW (mm)	LH (mm)
A	20 %EP	208	13.5	5	674	7.2	2.0
B	50 %EP	208	16.4	5	819	11.1	1.4
C	20 %EP	208	15.2	7	759	9.5	1.5
D	20 %EP	250	13.9	5	834	11.4	1.3

In addition, it is also noteworthy that the wear of electrodes resulting from the increase in % EP could potentially affect the arc length; thus the voltage and the resultant heat input.

From microstructural analysis (Figure 5-11), it was found that increasing % EP to 50 % led to an increase in the grain size with a resultant decrease in number as compared to 20 %EP. The increase in grain size may have been due to the corresponding increase in heat input (Figure 5-10b). This is expected since increasing the heat input slows down the cooling rate thereby allowing grains more time to grow [93,125]. For porosity analysis (Figure 5-12), 50 %EP had a significant amount of pores in comparison to that of 20 %EP. Porosity in aluminium based alloys is dependent on the amount of hydrogen dissolved in the liquid phase and results from the large solubility difference between the liquid and solid phases [92]. Previous studies by Cong et al. [93] on the effect of cold metal transfer process on porosity of additively manufactured walls identified a close relationship between grain size and porosity. The authors found that fine grains reduced the tendency for pore formation due to the competition between heterogeneous nucleation of grains and pore nucleation sites prior to solidification. This could explain the low porosity found in 20 % EP which had finer grain structure as compared to 50 % EP. In addition, the increase in pore numbers and sizes in the initial layers can also be attributed to the slightly high cooling rate of the substrate. This may result in entrapping hydrogen bubbles as they try to escape before solidification of the melt.

From mechanical test results (Figure 5-13), no significant differences were seen in 20 %EP and 50 %EP linear walls built. This indicates that for the same set of parameters, the difference in % EP does not affect the mechanical properties. Al-5556, a magnesium based alloy, obtains its strength by solid solution strengthening and varies in mechanical properties when there is a change in the chemical composition [23]. During welding, magnesium easily evaporates at high temperature due to their low melting point and vapour pressure in comparison to aluminium [125]. From the study conducted, it can be inferred that the difference in heat input of 20 % EP and 50 %EP may not be critical to affect the chemical composition of the walls deposited. SEM images of the fracture surface of 20 %EP and 50 %EP have been shown in Figure 5-14. The fracture surface of both walls were mainly characterised by dimples. This indicates that both walls exhibited ductile fracture features [91].

5.6.2 Process envelope development

A working range has been developed for Al WAAM for the respective WFS/TS ratios 6, 12 and 20 attaining EWW between (7.8 mm and 16 mm). This flexibility of controlling the current allows the possibility of investigating a wider working range. For a range of currents between 200 A and 240 A, it was found that increasing the current increased the wall width and decreased the layer height (Figures 5-15). This will be expected since the increase in current increases the heat input. The extra heat melts more the substrate leading to a wider melt pool. Furthermore, increasing the WFS/TS ratio increases the amount of material deposited per unit length. A comparable trend was observed in CMT-PA process studies conducted in Section 4. This could explain the resulting increase in both the wall width and layer height.

6 Production of aluminium silicon carbide (Al-SiC) composite by wire + arc additive manufacture (WAAM)

This chapter includes data presented in the Formnext conference on the next generation of manufacturing processes, Germany, November 2017. Production of Aluminium SiC by wire + arc additive manufacture.

Context:

In this section, an alternative manufacturing option for aluminium particle reinforced composites have been investigated using ACTIG wire + arc additive manufacture. The process was studied because of the wider working range and the flexibility of controlling the process parameters as highlighted in Section 5. The study sought to inject SiC particles into an aluminium melt pool with the view to producing aluminium SiC composites. Due to the novelty of this technique, in-depth process development was conducted. The main objective was to find how to control the depth of penetration of the SiC particles and the reinforcement ratio. The effect of feeding angle, nozzle position, particle size and type of shielding gas were investigated to this effect.

6.1 Introduction

The Literature section identified that structurally graded materials and metallic composites provide improved properties which is desirable to the aerospace and automotive industries. The presented work aims to produce aluminium silicon carbide composites using WAAM. This has been conducted to overcome the limitations of commercially produced AlSiC by liquid fabrication techniques identified in Sections 1 and 2.

They include:

- Wetting difficulties between particles and matrix
- Adverse chemical reactions between reinforcement and matrix due to the longer processing times
- Difficulty to control process parameters to produce near net shaped parts which can be repeated.

From the literature review (Section 2), it was identified that shorter duration processing techniques can help minimise formation of detrimental reaction products common with longer duration processing techniques such as casting. According to Lloyd [34], reinforcing aluminium - magnesium based melts with SiC can also help to minimise the formation of aluminium carbide phases. Also, studies conducted by Vreeling et al. [59] using laser melt injection technique revealed the possibility of injecting SiC into aluminium melt. However, the high reflectivity of the laser beam by the aluminium led to a small operating envelope. In WAAM there is flexibility in controlling the melt bead shape by controlling process parameters which means the potential for a broader range of process parameters. To produce Al-SiC by WAAM, the following process requirement have been considered for inserting SiC reinforcement particles in aluminium matrix:

- Use of high heat input processes to increase the melt temperature and eliminate surface oxides.
- Effective control on deposition process parameters to control melt pool size and behaviour

- Effective control on particle injection process parameters such as particle velocity and feed rate.
- Magnesium based aluminium alloy (Al 5xxx).

From previous studies conducted in Section 4 and 5, the ACTIG process was identified as the best WAAM production method for Al-SiC composites. This is due to the much higher level of control of process parameters resulting from the independent control of current (I) and wire feed speed (WFS) to control melt pool size compared to GMAW processes.

Therefore, the study sought to investigate the suitability of the ACTIG process for the manufacture of Al-SiC composites. In addition, the controlling parameters for the injection process were also investigated.

6.2 Experimental set-up

All detailed descriptions of equipment and materials used in this section can be found in Section 3. To produce aluminium matrix composites by WAAM, a Sulzer Metco TWIN-10-C R2 powder feeder was used during the powder injection process. The WAAM process used consisted of an ABB robot and a 330 AC/DC Migatronic TIG commander (see Figure 3-8). The torch nozzle and tungsten electrode diameters used were 10 mm and 3.2 mm respectively and this was set to have an arc length 5 mm perpendicular to the plate. The shielding gases used in the study were argon (15 L/min) and helium (30 L/min). The material substrate and wire used were aluminium 6082-T6 and 5556 respectively. For the reinforcement, SiC particles were used and were conveyed by argon carrier gas from the powder feeder to the melt. Figure 6-1 and Table 6-1 depicts the schematics and orientation of the wire and particle feeder nozzles with respect to the electrode reference and substrate.

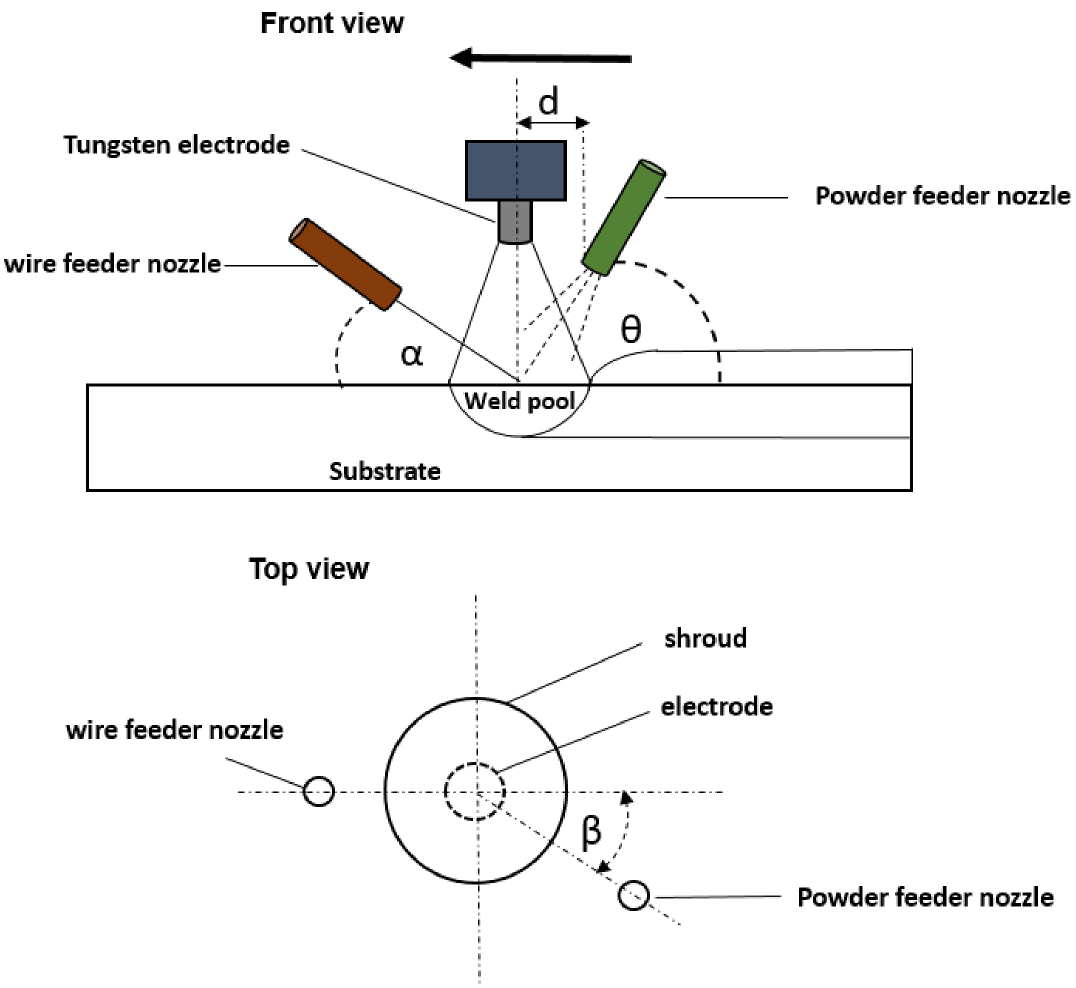

Figure 6-1: Schematic of the front and top views of equipment setup: where (α) and (θ) are the angles of the wire and powder feed nozzle respectively; (d) separation distance between the electrode and powder feeder nozzle; and (β) direction of feeding powder with reference to electrode axis

Table 6-1: Set-up configuration of the process

Trial	Name	α	θ	β	d (mm)
a	Back feed (B)	36	50	0	8
b	Front feed (F)	36	50	160	5
c	Side feed (S)	36	50	40	8

6.3 Process development

6.3.1 Experimental procedures

To produce Al-SiC composite by ACTIG wire + arc additive manufacture (WAAM), initial process development was conducted on the position and direction of injecting particle reinforcement into the matrix. In this study, the wire was always fed at the front of the melt pool on a substrate which had dimensions of 200 mm x 200 mm x 12.7 mm. The reinforcement particles used had an average size of 75 µm (see Figure 3-1a). The study aimed to inject the SiC reinforcement particles into Al melt pool prior to solidification. Table 6-2 shows the constant parameters used in the process investigation. The process stability and melt pool behaviour were monitored using a Redman welding camera and the velocity of particles was measured using a high speed camera (Phantom VR 0608). The study also investigated the required particle velocity on the powder embedding efficiency. To assess the particle embedding efficiency, single bead melt tracks were produced and sectioned. The melt bead geometry and SiC particle distribution was measured using optical and laser scanning microscopes. Prior to the analysis, sectioned samples were mounted, ground and polished following similar procedures for aluminium alloys, see Section 3. Image J software was used to analyse the number of SiC particles captured in the melt.

Table 6-2: Constant parameters used in the experiment

Parameter	I (A)	WFS (m/min)	TS (m/min)	% EP	PFR (g/min)	GFR (ml/s)	Powder Nozzle diameter (mm)
Set	260	2.4	0.10	20	18	2.5	2.3

** Powder feed rate (PFR) and set carrier gas flow rate (GFR)*

6.3.2 Results

Figure 6-2 shows selected images from the process monitoring camera and shows the effect of the orientation of the powder feeder nozzle on the stability of the melt bead and the process. It was observed that the process was stable when the powder nozzle was pointed directly at the back (Figure 6-2a) and side (Figure 6-2c) of the melt seam following the deposition direction. In the case of particles injected at the front of the melt (Figure 6-2b), the flow of the melt pool was interrupted during the injection process resulting in an unstable melt bead and deflection of particles as shown by the arrows.

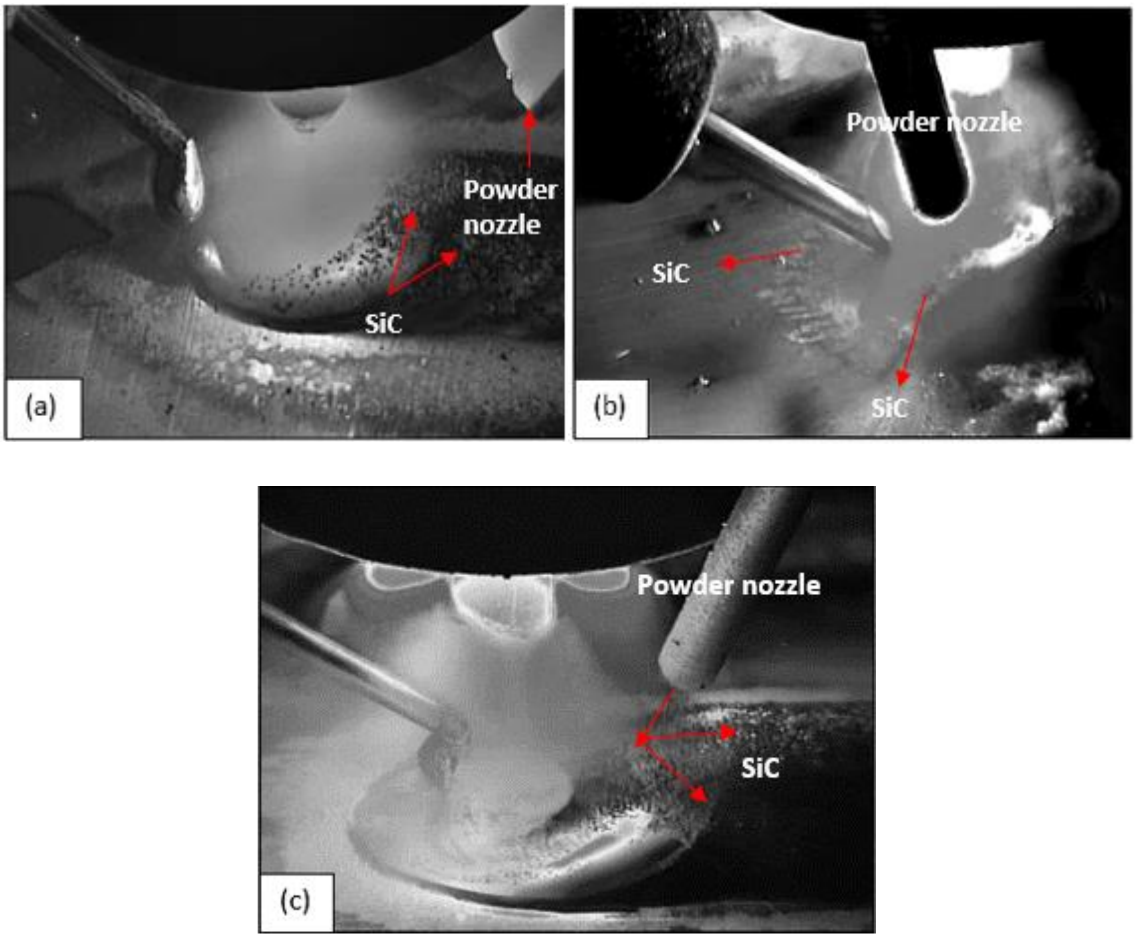

Figure 6-2: Process development for Al-SiC composite production by WAAM: (a) back feeding (b) front feeding and (c) side feeding

The physical characteristics of melt bead tracks produced is shown in Figure 6-3 for back fed and side fed particles. It can be seen that back fed particles were more central at the top of the melt bead (Figure 6.3a) whiles side fed particles were located more towards the side of the melt bead as seen in Figure 6-3b.

Figure 6-3: Melt seam tracks produced by injecting particles at different positions (a) back and (b) side of melt pool

In Figure 6-4, macrographs of back and side fed reinforcement particles are shown. It can be seen that melt beads of back fed particles resulted in a much more stable geometry whereas that of particles injected from the side of the melt resulted in bead drifting towards one side of the melt bead. This is likely to be attributed to the cooling effect of the carrier gas affecting the melt flow.

From the microstructure analysis as can be seen in Figure 6-5, none of the reinforcement particles penetrated the melt beads. The SiC particles are mostly embedded at the top of melt beads produced. The micrographs also display many pores distributed across the entire melt bead produced.

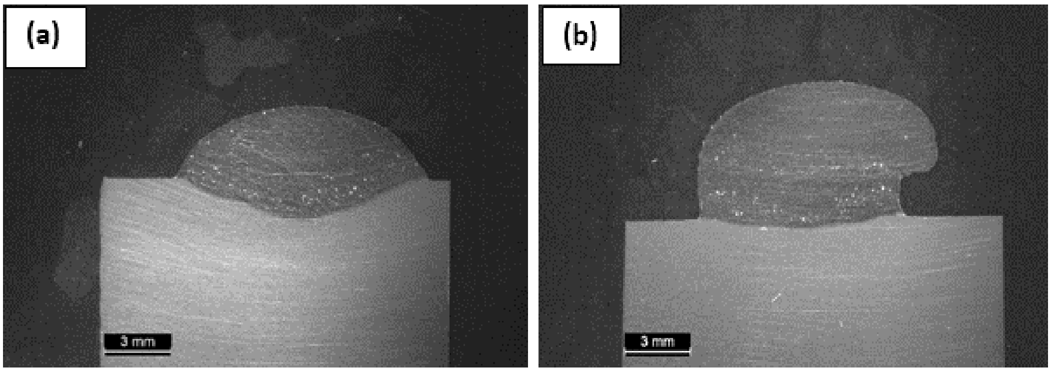

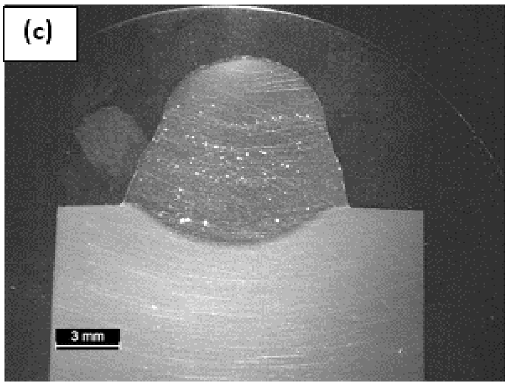

Figure 6-4: Macrographs of beads from initial process development (a) back feeding; (b) side feeding particles; (c) 3 – layer wall

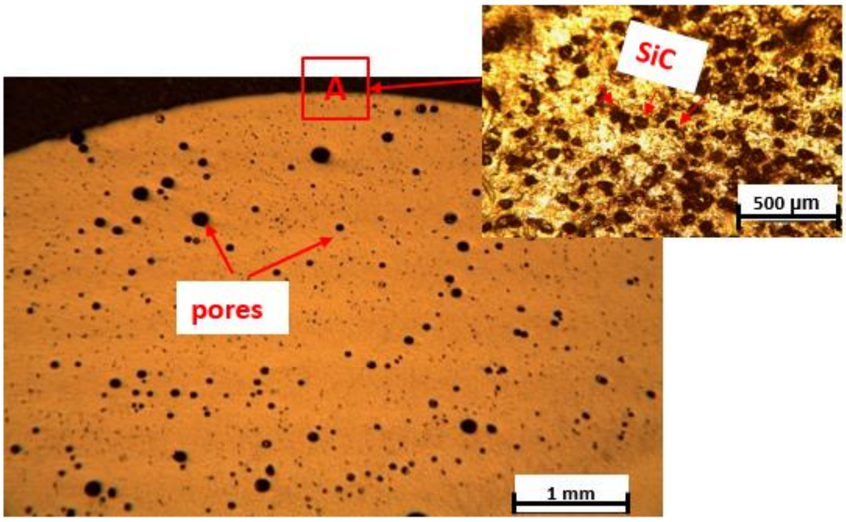

Figure 6-5: Micrographs of back fed particle injected melt bead track

6.4 Investigation of parameters controlling particle embedding in Al-SiC composites by WAAM

In the initial process investigation, SiC reinforcement particles were only embedded on the surface of melt seam tracks without penetrating the surface. The key factors identified that could possibly prevent particle penetration include:

- The rapid solidification rate of aluminium which makes it difficult for particles to penetrate the melt pool prior to solidification.
- Melt pool surface tension and oxide layer which could act as a barrier inhibiting particles from penetrating.

- The blowing away of particles by the welding arc shield which may also affect the particle velocity as well as the kinetic energy required to overcome the surface tension energy of the melt pool.

In view of this, to address the issues above, the controlling parameters for producing Al-SiC by WAAM were investigated in more detail. The study considered the following:

(a) Elimination of the filler wire to increase the melt temperature and simplify the study of particle injection.
(b) Control of conduction heat transfer from the workpiece.
(c) Effect of larger particle size (150 µm).
(d) Effect of shielding gas type (He).

6.5 Eliminating the additional wire to increase the melt temperature

6.5.1 Experimental procedure

In this section, filler wire was not used to increase the temperature of the melt pool and minimise the solidification rate. The SiC reinforcement particles were injected at the back of the melt pool as previously.

6.5.2 Results

The injection of SiC particles into a melt pool without filler wire is shown in Figure 6-6a. The melt penetration depth (see Figure 6-6c) is about twice that of the filler wire added melt bead shown in Figure 6-4a. It was observed that SiC particles were mostly deflected away from the melt pool. In Figure 6-6b, it can also be seen that the melt pool is mostly liquid at the hottest part of the arc just underneath the torch and there is apparently an oxide film flowing at the top downwards. Figure 6-6c shows macrograph of the melt bead produced. It can be seen that the melt bead geometry is characterised by porosity (white spots) with no visible particle penetration.

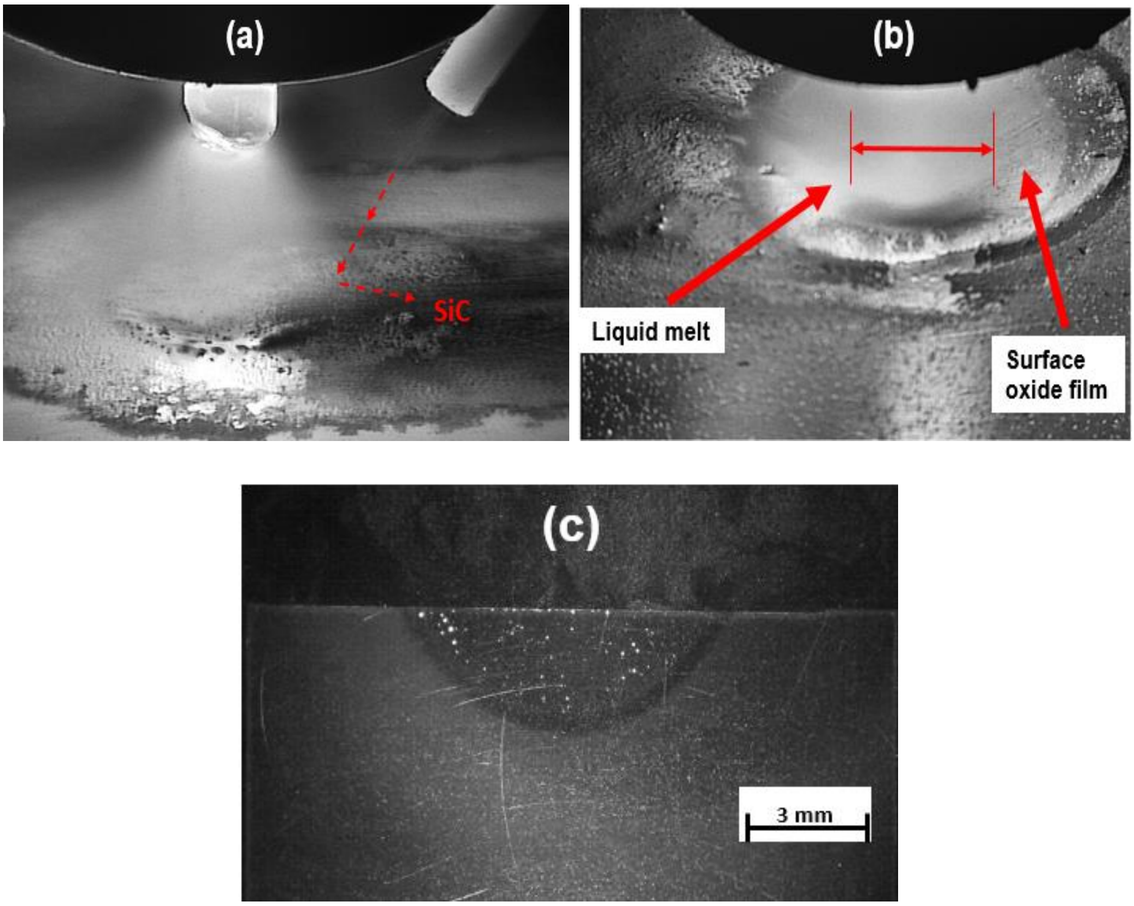

Figure 6-6: Images of weld pool without filler wire (a) particle injection in melt (b) autogenous melt pool and (c) cross section of bead with injected particles (melt penetration depth = 3.04 mm)

From the results of this section, it is apparent that the melt pool solidifies rapidly due to the high thermal conductivity of aluminium. In view of this, the next section (Section 6.6) sought to reduce the heat losses by isolating the work piece.

6.6 Isolation of thicker substrate and reduction of heat losses

6.6.1 Experimental procedure

In the previous section, SiC particles did not penetrate the melt, which indicates that the melt pool is not hot enough. For this reason, in this section, a thin plate (6 mm) and an insulating backing bar (isolation) were used to increase the melt pool temperature and minimise the conduction heat losses correspondingly. Also, the filler wire was added at the back of the melt pool to create a larger melt pool above the substrate for particle penetration.

6.6.2 Results

The effect of SiC injection using an isolated substrate is shown in Figure 6-7 for an autogenous and filler added melt pool. From the process monitoring, it was observed that SiC particles are mostly seen floating on the top of melt pool (Figure 6-7a, b). It can also be seen that a larger melt pool is created above the surface of the substrate with more SiC particles floating at the top. From the macrograph (Figure 6-7c), it can be seen that the melt area is much bigger (116 mm^2) than the one produced with the thick substrate without insulation as shown previously in Figure 6-4a (35 mm^2). Nonetheless, the results (Figure 6-7c) show no particle penetration in the melt bead.

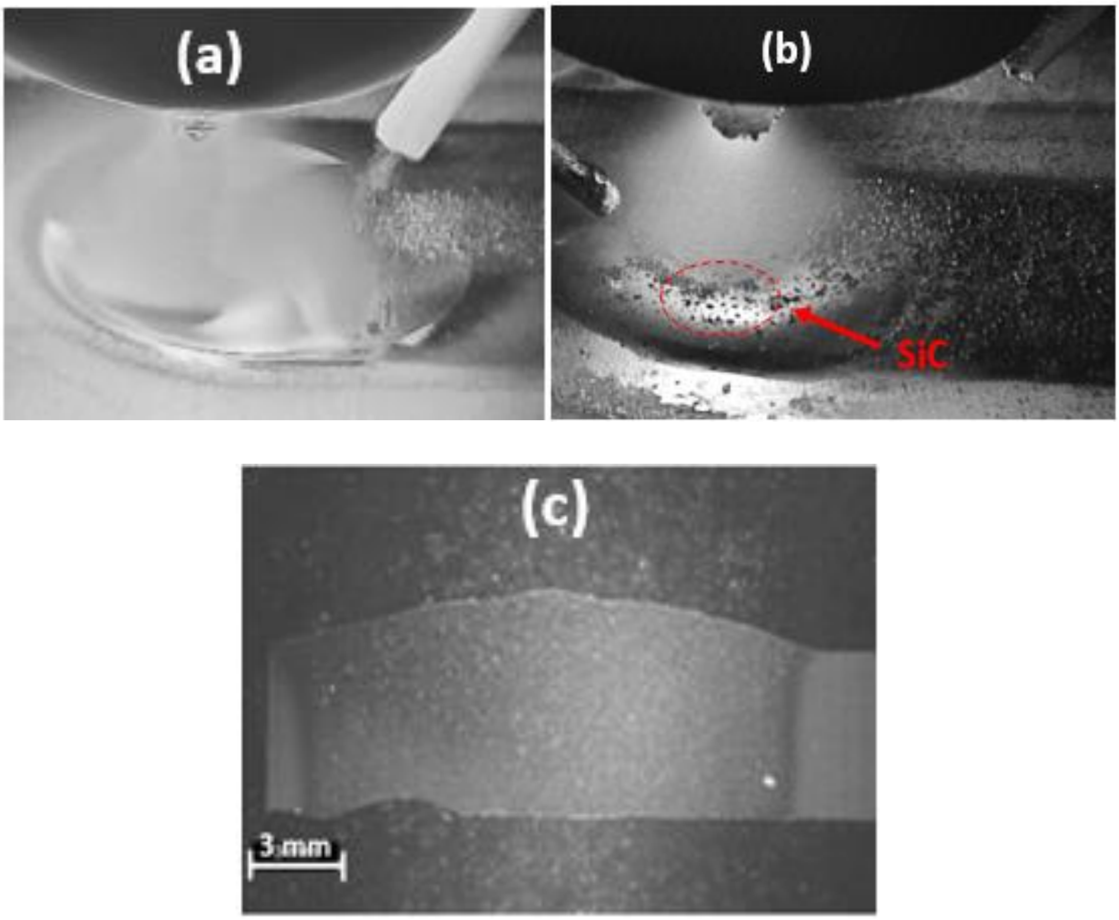

Figure 6-7: SiC particle injection in 6 mm substrate with (a) insulation and (b) insulation and additional wire; and (c) macrograph of Figure 6-7b

6.7 Effect of particle size and velocity on melt bead penetration

6.7.1 Experimental procedure

In this section, the effect of particle size and particle injection velocity on melt bead penetration was studied. Prior to this, the effect of nozzle feed diameter and carrier gas flow rate on particle velocity were assessed on the different particle sizes (75 µm and 150 µm) using a high speed camera at a frame rate of 3000 frames/s. Figure 6-8 shows the set-up for measuring the particle velocity. The high speed camera was used to measure the flight of particles as they travel from the nozzle to a set distance, ***d*** (see Figure 6-9). The distance covered was measured on a video screen by identifying and tracking particles and measuring the number of frames covered between the nozzle and the set point. Afterwards, the particle velocity ($\boldsymbol{V_{SiC}}$) was calculated using Equation 6-1.

$$\boldsymbol{V_{SiC}} = \frac{\boldsymbol{frame\ rate\ \left(^{frames}/_{s}\right)*d\ (m)}}{\boldsymbol{number\ of\ frames}},\ [\boldsymbol{m/s}] \quad \textbf{Equation 6-1}$$

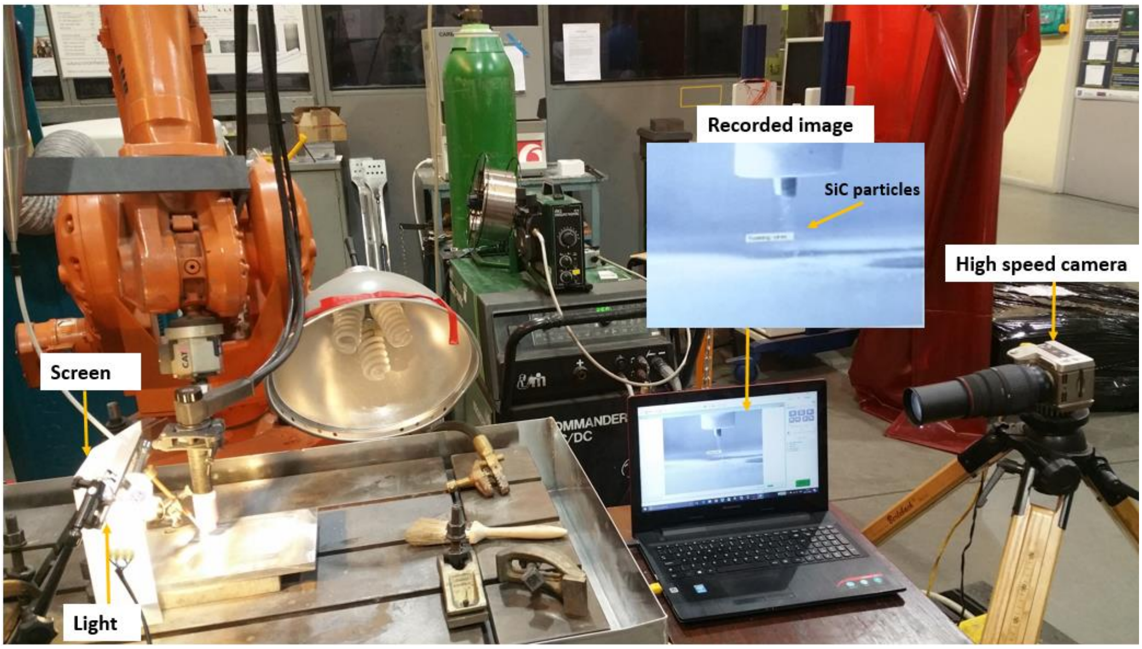

Figure 6-8: Set-up for measuring SiC particle velocity using the high speed camera

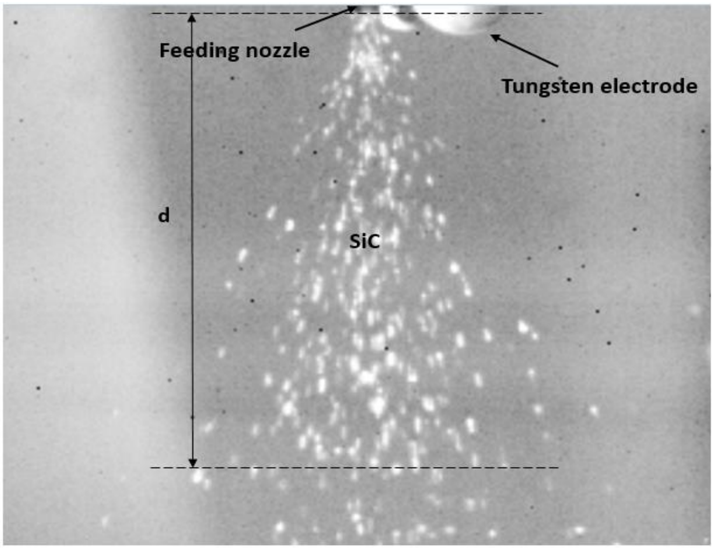

Figure 6-9: Image showing particle travel to distance

6.7.2 Results

In Figure 6-10, the effect of nozzle diameter and gas flow rate on SiC reinforcement particle velocity using the high speed camera is shown. The results show that the different nozzle diameters, carrier gas flow rate and particle sizes affect particle velocities significantly. It can be seen that SiC particle velocity increases with increasing carrier gas flow rate for the respective particle sizes. Also, particle velocities are higher for 75 µm SiC particles and lower for 150 µm SiC particles fed in a 1.6 mm nozzle diameter similarly. The lower velocities for coarser particles results from the low acceleration of larger particles.

Figure 6-11 shows plots of carrier gas flow rate and pressure against particle velocity for 150 µm SiC particles using a 2.3 mm nozzle diameter. The results show that to achieve higher velocities to that of fine particles in Figure 6-10, the carrier flow rate of coarse particles needs to be increased by a factor of 2.75. It can also be seen that a linear correlation exist for both the flow rate and pressure against particle velocity.

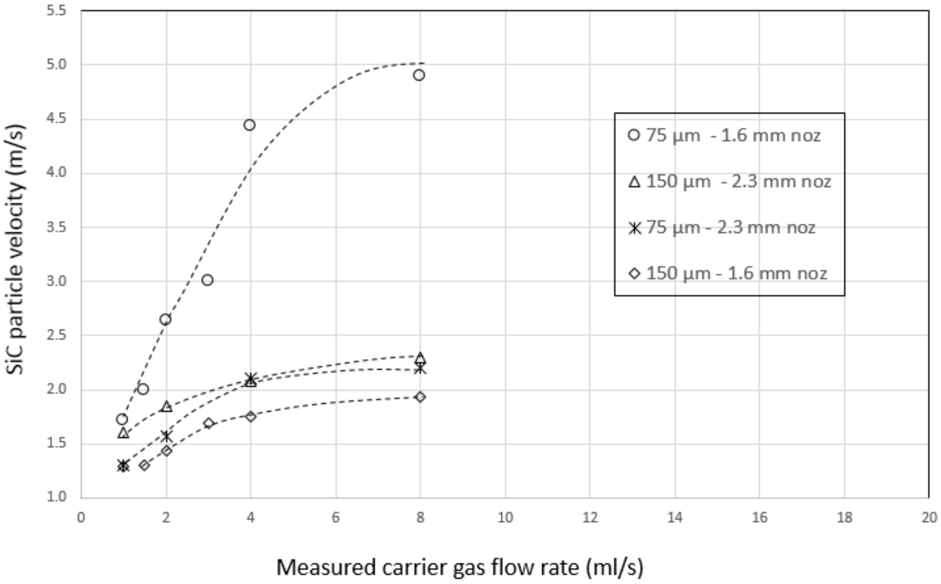

Figure 6-10: Effect of SiC particle feed nozzle and carrier gas flow rate on particle velocity

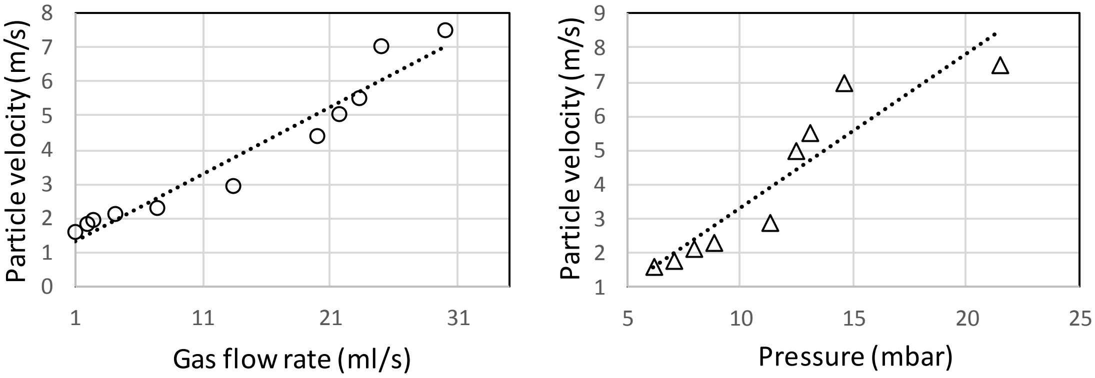

Figure 6-11: Effect of gas flow rate and pressure on particle velocity for 150 µm

Furthermore, a plot of particle velocity against the angle of spread (θ) is shown in Figure 6-12 for 150 µm SiC particles using a 2.3 mm nozzle diameter. It can be seen that increasing the particle velocity generally increases the angle of spread (θ) of the particles. The increase in the divergence of the powder may lead to reduced powder particle capture efficiency. The results also show that the angle of spread becomes constant above 2 m/s particle velocity for any significant change. Given the angle of spread is 50° and the distance from the nozzle to the surface is 5 mm, the expected area of coverage will be about 20 mm^2 which is quite wide. For a smaller nozzle of 1.6 mm diameter, the maximum angle of spread would be expected to reduce to about 30º.

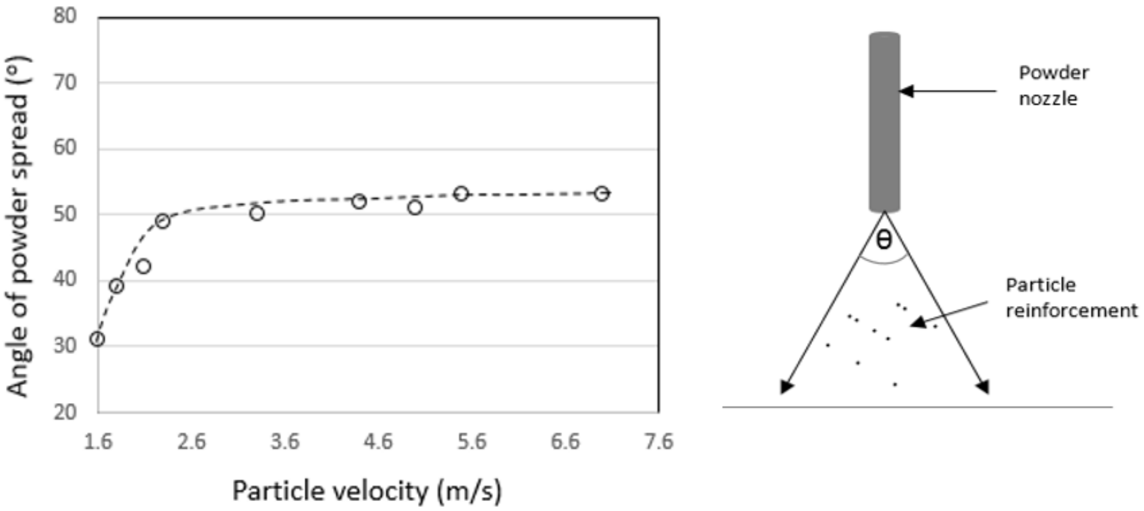

Figure 6-12: Effect of particle velocity on 150 µm SiC particle spread angle

Furthermore, the effect of 150 µm SiC particles on melt penetration was also investigated. Figure 6-13 shows the top beads of Al-SiC weld seam tracks produced. Both autogenous and filler wire added welds show a substantial amount of SiC particles on their surfaces.

Figure 6-13: Physical characteristics of Al-SiC composite weld seam tracks produced using 150 µm SiC (HI = 1.6 kJ/mm; V_{SiC} = 2.9 m/s; PFR = 22 g/min): (a) autogenous weld seam (b) Filler wire (WFS = 2.8 m/min)

Table 6-3 shows the effect of particle velocity on the penetration of the melt pool without filler wire. It is observed that particles are embedded only on the surface of the melt without any visible penetration (Figure 6-14). It can also be seen that particle velocity does not affect significantly the weld area for the different velocities used.

Table 6-3: Effect of particle velocity on particle penetration and melt area: (a) 2.4 m/s; (b) 2.9 m/s (TS = 2.5 mm/s, HI = 1.6 kJ/mm)

Particle velocity (m/s)	**Weld area (mm^2)**	**% SiC volume fraction**	**Melt geometry**
2.4	116	null	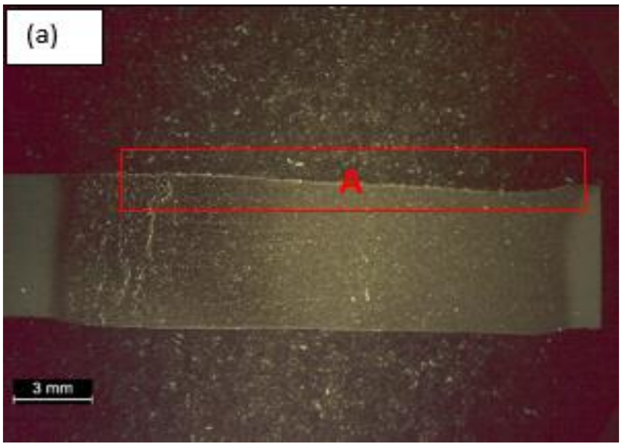
2.9	109	null	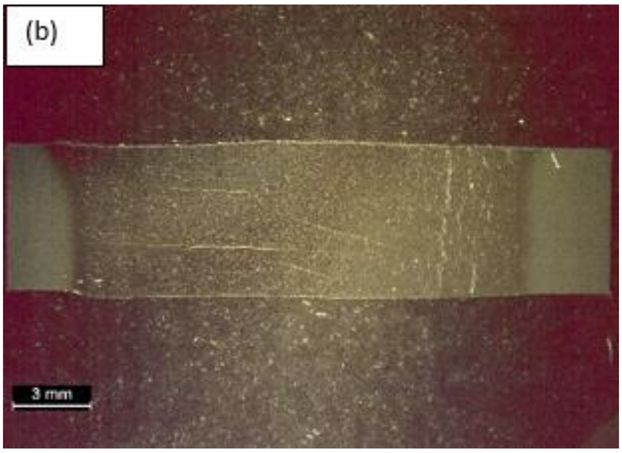

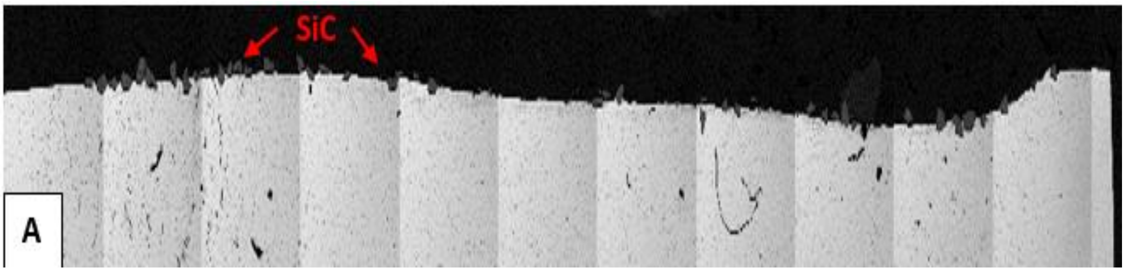

Figure 6-14: Microstructure of 150 µm SiC injection in an autogenous melt *(V_{SiC} 2.4 m/s)*

Figure 6-15 shows the nature of the melt pool during SiC particle injection with and without filler wire. It can be seen that SiC particles float on the surface of the melt.

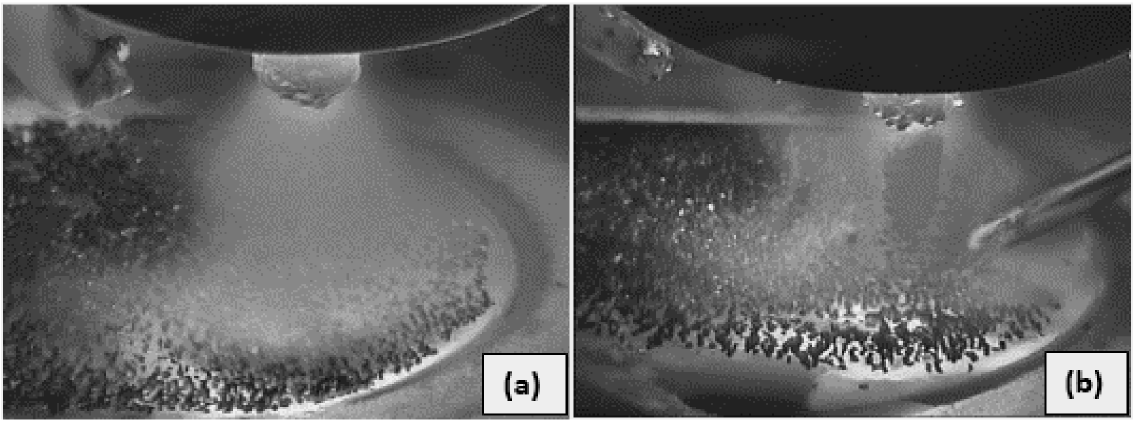

Figure 6-15: Images of autogenous and filler wire added weld seam tracks during 150 µm SiC particle injection (HI = 1.6 kJ/mm; V_{SiC} = 2.9 m/s; PFR = 22 g/min): (a) autogenous weld seam (b) Filler wire (WFS = 2.8 m/min)

The effect of increasing the powder feed rate on particle penetration is shown in Table 6-4. It can also be seen that particles are only embedded at the top of the weld seam without any particle penetration.

Table 6-4: Effect of powder feed rate on particle penetration (HI = 1.6 kJ/mm; V_{SiC} = 7.6 m/s)

Powder feed rate (%)	Weld area (mm^2)	% SiC volume fraction	Melt geometry
22	97.6	null	
31	113	null	

The effect of WFS on particle penetration and melt area is shown in Table 6-5. It can be seen that increasing the WFS increases the melt area. However, SiC particles float on the top of the melt with no particle penetration. From longitudinal micro sections, particles were embedded only partially in the top surface of the melt (see Figure 6-16).

Table 6-5: Effect of WFS on particle penetration and melt area: (TS: 2.5 mm/s HI = 1.6 kJ/mm)

WFS (m/min)	Weld area (mm^2)	% SiC volume fraction	Melt geometry	Melt pool
2.4	120	null	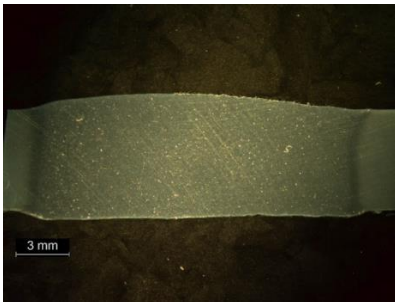	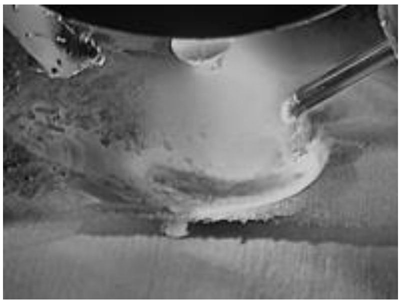
2.8	137	null	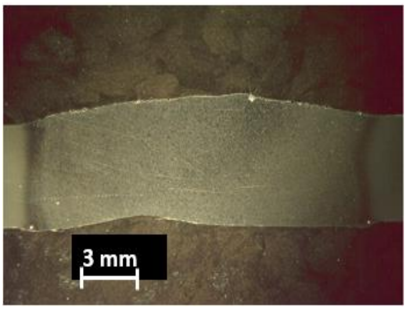	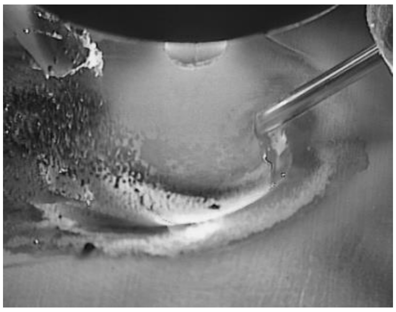

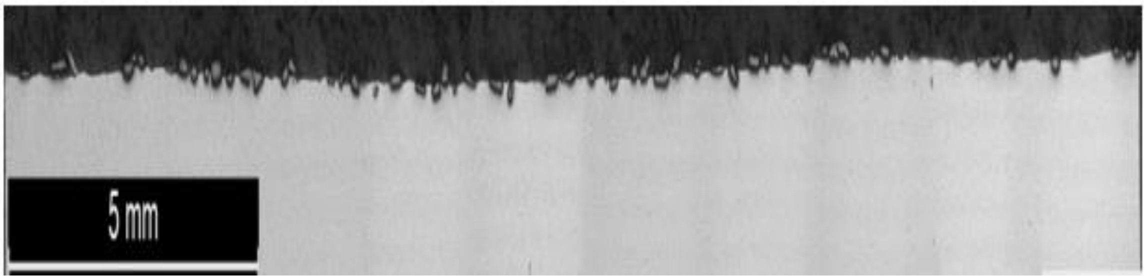

Figure 6-16: Longitudinal micro section of the top surface of melt bead showing 150 µm SiC particles at the top of weld bead (WFS: 2.8 m/min)

6.8 Effect of shielding gas on melt bead fusion and reinforcement penetration

From previous sections above, it was shown that SiC particles did not penetrate the surface of the melt pool using this range of conditions. It was supposed that the injected particles are prevented from entering the meltpool by an oxide barrier layer on the melt pool surface. It was proposed by Vreeling et al. [59] that the presence of could be due to the high thermal conductivity and surface tension of aluminium melt. Therefore there is a need to increase the heat input to increase melt pool temperature and reduce the surface tension. In Section 2.6.3, it was identified that the shielding gas plays an important role on the melt pool and droplet transfer. It was found that helium (He) gas increases the temperature and melt bead size in comparison to Argon (Ar). For this reason, this section sought to assess the effect of injecting SiC particles in a He produced melt.

6.8.1 Experimental procedure

In this study, a pure He shielding gas of flow rate 30 L/min was used in the melt deposition with subsequent injection of SiC reinforcement particles. The possibility of injecting fine and coarse particles in aluminium melt were studied. Furthermore, a comparison of the melting behaviour of Ar and He shielding gases were also investigated for 150 µm particle size for similar heat input. The comparison was done by adjusting the current and travel speed of He produced welds to obtain similar heat input as Ar shielding gas. The heat input was calculated by using the Equation 6.2. The volume fraction of particles captured was also calculated using Equation 6-3.

$$HI = (I \times V) / v \qquad \textbf{Equation 6-2}$$

current (I), voltage (V), travel speed (v)

$$\% \, \boldsymbol{SiC\ volume\ fraction} = \frac{\boldsymbol{partilce\ area}}{\boldsymbol{melt\ area}} \ \boldsymbol{x\ 100} \ (\%) \qquad \textbf{Equation 6-3}$$

6.8.2 Results

Figure 6-17 shows the effect of injecting 75 µm and 150 µm SiC into a melt pool produced by He shielding gas. From the process monitoring, it was observed that 75 µm SiC particles are mostly deflected by the arc (Figure 6-17a). This causes the arc to be erratic which in turn makes the melt pool unstable. Conversely, 150 µm SiC particles do not deflect as much, and so more particles are seen in the melt pool. Also, it was also observed that the melt pool was much colder during 150 µm SiC injection as compared to 75 µm SiC from the melt pool size.

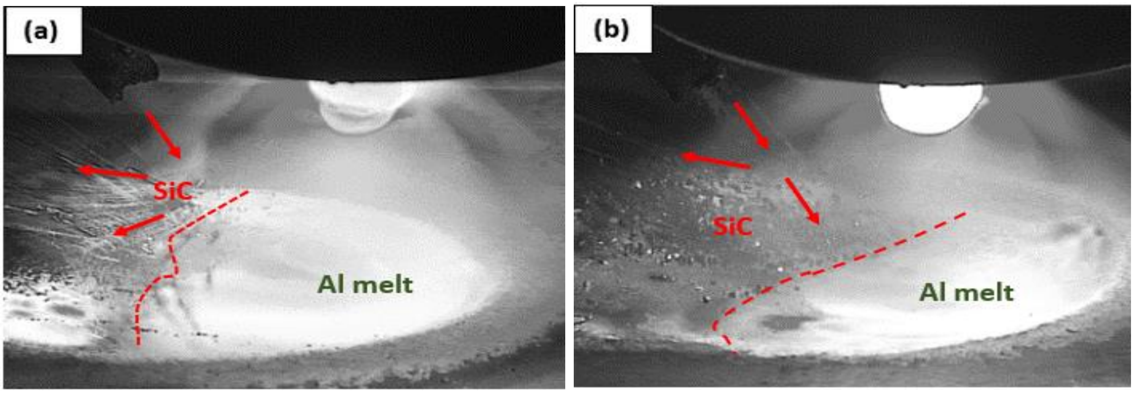

Figure 6-17: Effect of particle size on injection in melt pool produced by He shield gas (HI: 2.1 kJ/mm, V_{SIC} = 2.4 m/s, PFR = 20 g/min): (a) 75 µm; (b) 150 µm

The macrographs of injected 150 µm SiC particles in He produced melt beads with and without filler wire are shown in Table 6-6. It can be seen that particles sink to the bottom of both melt beads with more particles in the filler added melt.

Table 6-6: Macrographs of particles injected in melt beads produced (a) without filler wire and (b) with filler wire (WFS = 2.8 m/min)

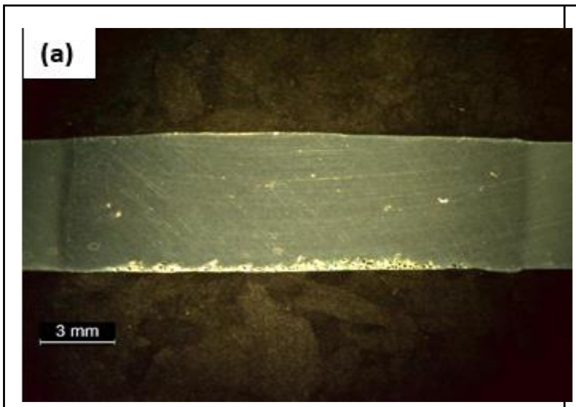	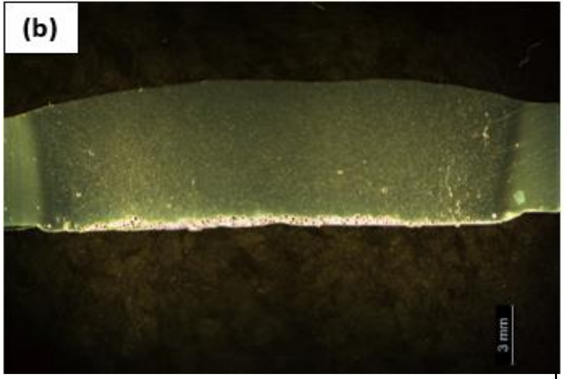
HI = 2.1 kJ/mm Weld area = 113 mm^2 % SiC volume fraction = 0.08 %	HI = 2.2 kJ/mm Weld area = 165 mm^2 % SiC volume fraction = 0.25 %

The effect of the shielding gas type on the melt pool during particle injection is shown in Figure 6-18. For similar heat inputs, it can be inferred that the melt pool is much colder with Ar shielding gas (Figure 6-18a) than He shielding gas (Figure

6-18b and 6-18c) during deposition. It was observed that SiC particles were mostly seen floating at the top of Ar melt bead as compared to that of He.

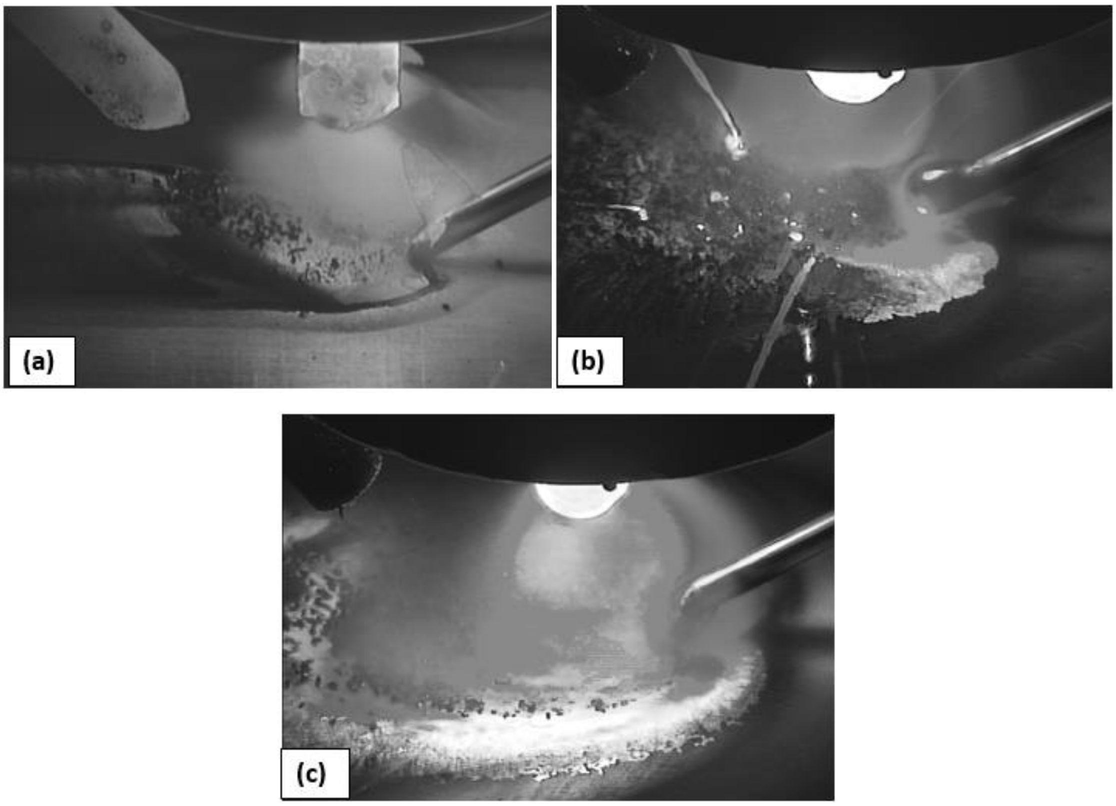

Figure 6-18: Effect of shielding gas on melt pool behaviour during SiC particle injection: (a) Ar (TS = 2.5 mm/s); (b) He (TS = 2.5 mm/s) and (c) He (TS = 4.1 mm/s)

Figure 6-19 compares the macrographs of the above melt beads produced by Ar and He shielding gas for similar heat inputs. It can be seen that the melt area of He gas is about 50 % higher than that of Ar shield gas. This indicates that He is much hotter than Ar and produces a larger melt pool than Ar even for similar current. This may be caused by the better melting efficiency of He gas. It can also be seen that particles injected penetrate to the bottom of He produced melt beads whereas no visible penetration is identified in Ar produced melt beads. The results also show that increasing the travel speed increases the melt area for similar heat inputs in He.

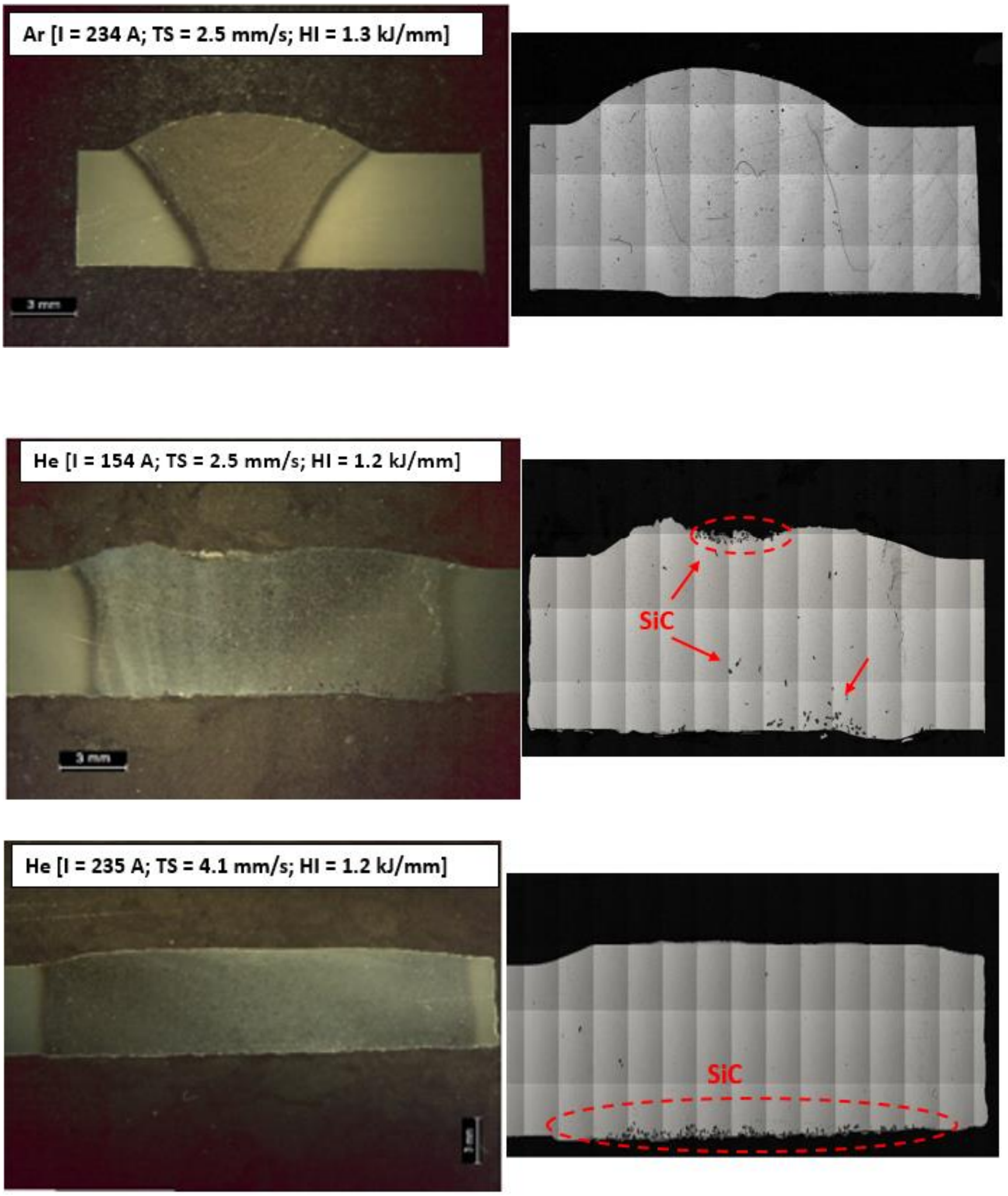

Figure 6-19: Melt bead cross sections showing the effect of shielding gas on particle penetration

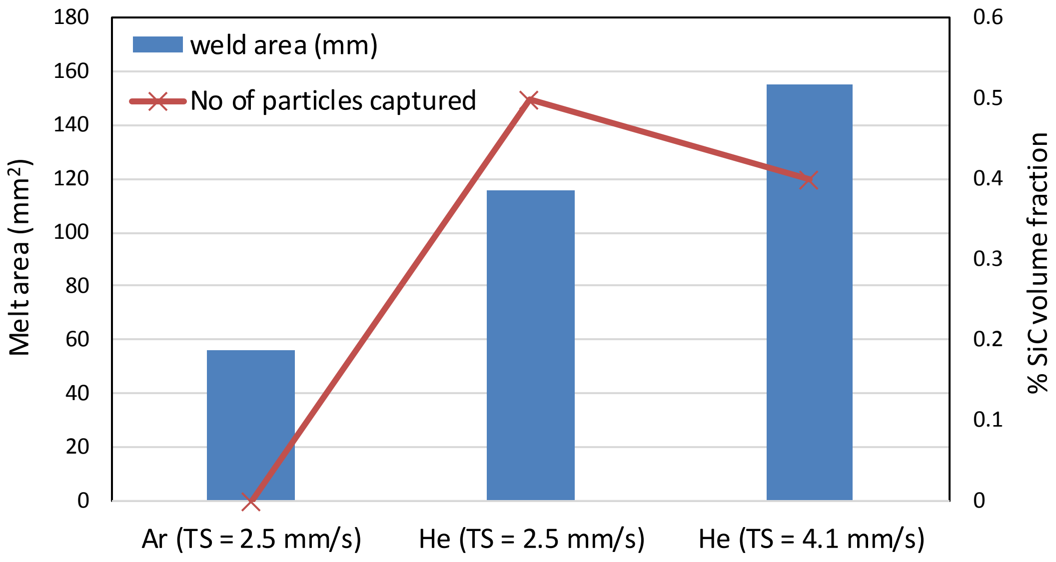

Figure 6-20: Effect of shielding gas type (Ar and He) on melt area and number of particles captured.

The effect of Ar and He shielding gases on the melt area of melt seam tracks is shown in Figure 6-21. The results show that increasing the heat input generally increases the melt fusion area. It can also be seen that for the same heat input range, He shield gas produces larger melt beads than Ar shield gas. This shows that He shield gas produces a hotter arc than Ar.

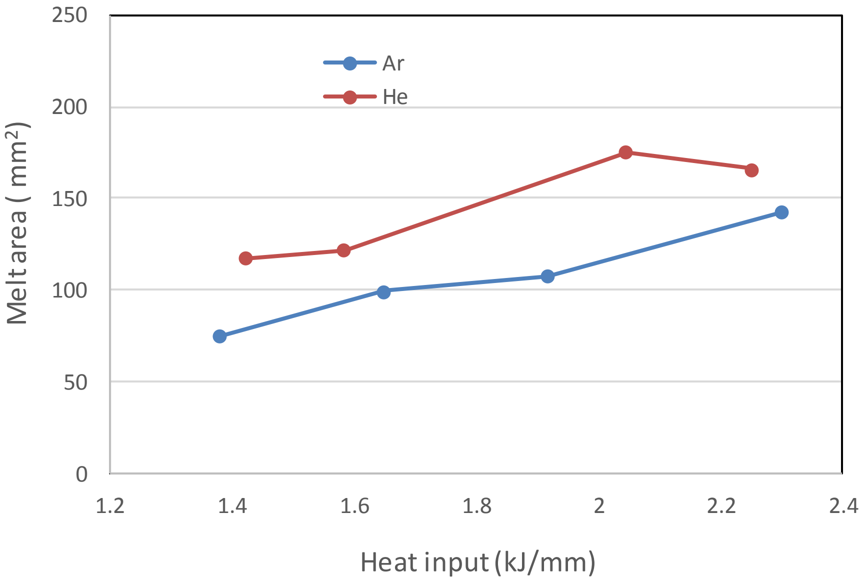

Figure 6-21: Effect of Ar and He shielding gas on melt area

The effect of increasing particle velocity to increase the number of particles injected in the melt is shown in Figure 6-22. From melt pool monitoring, it was observed that the high carrier gas flow rate associated with increasing particle velocity appears to blow the melt pool. This causes the melt pool to go sideways during the injection process. From the macrographs, it can be seen that increasing the particle velocity reduces the particles embedded in the aluminium matrix. Figure 6-22 b;c, it can be seen that melt beads show protrusion and gaps at the base of the substrate indicating significant melt flow. It is likely that the plate may have been lifting off the table during the injection process to allow this melt flow behaviours on the bottom surface.

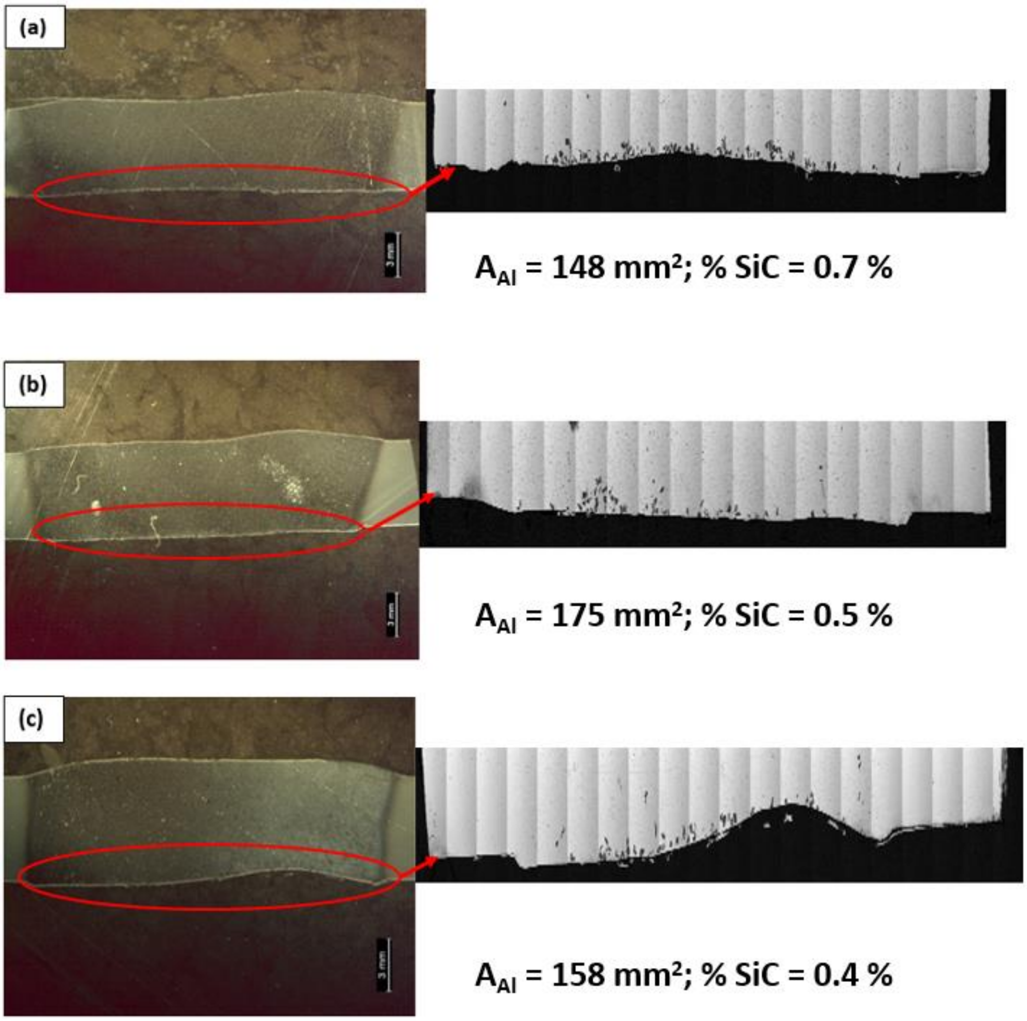

Figure 6-22: Macrostructure of weld seam tracks produced with increased particle velocity with respect to WFS (HI = 2.2 J/mm; PFR = 22 g/min): a. 2.4 m/s / 2.8 m/min;

b. 4.4 m/s / 3.2 m/min; c. 7.6 m/s; 3.2 m/min (where, A_{Al} and % SiC signify the melt area and the % volume fraction of SiC)

In Figures 6-23, the effect of heat input on the number of particles captured per melt area is shown. It can be seen that increasing the heat input increases the number of particles captured per unit melt bead area. The macrostructures also show improved distribution of particles in the melt bead produced with the maximum heat input. Also, it can be seen that increasing the heat input increases the melt area. However, the inconsistency of the melt area at maximum heat input is likely to be due to the reduced travel speed which increases the amount of particles embedded per unit length.

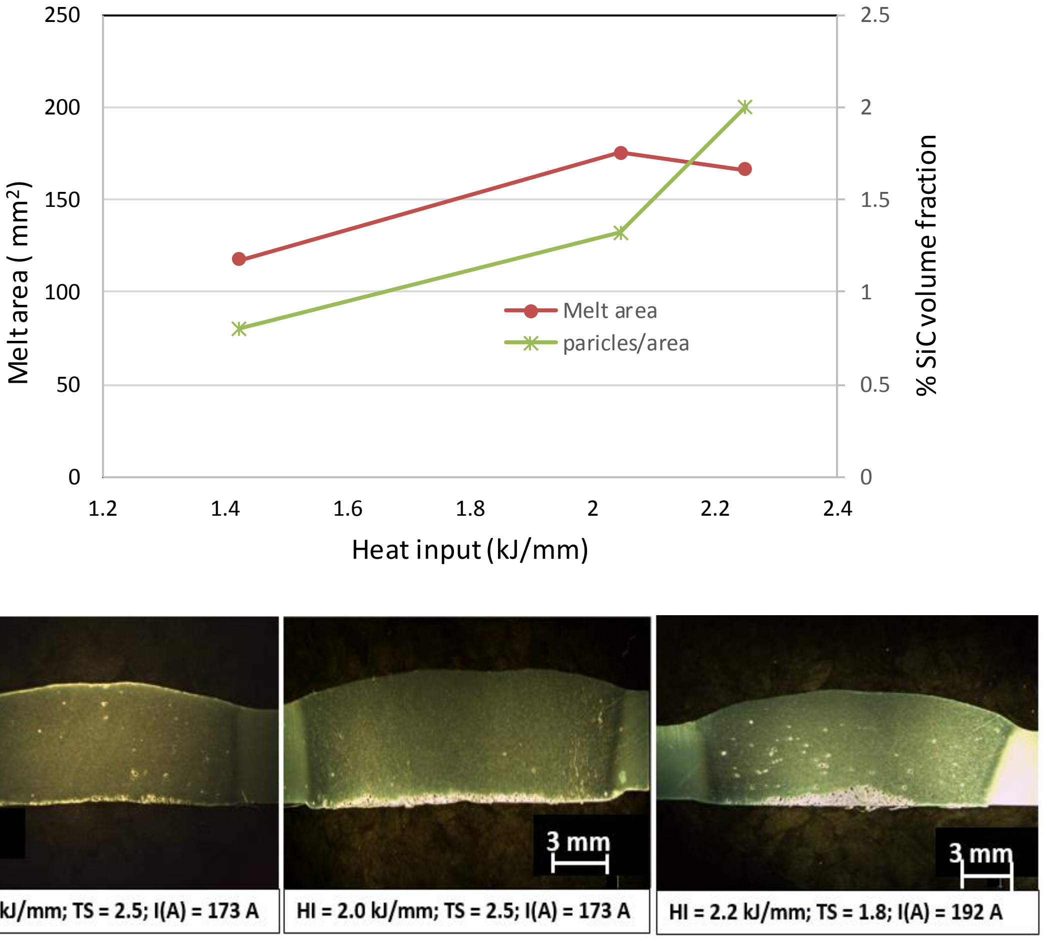

HI = 1.4 kJ/mm; TS = 2.5; I(A) = 173 A

HI = 2.0 kJ/mm; TS = 2.5; I(A) = 173 A

HI = 2.2 kJ/mm; TS = 1.8; I(A) = 192 A

Figure 6-23: Effect of He shielding gas heat input on melt area and particles injection (WFS: 2.8 m/min; V_{SiC}: 2.4 m/min; PFR: 22 g/min)

Table 6-7 shows the effect of increasing the powder feed rate on the amount of particles embedded in the melt pool. The results generally show that increasing the particle feed rate increases the number of particles captured per melt area.

Table 6-7: Effect of powder feed rate (PFR) on the number of particles captured, (a) 22 g/min; (b) 31 g/min; (c) 37 g/min.

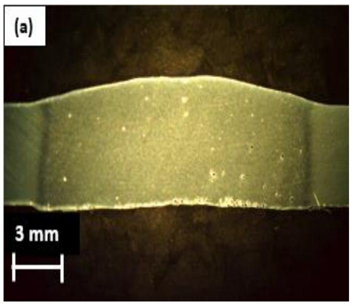	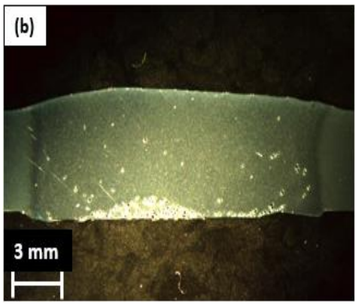	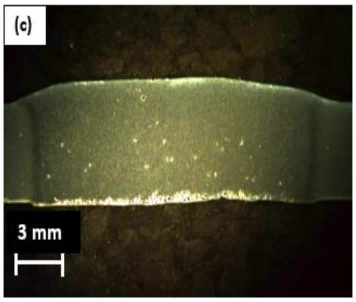
% vol SiC = 0.8 % SiC	% vol SiC = 1.5 % SiC	% vol SiC = 1.4 % SiC

The hardness results across the surface of the melt bead with varying SiC particle feed rate are shown in Figure 6-24. The hardness values range between 70 HV and 90 HV with a significant increase in the hardness at the bottom with SiC reinforcement. It can also be seen that the higher feed rate showed increased hardness at the bottom as compared to the low feed rate. This corresponds to findings from the macrograph where most particles are located at the bottom of the melt pool.

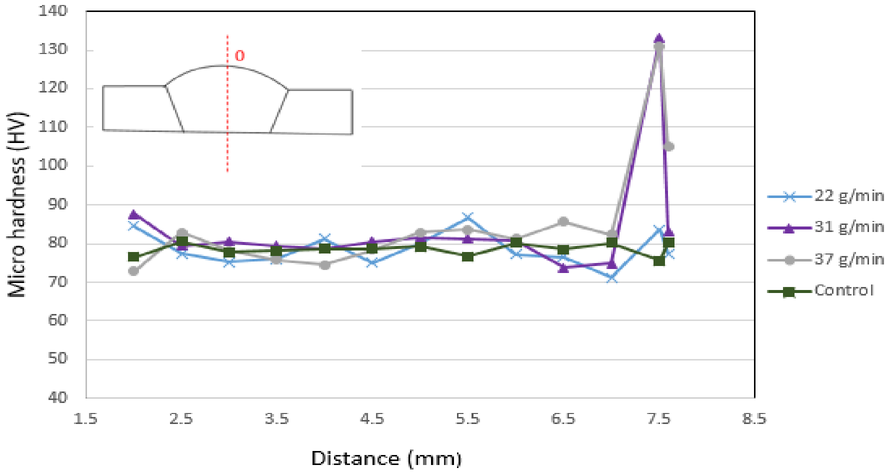

Figure 6-24: Effect of particle feed rate on the micro hardness in the vertical direction of micro sections

Furthermore, the hardness measurements along the surface of a melt bead are shown in Figure 6-25. From the results, it can be seen that areas of particle embedment show extremely high hardness as compared to areas of no particles.

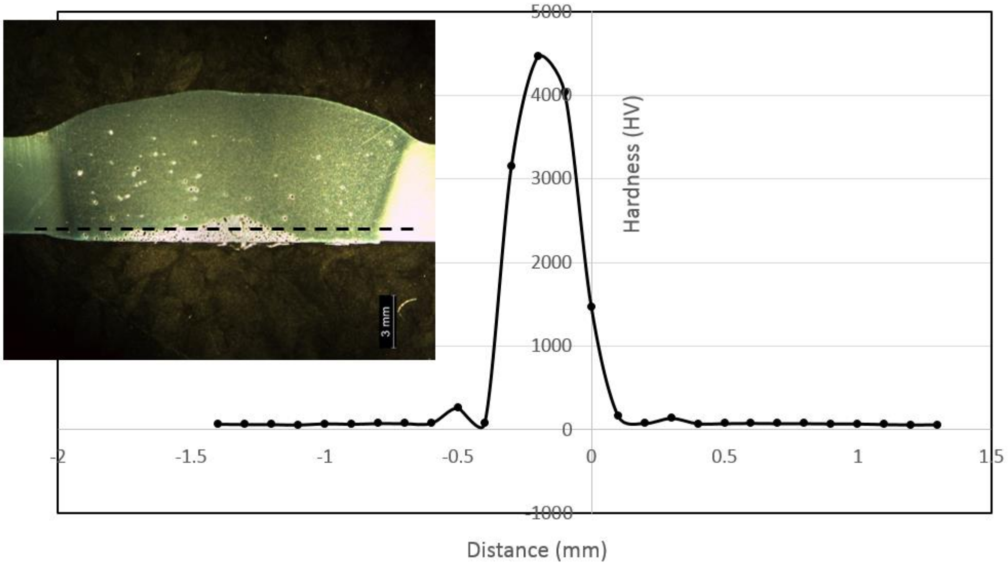

Figure 6-25: Micro hardness results measured in the horizontal part of the microstructure

The microstructure of SiC reinforced aluminium composites is shown in Figure 6-26. The results show 50 % volume fraction of SiC with uniform distribution of particles which are well enveloped by the matrix. This shows that the two materials used are compatible.

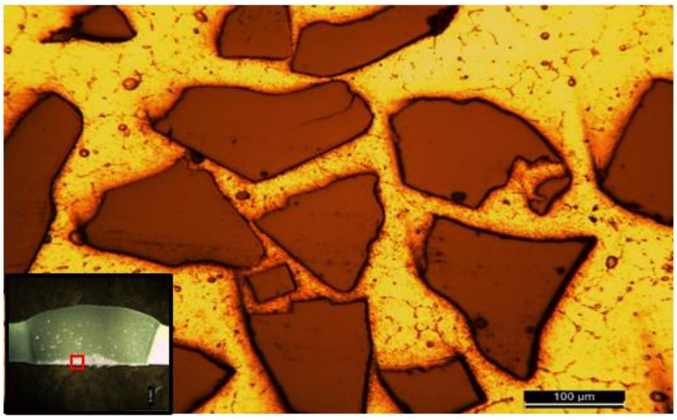

Figure 6-26: Microstructure of SiC particle reinforced in aluminium melt bead

6.9 Laser melt injection of SiC in aluminium melt

For this research the objective is to achieve a uniform distribution of SiC particles in the entire melt. In view of this, the next step was to use the laser melt injection process (LMI) which is a more controllable and precise heat source to melt the substrate with subsequent injection of SiC particle reinforcement. From studies by Vreeling et al. [59], the main controlling parameter for successful injection is the melt pool temperature. For this reason, the substrate was insulated to minimise the conduction heat losses to maximise the melt pool temperature.

6.9.1 Experimental procedure

The experiments in this section were performed using an 8 kW IPG YLR-800 CW multimode fibre laser. Figure 6-27 shows the experimental set-up for producing Al-SiC composites using the LMI process. The laser beam used to create a melt pool was at an angle of 7° perpendicular to the substrate to avoid back reflections into the fibre delivery system. The substrate used was Al 6082-T6 with dimensions 200 mm x 200 mm x 6 mm. 150 µm SiC particles were injected at the back of the melt pool at an angle of 40° using the Sulzer Metco TWIN-10-C R2 powder feeder. Pure argon gas was used for shielding to minimise oxidation of the aluminium melt. Table 6-8 shows the parameters used in these experiments. The study was conducted on both bare and, in order to increase the absorption of the laser beam, graphite coated substrates. The effect of the laser power and spot size on the injection process was investigated.

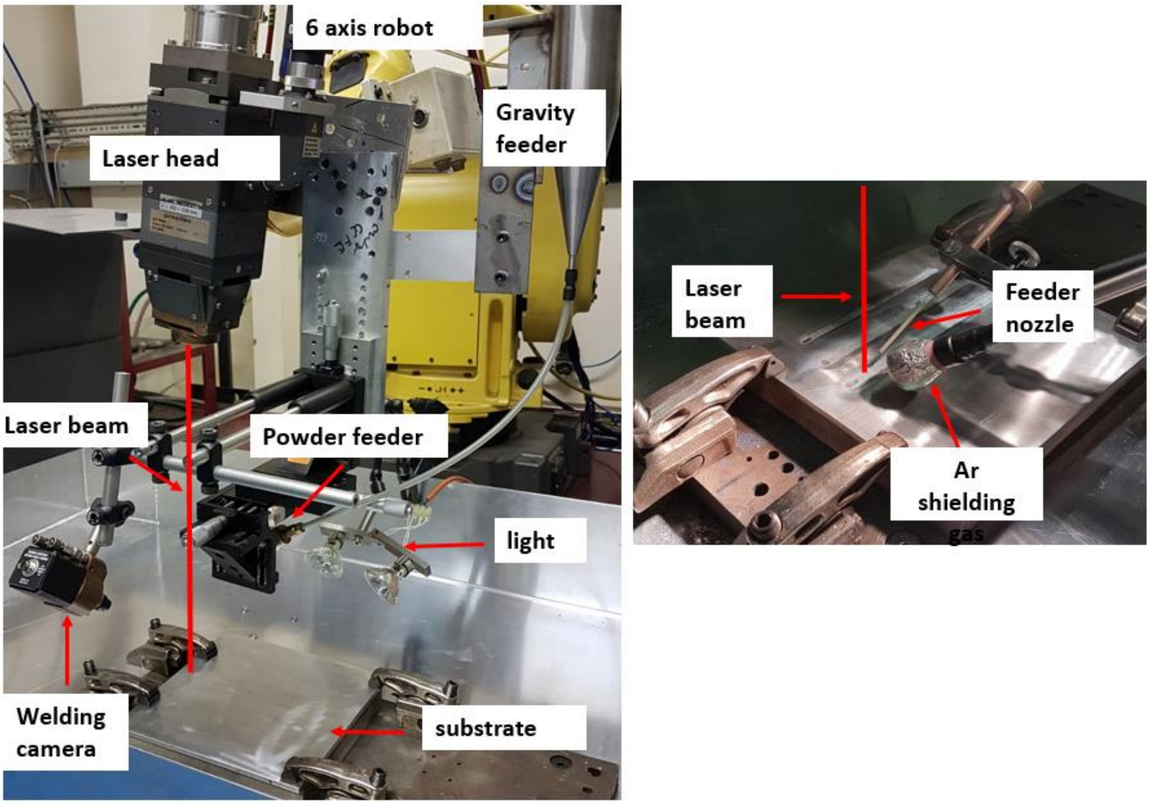

Figure 6-27: Laser melt injection set-up (left) and position of feeder nozzle relative to the substrate (right).

Table 6-8: Parameters used in the LMI of AlSiC

Trial	Power (kW)	Coated	Spot size (mm)	Melt area (mm^2)	Melt Penetration depth (mm)
A 1	3	Non-coated	15	30.2	4.0
A 2	5	Non-coated	15	31.7	4.4
A 3	5	Coated	15	113	6
A 4	5	Coated	5	43	5.8
A 5	5	Non-coated	5	27.8	4.5

Travel speed of laser: 0.15 m/min; V_{SiC}*: 2.4 m/min; PFR: 22 g/min*

6.9.2 Results

In Figure 6-28, the top surface of the laser melt seam tracks are shown for both coated and uncoated substrates for the spot size of 5 mm (A4 and A5). The results show that SiC particles are uniformly distributed on the top of the melt bead tracks as depicted by the arrows. On the other hand, no visible particles were seen in samples A 1-3.

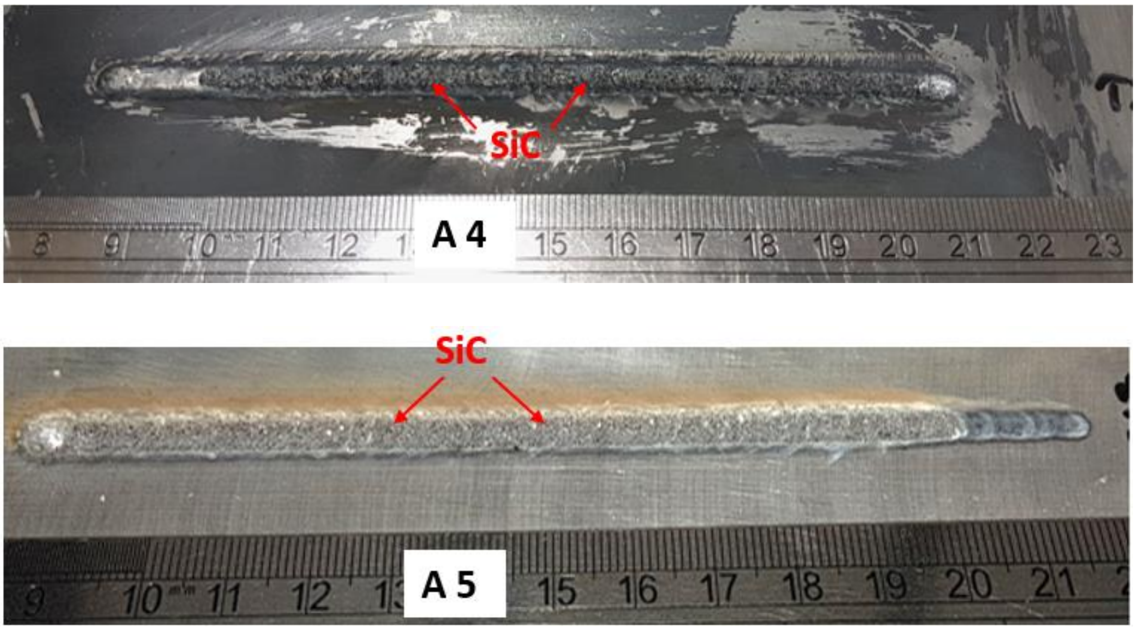

Figure 6-28: Laser melt seam tracks for coated (A4) and uncoated (A5) substrates

The macrostructures of the melt seam tracks produced from Table 6-8 are shown in Figure 6-29. The results reveal that the particle penetration depth is 1.5 mm in the uncoated substrate with a laser spot size of 5 mm (See Figure 6-29; A5). Conversely, this was not the case for the graphite coated substrate for the same parameters (Figure 6-29; A6). From the macrographs, it can be seen that graphite coated samples show an increased size of melt bead geometries which indicate a higher melt pool temperature. Nonetheless, no visible particle penetration is observed.

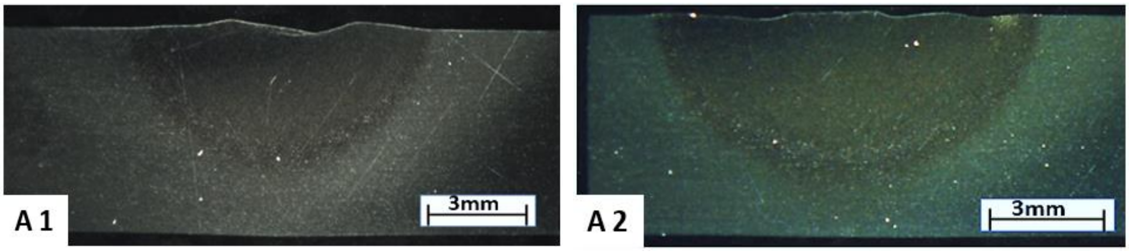

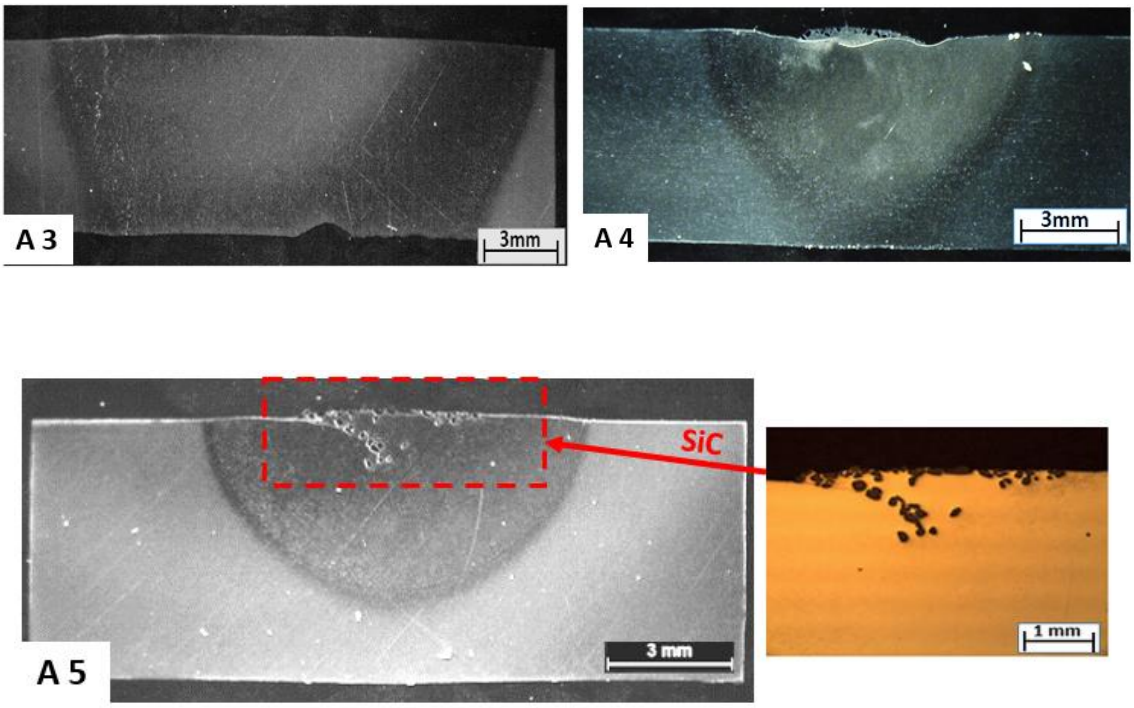

Figure 6-29: Macrograph of SiC injected particles in the LMI process depicting their measured melt areas: A1 = 30.2 mm ^{2}; A2 = 31.7 mm ^{2}; A3 = 113 mm ^{2}; A4 = 43 mm ^{2}; A5 = 27.8 mm ^{2}

The behaviour of SiC particles during the laser melt injection process is shown in Figure 6-28. It can be seen that SiC particles are mostly deflected opposite to the feeder nozzle direction. It can be seen that the particles are mostly deflected due to the small melt pool size. This may be because of the wider coverage area of particles as explained in Figure 6-12.

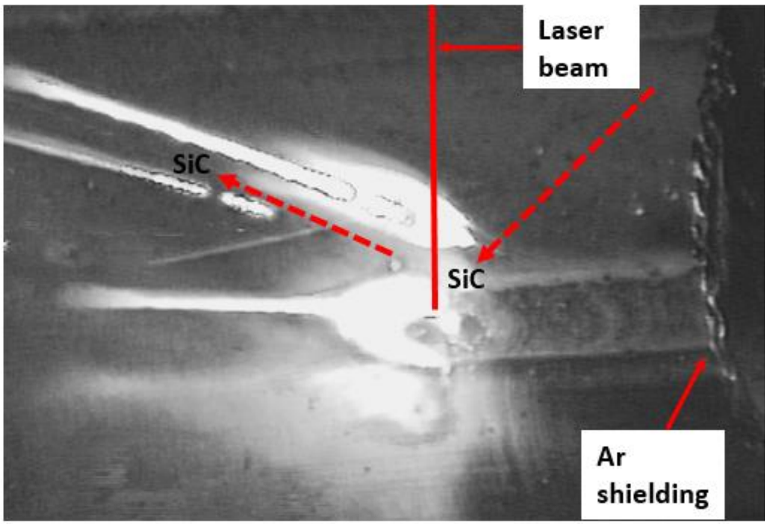

Figure 6-30: Al-SiC Laser melt injection process monitoring for Trial 5

6.10 Discussion

6.10.1 Process development

An alternative manufacturing option for aluminium silicon carbide (Al-SiC) metal matrix composites has been investigated using ACTIG WAAM. The optimum direction of injecting SiC particles into aluminium melt was back feeding where both the arc and melt pool were stable with particles dispersed on the top surface of the melt without disturbing the arc (Figure 6-2a). The problem is because of the low density and low viscosity of aluminium melt which led the study to consider the direction of the gas from the powder feed system. It was evident in the case of side and front fed particles that the carrier gas blows the melt pool during deposition. The effect of the carrier gas on the melt beads were an unstable melt pool in the case of front fed particles (Figure 6-2b) and an irregular melt bead shape in the case of side fed particles (Figure 6-4b). From microstructure analysis (Figure 6-5), it was found that SiC particles were only embedded on the surface of melt seam tracks without any visible penetration in all cases. From previous work by Vreeling et al. [59], it is known that low temperatures of the melt pool results in a thick oxide layer at the top and particles cannot penetrate. When using a thick Al plate the high thermal conductivity means that the temperature of the melt pool is very likely to be low leading this problem. Furthermore Figure 6-2a shows that the melt pool was small meaning that most of the particles will not penetrate. Also a colder melt pool will have a low fluidity making it difficult for particles to penetrate. In addition from the process monitoring, it is clear that SiC particles could be partially deflected by the arc which may also affect the kinetic energy and momentum of particles required to overcome the surface tension energy of the melt pool by reducing the injected particle velocity. More importantly this deflects the particles away from the hottest part of the meltpool where the oxide layer will be thinnest and likely to be broken up. From the above, it was concluded that the possible factors to increase the particle penetration into the melt were a more fluid melt pool of high temperature and an increased particle injection velocity for the particles to penetrate into the melt pool.

6.10.2 Effect of process parameters on SiC particle injection in aluminium melt

The previous section confirms the literature [59] indicating that a hot melt pool is needed to allow particle injection to be successful. This is for several reasons:

- To avoid the thick oxide layer
- To generate a larger meltpool so that the particles have time to enter and distribute before solidification occurs
- To increase the fluidity of the liquid metal

To increase the melt pool temperature a simple approach would be to increase the current. However, too high an energy input may result in heating and damaging of the SiC particles [59] as they cross the arc column making the melt pool unstable. Therefore two different approaches were taken. Firstly the substrate thickness was reduced from 12 mm to 6 mm and this was insulated from the support structure. Secondly trials were carried out both with and without filler wire. Comparing Figures 6.6 and 6.7 it can be seen that both of these measures significantly increased the size of the melt pool and therefore the temperature. However there was still no significant particle penetration into the melt pool and they were all still on the top surface.

From the study by Vreeling et al. [59] using laser melt injection process, it is shown that the melt pool surface tension and the particle velocity are the limiting factors to particle penetration. The authors explained that for successful injection of SiC particles, the kinetic energy of particles must exceed the surface energy of the liquid metal. Therefore a study was carried out to quantify the particle velocity and see if this was sufficient to penetrate the oxide layer as indicated by Vreeling [2]. By adapting Equation 2-1 the effect of particle velocity on kinetic energy (E_{kin}) was assessed for the respective particle sizes, 75 µm and 150 µm. The study also assessed the effect of particle velocity on momentum (M) of both the fine and coarse SiC particles (see Equation 6-4). Both the KE and M were calculated by adapting particle velocities of flow rates between 1 ml/s and 8 ml/s for 1.6 mm nozzle diameter as shown in Figure 6-10.

$$\boldsymbol{E_{kin} = \frac{2}{3}\pi R^3 \rho_{SiC} v_0^2;}$$

$$M = \frac{4}{3}\boldsymbol{\pi R^3 \rho_{SiC} v_0} \qquad \textbf{Equation 6-4}$$

$$(\rho_{SiC}, density\ of\ SiC = 3217\ kg/m^3)$$

Figure 6-31 shows the effect of particle velocity on the kinetic energy (KE) and momentum (M) of SiC particles. Note that the velocity ranges calculated pertain to those achievable for each particle size. The results show that 150 µm SiC particles achieve much high momentum values as compared to the 75 µm particles. This is attributable to the large difference in momentum of coarse particles which is proportional to the mass. In contrast both 75 µm and 150 µm particles show similar KEs for the range of flow rates available (maximum 8 ml/s).

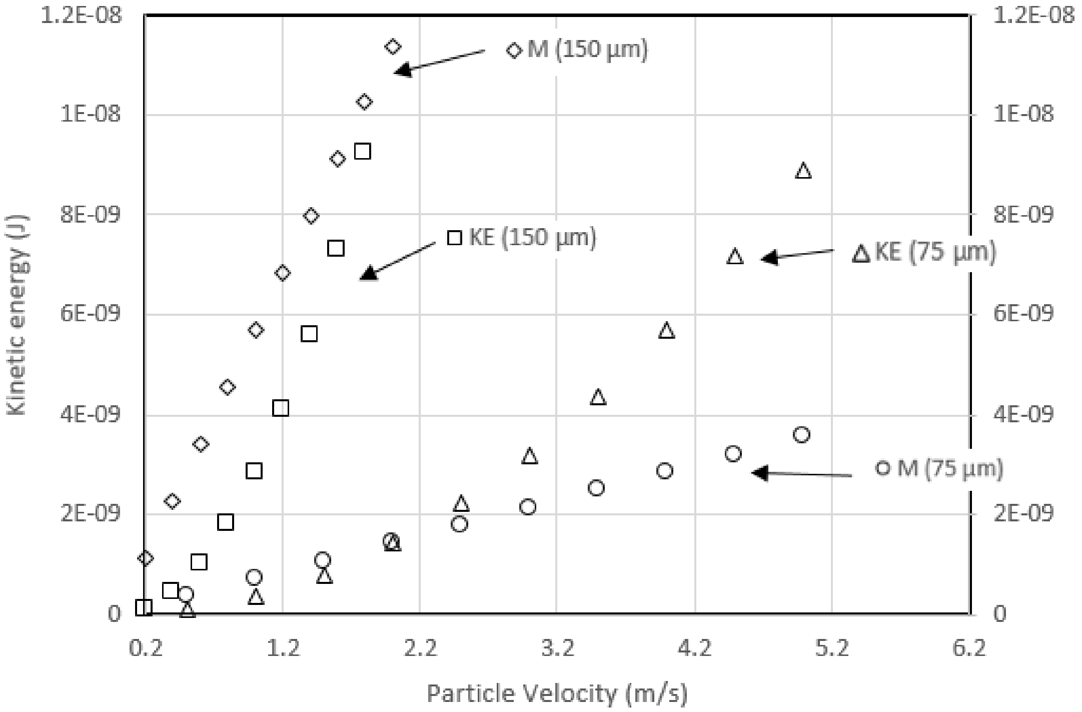

Figure 6-31: Effect of particle velocity on kinetic energy (KE) and Momentum (M) for 75 µm and 150 µm (nozzle diameter = 1.6 mm)

In addition, by using Equation 2-7, the minimum velocity (V_{min}) required for particle penetration was also calculated for both oxidised and unoxidised melt pool (see Table 6-9).

$$\boldsymbol{v_{min}} = \sqrt{\frac{\mathbf{3}}{\mathbf{2}\boldsymbol{\sigma_{1v} R \rho_{SiC}}}} \left(\boldsymbol{\sigma_{1v}} + \boldsymbol{\sigma_{1p}} - \boldsymbol{\sigma_{pv}}\right)$$

Where σ is the interface tension specified by the indices: 1 = liquid Al, p = solid SiC particles v = vapour (see Table 2-2).

Table 6-9: Minimum velocity required for particle penetration

Particle Size diameter (µm)	Velocity Oxidised (m/s)	Velocity Unoxidised (m/s)
75	4.5	2.0
150	3.2	1.5

The results (Table 6-10) indicate that low particle velocities will be required by coarse particles to break surface oxides and penetrate as compared to fine particles. The higher momentum of coarse particles can generate a higher force to overcome the penetration depth of the oxide layer (Figure 6-31). The effect of coarse particles on the injection process was also assessed in Section 6.7. In Table 6-3, the physical characteristics of melt beads produced using coarse particles (150 µm) were displayed. From microstructure analysis, coarse particles partially penetrated the melt surface (see Figure 6-14 and Figure 6-16).

In Section 6-8, switching the shielding gas from Ar to He for the same heat input resulted in larger melt bead sizes (6-21). Due to the higher voltage drop in He, either the current or the travel speed was adjusted to obtain the same heat inputs as Ar (Figure 6-19). The cross section of the melt seam tracks revealed penetration of the injected 150 µm SiC particles in the melt beads. The particle penetration can be attributed to the higher heat input of He shielding gas indicating a hotter melt pool which breaks the surface oxides. This confirms studies by Peasura and Watanapa [112] on the influence of shielding gas on aluminium 5083 alloy during TIG welding. Studies conducted by Campbell et al. [105] on the effect of shielding gas on melt behaviour of steel for different gases indicated that Marangoni flow influences the wider bead width produced by He shielding gas as compared to Ar produced melt beads for the same heat input. Marangoni flow is caused by the surface tension gradient which arise due to regions of warm and cold materials. According to Kou [104], warm melt pool is pulled outward by the colder melt and the surface tension gradient induces a shear stress causing the melt pool to flow from the centre to the edge. In this study, by comparing the Ar and He produced melt beads for aluminium (See Figure 6-19), there seem to be differences in the flow pattern of aluminium melt pool for the different shielding gases. This can affect the injection and localisation of particles at the bottom of the melt pool. In He, the Marangoni flow appears to be a reversed flow pattern resulting in a wider melt bead (Figure 6-19) and a downward flow in the centre which in turn drags the particles down (Figure 6-32). On the other hand the flow pattern in Ar also appears to affect particles clustering at the top surface of the melt bead. In Figure 6-19, it can also be seen that the longer time of melting affects the penetration depth of particles. The results of the He melt beads produced indicate that increasing the travel speed to match the heat inputs results in increasing the melt areas with localisation of particles at the bottom. The increased melt area is attributable to the reduction in heat losses for higher travel speeds. This explains the differences in the locations of SiC particles for the melt beads produced.

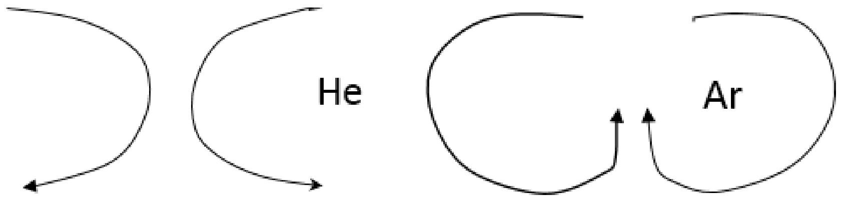

Figure 6-32: Marangoni flow patterns in He and Ar produced melt beads

The study showed that there could be a limit to the injection velocity of particles used with respect to the melt area as can be seen in Figure 6-22. For the injection process used, increased particle velocity was mainly achieved by increasing the carrier gas flow rate. The higher carrier gas flow rates resulted in blowing the melt pool sideways as a result making the melt pool unstable.

From the results of the heat input analysis, there is a direct correlation between heat input and the number of particles captured (Figure 6-23). Increasing the heat input increases the melt temperature which in turn allows more time for the particles to sink to the bottom during the injection process. In addition, the study also showed that increasing the particle feed rate increases the number of particles injected in the melt bead, Table 6-7. From the studies, the limiting factor to the maximum particles fed could be based on the melt instability from the high carrier gas flow rate resulting from the higher cone angle of the gravity feeder. The high carrier gas flow rate could potentially result in reducing the melt temperature. Therefore to increase the feed rate and maintain the melt stability, the cone angle must be reduced or the heat input can be increased.

From the micro hardness results (Figure 6-24 and 6-25), it was found that the hardness values were higher in the areas of the micro sections with particles. This can be correlated to the high hardness of SiC particles which enhances the hardness of the aluminium matrix. From the microstructure analysis, SiC particles were uniformly distributed in the matrix (Figure 6-26).

6.10.3 Laser melt injection of SiC in aluminium melt

The capability of the laser melt injection process for producing Al-SiC has also been demonstrated (see Section 6.9). In this study, particle penetration was achieved using 5 kW laser power with spot size of 5 mm and travel speed of 0.15 m/min on an uncoated substrate. The results of this study achieved a penetration depth of 1.5 mm which is more than that of Vreeling et al. [59]. The high penetration depth achieved in this study was affected by the low travel speed which increases the time of melting allowing particles time to sink as compared to the work done by Vreeling et al. [59]. The main factor for the penetration is the hot melt pool generated with the high laser power. From studies conducted by Vreeling et al. [59], particles only penetrated the melt after preheating the substrate above 300 ^{o}C for the set parameters used (see Figure 6-33).

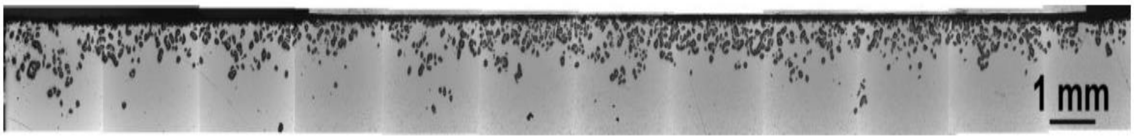

Figure 6-33: Longitudinal cross-section of laser melt bead (Power = 310 W/mm^2, travel speed = 0.5 m/min; penetration depth = 1.1 mm) [59]

From the melt geometries of this study (Table 6-8 and Figure 6-29), larger melt areas were observed in coated substrates indicating increased melt pool temperatures as compared to the uncoated melt beads. It would be expected that for the same parameters, more particles would penetrate the melt in the case of the coated substrate which was not the case. It appears that the graphite coating acts as a barrier thereby inhibiting penetration of SiC particles in the melt pool. From the process monitoring (Figure 6-30), it can be seen that the deflection of particles is likely to be due to the rapid solidification of the melt. The rapid solidification causes SiC particles to bounce off the plate.

By comparing the melt bead sizes of the LMI process to WAAM (He and Ar) for uncoated substrates, it was found that WAAM processes produces larger melt beads despite their low power (3.8 kW) as compared to the LMI process (5 kW). The reduced melt areas in LMI process can be attributed to the low spot size and the reflection of the laser beam. The melt areas can also be correlated with the location of particles in the melt beads. For melt beads produced by laser melt injection and WAAM using Ar gas, SiC particles penetrated at the top surface. On the other hand, melt beads produced by WAAM using He gas resulted in particles at the top, middle as well as localising at the bottom of the melt bead.

7 Conclusions, summary of results and future work

7.1 Conclusions

From the studies carried out, it is difficult to achieve SiC injection in aluminium by wire + arc additive manufacture. ACTIG process is better than MIG process but the control on temperature is critical during the injection process. Hence, the temperature of the melt pool is increased by using helium shielding gas (He) and by isolating the plate using thinner section plates embedded on an insulating bar to eliminate the heat losses and increase the melt area. This results in particles sinking to the bottom of the melt.

Therefore WAAM process is critical for production of Al-SiC composites and has a narrow operating range with poor distribution of particles. Moreover, with arc based processes, there are complications with arc plasma which could potentially affect the injection process.

7.2 Summary of results

7.2.1 Process studies of MIG deposition on aluminium WAAM

- Wire feed speed to travel speed ratio (WFS/TS) is the key factor controlling bead dimensions.
- Cold metal transfer pulse advance (CMT-PA) wire + arc additive manufacture (WAAM) is stable for WFS/TS ratios ranging between 5 and 25 but the working envelope was restricted to a wire feed speed range of 4-8 m/min. This enabled an effective wall width range of 4.9 – 8.0 mm.
- From the microstructure analysis, dendrite grains were found within layers and equiaxed grains between the interlayer boundaries.
- There was a direct correlation between the number and size of pores with WFS/TS ratio.
- CMT-PA is not suitable for production of thicker section walls which exceed the limit of single bead width.

- CMT-P process eliminates the lack of fusion defects associated CMT-PA process during thicker section deposition.
- Parallel deposited walls have higher hardness values than oscillated walls.
- The UTS and YS are maximum with a reduction in elongation after T6 post deposition treatment in comparison to the as-deposited walls.
- From the result of the microstructure, parallel walls were characterised by both columnar and equiaxed grains whereas oscillated walls were characterised by equiaxed grains.
- Oscillated walls display increased pore numbers as compared to parallel walls.

7.2.2 Process studies of TIG deposition on aluminium WAAM

- Minimum cleaning for ACTIG process ranged between 10 %EP and 20 %EP.
- The effective wall width is minimum at 20 %EP with a corresponding maximum in layer height. Increasing % EP between 10 %EP and 40 %EP does not have a significant effect on surface waviness.
- The main controlling factor for wall dimension is the heat input. Increasing % EP increases the voltage which in turn increases the heat input.
- Increasing the % EP increases the electrode wear rate.
- Increasing the % EP does not have any significant effect on mechanical properties (UTS, 0.2 PS and % elongation).
- For a constant % EP, frequency does not have any significant effect on WAAM wall dimensions and hardness.
- Increasing the % EP increases grain sizes and decreases the grain number.
- Increasing % EP increases pore sizes and number.
- For the WAAM process envelope developed, a wider working envelop was possible with wall width ranging between 7.8 mm and 16 mm.
- Increasing the WFS/TS ratio increases the wall width and layer height
- Increasing the current increases the wall width and decreases the layer height at constant WFS/TS ratio.

7.2.3 Production of Al-SiC composites by WAAM

- The main factors for embedding SiC particle in aluminium matrix are increased melt temperature and the longer melt duration.
- From the melt bead geometry, He shielding gas increases the temperature of the melt pool as compared to Ar gas for the same heat input. This enables the injection of SiC reinforcement particles in Al melt.
- Increasing the heat input of He produced melt beads increases the volume fraction of SiC particles in the melt.
- Coarse SiC particles have higher momentum than fine particles which enhaces its ability to penetrate the melt bead surface.
- Increasing the particle feed rate increases the volume fraction of SiC in the melt.
- SiC reinforcement increases the hardness of aluminium matrix.
- Laser melt injection technique enables partilces to be injected at the surface of the melt for an uncoated substrate but not for graphite coated substrates
- Graphite coated substrates increases the melt bead size for the laser melt injection technique.

7.3 Future work

- Conducting studies in an enclosed shielding environment to minimise surface oxides and assess the possibility of injecting SiC reinforcement in aluminium matrix.
- Investigate the effect of powder with surfactants using ceramic cored wires to lower the surface tension of aluminium melt to enhance the penetration particles in an argon melt pool.
- Extended studies on laser can also be conducted to reduce the coupling effect by addition of filler wire or using hybrid laser welding.
- Further studies can be conducted on the influence of He and Ar (He/Ar) gas mix on the powder embedding efficiency.

References

1. Bechmann F., Fallböhmer P., Stauber R., Rauber C., Lohmüller A., Hartmann M., et al. Reinforced Light Metals for Automotive Applications. SAE International. 2007. p. 1234. Available at: DOI:10.4271/2007-01-1228

2. Centro FR. The research requirement of the transport sectors to facilitate an increased usage of composite materials. 2004. pp. 1–20. Available at: http://www.transport-research.info/sites/default/files/project/documents/20050222_155158_31010_Composit_Automotive_Report.pdf (Accessed: 21 September 2017)

3. Chawla N., Chawla KK. Metal-matrix composites in ground transportation. The Journal of the Minerals, Metals & Materials Society. 2006; 58(11): 67–70. Available at: DOI:10.1007/s11837-006-0231-5

4. Stojanović B., Ivanović L. Application of aluminium hybrid composites in automotive industry. Tehnicki vjesnik - Technical Gazette. 2015; 22(1): 247–251. Available at: DOI:10.17559/TV-20130905094303

5. Gupta M., Eric A., Jarfors W. Aluminum and Magnesium Metal Matrix Nanocomposites. Singapore: Springer Nature Singapore Ltd; 2017. Available at: http://ebook-dl.com/md5/88b2215e45508a81588cccbf3121fca7.pdf (Accessed: 5 July 2017)

6. Suryanarayanan K., Praveen R., Raghuraman S. Silicon Carbide Reinforced Aluminium Metal Matrix Composites for Aerospace Applications : A Literature Review. International Journal of Innovative Research in Science, Engineering and Technology. 2013; 2(11): 6336–6344.

7. Michaud VJ. Liquid State Processes. Fundamentals of Metal-Matrix Composites. Elsevier; 1993. pp. 3–22. Available at: DOI:10.1016/B978-0-08-052371-2.50005-5 (Accessed: 28 October 2014)

8. Meena KL., A. Manna D., S.S. Banwait D., Jaswanti D. An Analysis of Mechanical Properties of the Developed Al/SiC-MMC’s. American Journal of Mechanical Engineering. 31 January 2013; 1(1): 14–19. Available at: DOI:10.12691/ajme-1-1-3 (Accessed: 24 September 2014)

9. Hashim J., Looney L., Hashmi MSJ. Metal matrix composites: production by the stir casting method. Journal of Materials Processing Technology. August 1999; 92–93: 1–7. Available at: DOI:10.1016/S0924-0136(99)00118-1 (Accessed: 14 October 2014)

10. Dunning PD. Introducing Loading Uncertainty in Level Set-Based Structural Topology Optimisation. University of Bath; 2011.

11. Hiller JD., Lipson H. Multi Material Topological Optimization of Structures and Mechanisms. Genetic and Evolutionary Computation Conference.

2009. pp. 1521–1528.

12. Tomlin M., Meyer J. Topology Optimization of an Additive Layer Manufactured (ALM) Aerospace Part. The 7th Altair CAE Technology Conference 2011. 2011; : 1–9.

13. Rao, J Kiran S. Topology Optimization of Aircraft Wing. CEUR Workshop Proceedings. 2015; 1542(9): 33–36. Available at: DOI:10.1017/CBO9781107415324.004

14. Bhavar V., Kattire P., Patil V., Khot S., Gujar K., Singh R. A Review on Powder Bed Fusion Technology of Metal Additive Manufacturing. 4th International Conference and Exhibition on Additive Manufacture. 2014.

15. Williams SW., Martina F., Addison a. C., Ding J., Pardal G., Colegrove P. Wire+Arc Additive Manufacturing. Materials Science and Technology. 2015; 32(7): 641–647. Available at: DOI:10.1179/1743284715Y.0000000073

16. Ding D., Pan Z., Cuiuri D., Li H. Wire-feed additive manufacturing of metal components: technologies, developments and future interests. International Journal of Advanced Manufacturing Technology. 2015; 81(1–4): 465–481. Available at: DOI:10.1007/s00170-015-7077-3

17. EADS and EOS research study on sustainability of DMLS. Available at: https://www.eos.info/press/customer_case_studies/eads (Accessed: 9 June 2017)

18. Get into High Gear with Altair's Optimized Race Car Brake Pedal | Materialise - Innovators you can count on. Available at: http://www.materialise.com/en/cases/get-into-high-gear-altairs-optimized-race-car-brake-pedal (Accessed: 9 June 2017)

19. Suragimath PK., Purohit GK. A Study on Mechanical Properties of Aluminium Alloy (LM6) Reinforced with SiC and Fly Ash. Journal of Mechanical and Civil Engineering. 2013; 8(5): 13–18.

20. Cobden R., Banbury A. Aluminium: Physical Properties, Characteristics and Alloys. TALAT. Association European Aluminium; 1994. Available at: http://www.alueurope.eu/talat/lectures/1501.pdf

21. Aluminum: History. Available at: http://nautilus.fis.uc.pt/st2.5/scenes-e/elem/e01310.html (Accessed: 23 July 2017)

22. Encyclopedia Britannica. Available at: https://www.britannica.com/biography/Paul-Louis-Toussaint-Heroult (Accessed: 2 October 2017)

23. Mathers G. The Welding of Aluminium and its Alloys. The Welding of Aluminium and its Alloys. Cambridge, England: Woodhead Publishing Limited; 2002. 1-9 p. Available at: DOI:10.1533/9781855737631.1

24. Singh H., Jit SN., Tyagi AK. An Overview of Metal Matrix Composite:

Processing and SiC Based Mechanical Properties. Journal of Engineering Research and Studies. 2011; 2(4): 72–78.

25. Davis JR. Aluminum and Aluminum Alloys. Light Metals and alloys. ASM International; 2001. pp. 351–416. Available at: DOI:10.1361/autb2001p351

26. Weman Klas. Welding processes handbook. Second Edi. Cambridge, UK: Woodhead Publishing Limited; 2012.

27. Ashby MF., Jones DRH. Engineering materials 2. Third. An Introduction to Microstructures, Processing, and Design. Cambridge, UK: Elsevier; 1998.

28. Wellman B. Solid Solution Hardening & Strength. Technical Tidbits. 2010; (16). Available at: https://materion.com/-/media/files/pdfs/alloy/newsletters/technical-tidbits/issue-no-16-solid-solution-hardening--strength.pdf (Accessed: 21 September 2017)

29. Cambell FC. Chapter 26. Elements of Metallurgy and Engineering Alloys. 2008; 3: 487–508. Available at: DOI:10.1007/978-1-60327-017-5

30. Lakhtin Y. Engineering Physical Metallurgy. New Delhi-India: S.K. Jain for CBS Publishers & Distributors; 1998.

31. Boopathi MM., Arulshri KP., Iyandurai N. Evaluation of Mechanical Properties of Aluminium Alloy 2024 Reinforced with Silicon Carbide and Fly Ash Hybrid Metal Matrix Composites. American Journal of Applied Sciences. 1 March 2013; 10(3): 219–229. Available at: DOI:10.3844/ajassp.2013.219.229

32. Callister WD. Materials Science and Engineering: An Introduciton. Seventh Ed. New York: John Wiley & Sons, Inc.; 2007.

33. Surappa MK. Aluminium matrix composites : Challenges and opportunities. Sadhana. 2003; 28: 319–334.

34. Lloyd DJ. Particle reinforced aluminium and magnesium matrix composites. International Materials Reviews. 1 January 1994; 39(1): 1–23. Available at: DOI:10.1179/095066094790150982

35. Huda D., El Baradie MA., Hashmi MSJ. Metal-matrix composites: Manufacturing aspects. Part I. Journal of Materials Processing Technology. February 1993; 37(1–4): 513–528. Available at: DOI:10.1016/0924-0136(93)90114-L

36. Carreño-Morelli E., Cutard T., Schaller R., Bonjour C. Processing and characterization of aluminium-based MMCs produced by gas pressure infiltration. Materials Science and Engineering: A. 1998; 251(1–2): 48–57.

37. Ramnath BV., Elanchezhian C., Atreya TSA., Vignesh V. Aluminium Metal Matrix Composites - A Reveiw. Rev. Adv. Mater.Sc. 2014; 38: 55–60.

38. Kok M. Properties and Mechanical Properties of Al2O3 Particulate-Reinforced 2024 Aluminium Alloy Composites. Journal of Materials

Processing Technology. 2005; 161: 381–387.

39. J.C. Viala, M. Peronnet FB and JB. Chemical Compatibility between Aluminium base matrices and light refractory carbide reinforcements. Villeurbanne Cedex, France; Available at: http://www.iccm-central.org/Proceedings/ICCM12proceedings/site/papers/pap739.pdf (Accessed: 28 June 2015)

40. Hao Z., Ding C., Zhen-hua C. Densification of Spray Deposited Aluminum Composite Sheets via Ceramic Rolling Technique. Materials and Manufacturing Processes. 2008; 23(5): 479–483. Available at: DOI:10.1080/10426910802103866

41. AZO materials. Properties: Aluminium - Advantages and Properties of Aluminium. Available at: https://www.azom.com/properties.aspx?ArticleID=1446 (Accessed: 21 February 2018)

42. Raquibul Hasan M. Failure Investigation Report on Different Components of an Automotive Engine. International Journal of Mechanical Engineering and Applications. 2017; 5(1): 47–51. Available at: DOI:10.11648/j.ijmea.20170501.16

43. Stojanovic B., Babic M., Mitrovic S., Vencl A., Miloradovic N., Pantic M. Tribological characteristics of aluminium hybrid composites reinforced with silicon carbide and graphite. A review. Journal of the Balkan Tribological Association. 2013; 19(1): 83–96.

44. Miracle DB. Metal matrix composites – From science to technological significance. Composites science and Technology. 2005; 65: 2526–2540. Available at: DOI:10.1016/j.compscitech.2005.05.027

45. Melgi MC., Purohit GK. A Study of Microstructure and Mechanical Properties of Aluminium Silicon Carbide Metal Matrix Composites (MMC's). International Journal of Engineering Research & Technology (IJERT). 2013; 2(9): 690–700.

46. Kaptay G. Interfacial phenomena during melt processing of ceramic particle-reinforced metal matrix composites part I. Introduction (incorporation) of solid particles into melts. Materials Science Forum. 1996; 215: 467–474.

47. Pawar PB., Utpat AA. Development of Aluminium Based Silicon Carbide Particulate Metal Matrix Composite for Spur Gear. Procedia Materials Science. 2014; 6: 1150–1156. Available at: DOI:10.1016/j.mspro.2014.07.187 (Accessed: 5 October 2014)

48. Hashim J. The Production of Cast Metal Matrix Composites by a Modified Stir Casting Method. Jurnal Tecknologi. 2007; 35(A): 9–20.

49. Saravanapandi SA., Balavignesh P., Pravinkumar S. Processing Techniques and applications of Metal Matrix Composites. Tuticorin, India;

Available at: https://www.academia.edu/8932186/PROCESSING_TECHNIQUES_AND_APPLICATIONS_OF_METAL_MATRIX_COMPOSITES (Accessed: 16 December 2014)

50. Shorowordi KM., Laoui T., Haseeb ASMA., Celis JP., Froyen L. Microstructure and interface characteristics of B4C, SiC and Al2O3 reinforced Al matrix composites: a comparative study. Journal of Materials Processing Technology. December 2003; 142(3): 738–743. Available at: DOI:10.1016/S0924-0136(03)00815-X (Accessed: 21 June 2015)

51. Li W., Liang H., Chen J., Zhu SQ., Chen YL. Effect of SiC Particles on Fatigue Crack Growth Behavior of SiC Particulate-reinforced Al-Si Alloy Composites Produced by Spray Forming. Procedia Materials Science. 2014; 3: 1694–1699. Available at: DOI:10.1016/j.mspro.2014.06.273 (Accessed: 14 October 2014)

52. Occhionero MA., Hay RA., Adams RW., Fennessy KP. Aluminum Silicon Carbide (AlSiC) For Cost-Effective Thermal Management And Functional Microelectronic Packaging Design Solutions. Proceedings of SPIE- The international Society for Optical Engineering. 1998. pp. 1–4.

53. Tham LM., Gupta M., Cheng L. Effect of limited matrix–reinforcement interfacial reaction on enhancing the mechanical properties of aluminium–silicon carbide composites. Acta Materialia. September 2001; 49(16): 3243–3253. Available at: DOI:10.1016/S1359-6454(01)00221-X

54. Bhandare RG., Sonawane PM. Preparation of Aluminium Matrix Composite by Using Stir Casting Method. International Journal of Engineering and Advanced Technology(IJEAT). 2013; 3(2): 61–65.

55. Sarkar S., Singh A. Studies on Aluminum-Iron Ore in-Situ Particulate Composite. Open Journal of Composite Materials. 2012; 2(January): 22–30.

56. Pradeep S., Gulsian C., Neeraj S. Production of AMC by Stir Casting - An Overview. International Journal of Contemporary Practices. 2013; 2(1): 23–46.

57. Blucher JT. Discussion of a liquid metal pressure infiltration process to produce metal matrix composites. Journal of Materials Processing Technology. 1992; 30: 381–390.

58. Singh R., Singla R. Tribological Characterization of Aluminium-Silicon Carbide Composite Prepared By Mechanical Alloying. International Journal of Applied Engineering Research. 2012; 7(11): 1420–1423.

59. Vreeling JA., Hosson DE., Ocelik V., Pei TY., V. A. Laser Melt Injection in Aluminum Alloys : on the Role of the Oxide Skin. Acta Materialia. 2000; 48: 4225–4233.

60. Jendrzejewski R., Van Acker K., Vanhoyweghen D., Śliwiński G. Metal

matrix composite production by means of laser dispersing of SiC and WC powder in Al alloy. Applied Surface Science. 2009; 255(10): 5584–5587. Available at: DOI:10.1016/j.apsusc.2008.09.048

61. Vreeling JA. Laser Melt Injection of Ceramic Particles in Metals. Groningen University; 2001.

62. Koebler NB., Scholar M. Characterization and Optimization of a Powder Feed Nozzle for High Deposition Laser Cladding. Penssylvania; Available at: http://forms.gradsch.psu.edu/diversity/mcnair/mcnair_jrnl2010/files/Koebler.pdf (Accessed: 4 July 2017)

63. Media P. Efficient Powder Process Handling. Available at: http://www.chemicalprocessing.com/assets/wp_downloads/pdf/efficient-powder-process-handling-ebook.pdf (Accessed: 22 September 2017)

64. John W. Carson and Brian H. Pittenger J& J. Bulk properties of Powders. ASM Handbook, Vol 7 : Powder Metal Technologies and Application. 1998; 7: 97–101. Available at: DOI:10.1361/asmhba00015

65. Ehsan T., Khajepour A., Corbin S. Laser Cladding Laser Cladding. New York Washington, D.C.: CRC press; 2005.

66. Liberto NPE. Overcoming powder-feed problems. 1992. pp. 1–3. Available at: http://www.powdercc.com/pdf/Overcoming powder-feed problems.pdf

67. Katz RN., Makhlouf MM., Introduction I. Optimum Parameters for Wetting Silicon Carbide by Aluminum Alloys. METALLURGICAL AND MATERIALS TRANSACTIONS A. 2000; 31(February): 565–573.

68. Skolianos S. Mechanical behavior of cast SiCp-reinforced. Materials Science and Engineering: A. 1996; 210: 76–82.

69. Coucil N research. Opportunities in Protection Materials Science and Technology for Future Army Applications. Washington, D.C.: National Academies Press; 2011. Available at: DOI:10.17226/13157 (Accessed: 22 July 2017)

70. Mosisa E., YU Bazhin V., Savchenkov S. Review on Nano Particle Reinforced Aluminium Metal Matrix Composites. Research Journal of Applied Sciences. 2016; 11(5): 188–196.

71. Warren R., Andersson C-H. Silicon carbide fibres and their potential for use in composite materials. Part II. Composites. 1984; 15(2): 101–111.

72. Vreeling JA., Ocelı V., Hamstra GA., Pei YT., Hosson JTM De. In-situ microscopy investigation of failure mechanisms in AL/SiC p metal matrix composites produced by laser embedding. 2000; 42: 589–595.

73. Neelima DC., Mahesh V., Selvaraj N. Mechanical characterization of Aluminium silicon carbide composite. International Journal of Applied Engineering Reseach, Dindigul. 2011; 1(4): 793–799.

74. Nagaral M., Bharath V., Auradi V. Material Science & Engineering Effect of Al 2 O 3 Particles on Mechanical and Wear Properties of 6061al Alloy Metal Matrix Composites. Material Science & Engineering. 2013; 2(1): 2–5. Available at: DOI:10.4172/2169-0022.1000120

75. Erlangung Z., Zhang W. Rapid Prototyping of Ceramic / Metal Composites (Rapid Prototyping von Keramik / Metall-Verbundwerkstoffen). 2010;

76. Jayalakshmi S., Gupta M. Metallic Amorphous Alloy Reinforcements in Light Metal Matrices. 2015. Available at: DOI:10.1007/978-3-319-15016-1

77. Kobryn PA., Ontko NR. Additive Manufacturing of Aerospace Alloys for Aircraft Structures. Cost Effective Manufacture via Net-Shape Processing. 2006. pp. 3-1-3–14.

78. Consultants Berger R. Additive manufacturing A game changer for the manufacturing industry? 2013; (November): 1–33. Available at: https://www.rolandberger.com/publications/publication_pdf/roland_berger_additive_manufacturing_1.pdf

79. Brackett D., Ashcroft I., Hague R. Topology optimisation for additive manufacturing. University of Loughborough; 2011; : 348–362.

80. Gu J., Cong B., Ding J., Williams SW., Zhai Y. Wire+arc additive manufacturing of aluminium. Proc. 25th Int. Solid Freeform Fabrication Symp. University of Texas; 2014. pp. 451–458. Available at: https://sffsymposium.engr.utexas.edu/sites/default/files/2014-038-Gu.pdf (Accessed: 19 October 2017)

81. Zhang Y., Wei Z., Shi L., Xi M. Characterization of laser powder deposited Ti-TiC composites and functional gradient materials. Journal of Materials Processing Technology. 2008; 206(1–3): 438–444. Available at: DOI:10.1016/j.jmatprotec.2007.12.055

82. Booth G. Manufacturing with Lasers Developments and Opportunities (July 2004). IIW Annual Assembly. Osaka, Japan: The Welding Institute; 2004. Available at: http://www.twi-global.com/technical-knowledge/published-papers/manufacturing-with-lasers-developments-and-opportunities-july-2004/ (Accessed: 24 September 2017)

83. Endless Possibilities with Sciaky's Expanded Lineup of Electron Beam Additive Manufacturing (EBAM) Systems | Additive Manufacturing (AM). Available at: http://additivemanufacturing.com/2015/08/24/endless-possibilities-with-sciakys-expanded-lineup-of-electron-beam-additive-manufacturing-ebam-systems/ (Accessed: 25 September 2017)

84. Heralić A. Monitoring and Control of Robotized Laser Metal-Wire Deposition. Chalmers University of Technology, Sweden; 2012. Available at: DOI:LMD_Thesis

85. Mehnen J., Ding J., Lockett H., Kazanas P. Design for Wire and Arc Additive Layer Manufacture. 2010; : 19–21.

86. Martina F., Mehnen J., Williams SW., Colegrove P., Wang F. Investigation of the benefits of plasma deposition for the additive layer manufacture of Ti–6Al–4V. Journal of Materials Processing Technology. June 2012; 212(6): 1377–1386. Available at: DOI:10.1016/j.jmatprotec.2012.02.002

87. Wang F., Williams S., Rush M. Morphology investigation on direct current pulsed gas tungsten arc welded additive layer manufactured Ti6Al4V alloy. The International Journal of Advanced Manufacturing Technology. 8 April 2011; 57(5–8): 597–603. Available at: DOI:10.1007/s00170-011-3299-1 (Accessed: 7 December 2014)

88. Venkatesh R., Hariharan AM., Muthukrishnan N. Machinability Studies of Al / SiC / (20p) MMC by Using PCD Insert (1300 grade). Proceedings of the World Congress on Engineering. 2009. pp. 1–4.

89. Bandari Y., Williams S., Ding J., Martina F. Additive Manufacture of Large Structures: Robotic or Cnc Systems. 26th International Solid Freeform Fabrication Symposium, Austin, Texas; 08/2015. 2015. pp. 17–25. Available at: DOI:10.1017/CBO9781107415324.004

90. Almeida P. Process Control and Development in Wire and Arc Additive Manufacturing. Cranfield University, Bedfordshire, UK; 2012.

91. Gu J., Ding J., Gu H., Bai J., Zhai Y., Ma P. The strengthening effect of inter-layer cold working and post-deposition heat treatment on the additively manufactured Al– 6.3Cu alloy. Materials Science & Engineering A. 2016; 651: 18–26.

92. Gu J., Ding J., Williams SW., Gu H., Ma P., Zhai Y. The effect of inter-layer cold working and post-deposition heat treatment on porosity in additively manufactured aluminum alloys. Journal of Materials Processing Technology. 2016; 230: 26–34. Available at: DOI:10.1016/j.jmatprotec.2015.11.006

93. Cong B., Ding J., Williams S. Effect of arc mode in cold metal transfer process on porosity of additively manufactured Al-6.3%Cu alloy. The International Journal of Advanced Manufacturing Technology. 2014; 76: 1593–1606. Available at: DOI:10.1007/s00170-014-6346-x

94. Cong B., Qi Z., Qi B., Sun H., Zhao G., Ding J. A Comparative Study of Additively Manufactured Thin Wall and Block Structure with Al-6.3%Cu Alloy Using Cold Metal Transfer Process. Applied Sciences. 2017; 7(3): 275. Available at: DOI:10.3390/app7030275

95. Bai LY., Lin SB., Dong SB., Fan CL. Mechanical properties of 2219-Al components produced by additive manufacturing with TIG. Int J Adv Manuf Technol. 2016; 86: 479–485. Available at: https://www.researchgate.net/profile/Sanbao_Lin/publication/299518465_Molten_pool_behaviors_and_weld_forming_characteristics_of_all-position_tandem_narrow_gap_GMAW/links/58992631aca2721f0daf42ca/Molten-pool-behaviors-and-weld-forming-characteristics-of-al (Accessed:

6 July 2017)

96. Wang H., Jiang W., Ouyang J., Kovacevic R. Rapid prototyping of 4043 Al-alloy parts by VP-GTAW. Journal of Materials Processing Technology. May 2004; 148(1): 93–102. Available at: DOI:10.1016/j.jmatprotec.2004.01.058 (Accessed: 28 June 2015)

97. Cirino LM., Dutra JC. The influence of positive polarity time on GTAW AC of aluminium. Welding International. 2010; 24(January): 825–833. Available at: DOI:10.1080/09507110903568919

98. Yarmuch MAR., Patchett BM. Variable AC Polarity GTAW Fusion Behavior in 5083 Aluminum. Welding Research. 2007; 86: 196–200. Available at: https://app.aws.org/wj/supplement/wj0707-196.pdf

99. Yarmuch M., Pepin J., A.C. B., Patchet B.M. Characterisation of fusion behaviour during variable polarity ac welding of aluminium. Trends in Welding Research proceedings of 9th International Conferences. 2013. pp. 129–137.

100. Pickin CG., Williams SW., Lunt M. Characterisation of the cold metal transfer (CMT) process and its application for low dilution cladding. Journal of Materials Processing Technology. 2011; 211: 496–502. Available at: DOI:10.1016/j.jmatprotec.2010.11.005

101. Fronius. CMT: Cold Metal Transfer. 2011. Available at: http://www.digitalweldingsolutions.com/CMT.pdf (Accessed: 14 August 2015)

102. Causes of common problems encountered during welding of aluminium. Available at: http://www.idc-online.com/technical_references/pdfs/mechanical_engineering/Causes_of_common_problems.pdf (Accessed: 22 July 2017)

103. Zhou W. Problems in Welding of High Strength Aluminium Alloys. 1999. Available at: http://www.ntu.edu.sg/home/mwzhou/Papers/Zhou 1999 - Welding of Al Alloys.pdf (Accessed: 28 June 2015)

104. Kou S. Metallurgy Second Edition Welding Metallurgy. Structure. 2003. 466 p. Available at: DOI:10.1016/j.theochem.2007.07.017

105. Campbell SW., Galloway a M., McPherson N a. Arc pressure and fluid flow during alternating shielding gases. Part 2: arc force determination. Science and Technology of Welding and Joining. 2013; 18(7): 597–602. Available at: DOI:10.1179/1362171813Y.0000000141

106. Wang S., Nates R., Pasang T., Ramezani M. Modelling of Gas Tungsten Arc Welding Pool under Marangoni Convection. Universal journal of Mechanical engineering. 2015; 3(5): 185–201. Available at: DOI:10.13189/ujme.2015.030504

107. Prakash J., Tewari SP., Srivastava BK. Shielding Gas for Welding of

Aluminium Alloys by TIG / MIG Welding-A Review. International Journal of Modern Engineering Research (IJMER). 2016; 1(2): 690–699.

108. Rao ZH., Liao SM., Tsai HL. Effects of shielding gas compositions on arc plasma and metal transfer in gas metal arc welding. Journal of Applied Physics. 2010; 107(4): 1–11. Available at: DOI:10.1063/1.3291121

109. Murphy AB., Tanaka M., Tashiro S., Sato T., Lowke JJ. A computational investigation of the effectiveness of different shielding gas mixtures for arc welding. Journal of Physics D: Applied Physics. 2009; 42(11): 115205. Available at: DOI:10.1088/0022-3727/42/11/115205

110. Campbell S., Galloway A., Mcpherson N. Derivation of Forces Acting on the Liquid Weld Metal Based on Arc Pressure Measurements Produced Using Alternating Shielding Gases in the Gtaw Process. The 8th Pacific International Congress on Advanced materials and Processing. 2013. pp. 2375–2386.

111. Dong W., Lu S., Li D., Li Y. GTAW liquid pool convections and the weld shape variations under helium gas shielding. International Journal of Heat and Mass Transfer. Elsevier Ltd; 2011; 54(7–8): 1420–1431. Available at: DOI:10.1016/j.ijheatmasstransfer.2010.07.069

112. Peasura P., Watanapa A. Influence of shielding gas on aluminum alloy 5083 in gas Tungsten arc welding. Procedia Engineering. 2012; 29: 2465–2469. Available at: DOI:10.1016/j.proeng.2012.01.333

113. Kolarik L., Kovanda K., Kolarikova M. Influence of shielding gas on GMA welding of AL alloys. Metal Science. 2013; : 3–6.

114. Ding D., Pan Z., Cuiuri D., Li H. A multi-bead overlapping model for robotic wire and arc additive manufacturing (WAAM). Robotics and Computer-Integrated Manufacturing. Elsevier; 2015; 31: 101–110. Available at: DOI:10.1016/j.rcim.2014.08.008

115. Bandari YK., Charrett TOH., Michel F., Ding J., Williams SW., Tatam RP. Compensation Strategies for Robotic Motion Errors for Additive Manufacturing (AM). Proceedings of 27th Annual International Solid Freeform Fabrication Symposium. Texas, USA; 2016.

116. Pinter Z. Study of aluminium wire + arc additive manufacture. Cranfield University, UK; 2017.

117. Armao F. Aluminum Workshop: How to recognize, minimize weld smut - The Fabricator. Available at: http://www.thefabricator.com/article/aluminumwelding/how-to-recognize-minimize-weld-smut (Accessed: 13 October 2017)

118. Nguyen H. The Effects of Solidification Rates on Porosity Formation and Cast Microstructure of Aluminum Alloy A356. Michigan: Grand Valley state University; 2005.

119. Kurz W., Bezençon C., Gäumann M. Columnar to equiaxed transition in solidification processing. Science and Technology of Advanced Materials. 2001; 2(1): 185–191. Available at: DOI:10.1016/S1468-6996(01)00047-X

120. Sarrafi R., Kovacevic R. Cathodic Cleaning of Oxides from Aluminum Surface by Variable-Polarity Arc. Welding Journal. 2010; 89(1): 1S–10S.

121. DuPont JN., Marder a. R. Thermal Efficiency of Arc Welding Processes. Welding Research Supplement. 1995; (December): 406–416.

122. Cho J., Lee J-J., Bae S-H. Heat input analysis of variable polarity arc welding of aluminum. The International Journal of Advanced Manufacturing Technology. 2015; 81(5–8): 1273–1280. Available at: DOI:10.1007/s00170-015-7292-y

123. Fuerschbach PW. Cathodic cleaning and heat input in variable polarity plasma arc welding of aluminum. Welding Journal (Miami, Fla). 1998; 77(2): 76–s. Available at: http://www.scopus.com/inward/record.url?eid=2-s2.0-0031999969&partnerID=40&md5=ab9619a0db45a393544e3551b352a063

124. Syed WUH., Pinkerton AJ., Li L. Simultaneous wire- and powder-feed direct metal deposition: An investigation of the process characteristics and comparison with single-feed methods. Journal of Laser Applications. Laser Institute of America; 9 February 2006; 18(1): 65–72. Available at: DOI:10.2351/1.2164485 (Accessed: 18 August 2017)

125. Min D., Shen J., Lai S., Chen J. Effect of heat input on the microstructure and mechanical properties of tungsten inert gas arc butt-welded AZ61 magnesium alloy plates. Materials Characterization. Elsevier Inc.; 2009; 60(12): 1583–1590. Available at: DOI:10.1016/j.matchar.2009.09.010